Synthesis, Properties and Applications of Cadmium Based Nanoparticles Emitting from 400 – 750 nm

A thesis submitted to The University of Manchester for the degree of

Doctor of Philosophy

in the Faculty of Engineering and Physical Sciences

2010

Katayune Presland

School of Chemistry

Contents

Final word count : 39,583

List of Figures

List of Tables

Abstract

This thesis concerns the synthesis of cadmium based nanoparticles that emitted from 400 to the near infrared (NIR) region. Once synthesised they can be possibly used as biomarkers once encapsulated in microspheres. A brief introduction to the area of nanomaterials is also provided.

The focus of this thesis is split into three main categories. Firstly core/shell nanoparticles were synthesised due to their ability to emit over a large range of wavelengths. Alloyed nanoparticles were then synthesised due to their ability of being very good photoemitters. Finally core/shell/shell nanoparticles were synthesised as they had the ability of emitting in the NIR region.

This thesis is split into five main chapters. The first chapter is a brief introduction to the field of nanomaterials, analysis techniques and current and possible future applications. Chapters 2, 3, and 4 contain the main research carried out with brief synthetic methods and detailed analysis and characterization. Chapter 5 contains detailed synthetic methods with experimental conditions and specific equipment used for this research.

Declaration

No portion of the work referred to in the thesis has been submitted in support of an application for another degree or qualification of this or any other university or other institute of learning. All work included was completed at the University of Manchester.

Copyright and the ownership of intellectual property rights

(i) The author of this thesis (including any appendicies and/or schedules to this thesis) owns any copyright in it (the "copyright") and s/he has given the University of Manchester the right to use such Copyright for any administrative, promotional, educational and/or teaching purposes.

(ii) Copies of this thesis, either in full or in extracts, may be made only in accordance with the regulations of the John Rylands University Library of Manchester. Details of these regulations may be obtained from the Librarian. This page must form part of any such copies made.

(iii) The ownership of any patents, designs, trade marks and any and all other intellectual property rights except for the Copyright (the "Intellectual Property Rights") and any reproductions of copyright works, for example graphs and tables ("Reproductions"), which may be described in this thesis, may not be owned by the author and may be owned by third parties. Such Intellectual Property Rights and Reproductions cannot and must not be made available for use without the prior written permission of the owner(s) of the relevant Intellectual Property Rights and/or Reproductions.

(iv) Further information on the conditions under which disclosure, publication and exploitation of this thesis, the Copyright and any Intellectual Property Rights and/or Reproductions described in it may take place is available from the Head of School of Chemistry and the Dean of the Faculty of Engineering and the Physical sciences.

Acknowledgments

First of all I would like to thank my supervisor, Paul O'Brien for his guidance. I am also thankful for the advice provided by Mo and Azad. I'd like to thank members of the group that provided me with suggestions, help and friendship during my time in and sometimes outside of the lab, noting Alex, S'bu, Ahmed and Deborah. I also need to thank Imrana and Mike at Nanoco for assistance with running QYs. Thanks also to Judith and Alan for help with the temperamental XRD and TEM machines in Materials! Thanks need to go to J. Behrendt from the A. Sutherland group in Aston for immobilizing my QDs, Simon Fairclough from the J. Smith group in Oxford for the single crystal investigations, Stuart Stubbs from the D. Binks group in Manchester for comparing the PL transient decays of my Type I and Type II/Type I QDs and finally Steve Magennis for multiexitation experiments.

I'd like to thank members of the Coe group as they have provided me with many hours of entertainment in the form of pointless and funny conversations in the labs and cakes and other goodies in their office. This especially includes Foxon and Martyn for being the cause of me not leaving for at least an hour after I'd originally planned on going home.

I did not mention Laura or Cat above as they both deserve a special mention because they are two of my best friends and have provided me with hours of entertainment in and out of the lab. Cat and I both danced around to music in the lab and Laura, as well as being my housemate for 4 years, is one of my closest friends who has helped me a lot during our PhDs!

My thanks to other members of the chemistry department include Matthew Pumford, Christine Martyniuk and of course Mary Lea. Mary was like my chemistry mum and when times got hard she was a shoulder to cry on as well as being an amazing person to work for who is sorely missed. Mike and Graham kept me entertained whilst demonstrating to the undergrads and all of the various outreach activities. Tour guiding, outreach and demonstrating provided me with hours of fun as well as moments stress but all totally worth it. Without Ryan, Liam, Nigel, Helen, Jon, Adam, Jonny, Jess, Carlos, Dean, Liz, Carl, Laura and Cat and others it wouldn't have been half as much fun especially at the infamous tour guide parties!!!

David Foley, Rob Senior and Paul Elliot all get a massive thank you for kindly agreeing to go through and proof read this thesis!!

I've got to mention my amazing group of friends who have just about managed to keep me sane during these four years!! From my undergrad days Vic, Tom and Karl, past housemates Mackin, Rostron, Jillian and currently Nikita, of course my fabulous dancing girls Chisholm, Jefferson, Penny, Jude, Zoe, Hannah B, Andrea, Natalie, Cindy, Kaz and so many more I haven't listed; two of my oldest friends Sarah and Jenny who are still great friends despite Jen being on the other side of the world. Love you all!!

My thanks also go to my family. All my cousins, uncles, aunties and my grandma in Iran have provided me with so much love and support even though they live so far away and we only see each other every couple of years. I love you all to bits despite the language barrier that pops up from time to time!

However, my biggest thanks have to go to my mum and dad, Soraya and Richard, and to Samon, my not so little brother. You have provided me with so much love, support, kindness, help buying my first flat and of course all the food parcels ha ha! You convinced me to keep going and I can never thank you enough for what you have done for me during these four years never mind the past 22 years of my life!! I love you all so much!!

List of Abbreviations

Chemical

HDA	Hexadecylamine	$CH_3(CH_2)_{15}NH_2$
OA	Oleic acid	$CH_3(CH_2)_7C=C(CH_2)_7COOH$
ODA	Octadecylamine	$CH_3(CH_2)_{17}NH_2$
ODE	1-Octadecene	$CH_3(CH_2)_{15}CH=CH_2$
TBP	Tri-n-butylphosphine	$[CH_3(CH_2)_3]_3P$
TDPA	Tetradecylphosphonic acid	$CH_3(CH_2)_{13}P(OH)_3$
TOP	Tri-n-octylphosphine	$[CH_3(CH_2)_7]_3P$
TOPO	Tri-n-octylphosphine oxide	$[CH_3(CH_2)_7]_3PO$
TOP-Se	Tri-n-octylphosphine selenide	$[CH_3(CH_2)_7]_3PSe$
TOP-Te	Tri-n-octylphosphine telluride	$[CH_3(CH_2)_7]_3PTe$
TOP-S	Tri-n-octylphosphine sulfide	$[CH_3(CH_2)_7]_3PS$

Techniques

MEG	Multi exciton generation
PL	Photoluminescence
QD	Quantum dot
QY	Quantum yield
TEM	Transmission electron microscopy
TGA	Thermogravimetric analysis
pXRD	Powder X-ray diffraction

CHAPTER 1 INTRODUCTION

1.1 Background

In general, solid materials classed as bulk can be put into three different categories based on their electrical properties. These are:

- Conductors – This is common for most metals. They have partially filled and fully unoccupied levels with similar energies containing a large number of mobile electrons which can move freely when an electric current is applied.
- Semiconductors – The valence band is filled with electrons and the unoccupied conduction band is separated by a small band gap (E_g). When the electrons absorb enough thermal or optical energy, larger than their band gap, they are able to jump from the valence band to the conduction band.
- Insulators – The valence band is also filled with electrons leaving the conduction band unoccupied however; the band gap is too large, greater than 4.0 eV, to allow thermally or optically excited electrons to jump.

A schematic drawing of the different band structures at 0 K is shown in Figure 1.1. The bottom band is the valence band and the highest band contains the outer electrons and is identified as the conduction band. The highest occupied energy level at absolute zero (0 K) is called the Fermi level (E_f).

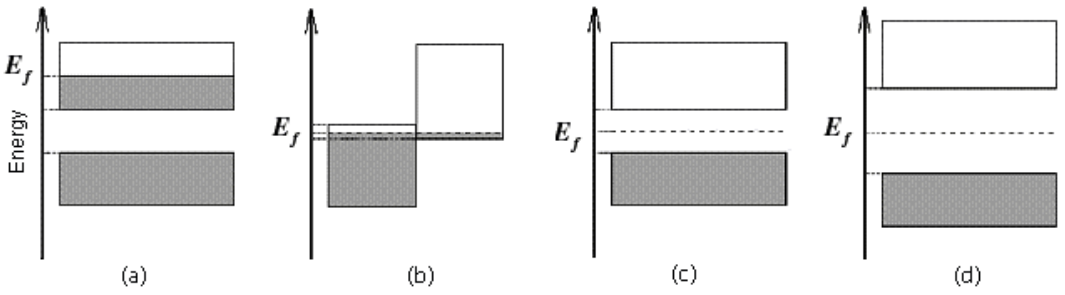

Figure 1.1 Schematic drawing of different band structures for solids at 0 K. (a) conductors, (b) semi-metals, (c) semiconductors, (d) insulators.

In Figure 1.1, semi-metals are also represented (b). These can also be classed as conductors but they differ from metallic conductors as there is an overlap of the filled and empty bands, meaning the electrons are free to move between the two bands.

Our work concentrates on semiconductors but on the nanoscale and I will explain why we are so interested in this area.

1.2 Why work on the nanoscale?

The properties of bulk materials are generally well understood. However, as the size of a particle decreases to between 1-100 nm every material can give many different materials each with its own properties. The property of the material is determined by the space available for the electrons to execute their characteristic motion. Therefore, the changes in physicochemical properties are observed as the size and shape changes.

As well as the physicochemical properties, there is a great deal of interest in terms of applications in nanotechnology. It has been estimated that the nanotech industry could be worth up to $1 trillion in the next 10-20 years.

1.3 What are Nanomaterials?

Nanomaterials have at least one dimension in the range 1-100 nm. The material can be zero dimensional (0D) to two dimensional (2D), with three dimensional (3D) being considered as bulk and a range of morphologies have also been observed. QDs, which are 0D, are controlled by the quantum effect; these include both their photoelectric and electric properties. Amongst the properties exhibited by QDs, the three important ones are:

1. The band gap can be tuned by changing the size of the material.
2. The thermal properties of the material can be changed greatly. Examples of these include the point at which a phase changes, for example the melting point.
3. The radiative lifetime ranges from tens of picoseconds to several nanoseconds for the lowest allowed optical excitation.

1.4 History of Nanomaterials

Although research and work with nanomaterials is still relatively new, nanoparticles have been used in art and pottery for many centuries. It has recently been found that luster decorations, typical of the Medieval and Renaissance pottery of the Mediterranean basin, substantially consist of a metal-glass nanocomposite thin layer.[1] The Romans also used luster decorations and an example of this can be seen in the Lycurgus cup which exhibits surface plasmon polaritons, Figure 1.2.

Figure 1.2 The Lycurgus cup. *Left:* Under normal light it appears green. *Right:* When illuminated from within it appears red.[1]

In more recent times the significance of nanoparticles in the scientific world were first realised by Michael Faraday who was the first to observe nanoparticles in the mid-19th century. He reported the preparation of colloids of relatively monodispersed gold.[2]

The physicist Richard Feynman is considered the father of modern day nanoscience after his groundbreaking and inspiring 'There's Plenty of Room at the Bottom' talk in 1959 about the physical possibilities for "making, manipulating, visualizing and controlling things on a small scale," and imagining that in decades to come it might be possible to arrange atoms "the way we want."[3] Research in this area has increased dramatically with the advent of scanning tunnelling microscopy in the 1980s with the power to allow us to see particles on the nanoscale.

1.5 Nanomaterial Morphologies

As seen in Figure 1.4 nanomaterials are available in a range of different dimensions. These are:

- Zero dimensional – nanoparticles/quantum dots which tend to be spherical in shape.
- One dimensional – nanorods and nanowires.
- Two dimensional – quantum wells and thin films.

1.5.1 Zero dimensional

Nanoparticles of semiconductors, also known as QDs, are particles with sizes which can range from 2-10 nm, 50-100 atoms, in diameter in colloidally grown quantum dots, or 10-50 nm in diameter for self-assembled quantum dots. QDs are zero dimensional (0D) and are a special class of semiconductors. They are classed as 0D because the motion of the bound pairs of electrons in the conduction band and the holes in the valence band are confined in all three spacial directions. This confinement can have several different aspects. A couple of examples include particles which have been shelled by a different material, where the interface can confine the electrons, or an electrostatic potential (caused by impurities, strain, doping or even external electrodes) or it can be caused by a combination of the two. As shown, the particles only contain a finite number of conduction band electrons and valence band holes.

1.5.2 One dimensional

Nanowires or nanorods are one dimensional, as the electrons in the conduction band and the holes in the valence band are confined in two spacial directions; however, free propagation in the third is allowed. It is generally accepted that one dimensional nanostructures have lateral dimensions in the range of 1 – 100 nm.[4] The general classification to differentiate nanorods and nanowires is that if the length of the material is less than approximately 200 nm then it is classed as a nanorod, however if the length is greater than 200 nm it is considered to be a nanowire. Anisotropic growth is the

preferential growth to a particular face or axis. The synthetic strategies currently known can be put into three categories:[5]

1. Anisotropic growth which is dictated by the crystallographic structure of the material.
2. Anisotropic growth which is confined and directed by various templates.
3. Anisotropic growth which is kinetically controlled by supersaturation or through the use of an appropriate capping agent.

1.5.3 Two dimensional

Quantum wells and thin films are two dimensional as the motion of the electrons and holes is only confined in one direction and free propagation is allowed in the other two.[6]

Thin films have one dimension in the nanoscale and generally have two dimensions which are much larger than nanoscale. Quantum dot quantum wells (QDQW) possess greater photochemical stability than ordinary quantum dots. It has been revealed that QDQWs are preferentially tetrahedral particles with a zinc blende crystal lattice.[7] A specific feature of the QDQWs is the considerable difference in the effective-mass parameters between the well and the barrier materials on the interfaces of the thin layer of the well. Another is the coupling of the conduction band with the valence band in the well, due to a small value of the band gap.[8] They are a special case of core/shell/shell systems in which a higher band gap core is shelled with a lower band gap material and then again with a higher band gap material, with both materials having type I alignment, for example ZnS/CdSe/ZnS.[9] The first system studied was CdS/HgS/CdS.[10] An 'inverse' QDQW structure has been realized with the synthesis of CdSe/ZnS/CdSe NCs. In this system the lower band gap material sandwiches the larger band gap in the middle.

1.6 Nanoparticles as Semiconductors

The potential use of nanoparticles as semiconductors was realised as their properties differ from bulk semiconductors. This was first considered by Ostwald in a

publication translated into English called “The World of Neglected Dimensions.”[11] When materials are arranged in bulk, their electrons have a range of energies which are found in different energy levels. Due to their packing, an almost infinite lattice of molecules can be formed, leading them to possess an infinite number of energy levels. These energy levels make up the valence and conduction bands which are separated by a region of forbidden electron energy known as either an energy or band gap. Materials normally considered as semiconductors typically exhibit band gaps in the range 0.3 - 3.8 eV.[12] The energy levels are so close together they can be described as continuous and the band gap for the particular material is fixed. This means that the addition of an atom would be barely distinguishable and make an immeasurable difference to the band gap.

Nanocystalline semiconductors exhibit different properties due to two fundamental factors. They possess a high surface to volume ratio and the actual size of the particle can determine the electronic and physical properties of the material.[13] The band gaps are size dependent but only when they are smaller than the bulk-exciton Bohr radius, which varies for different materials. Once the particles are of nano dimensions the energy levels can no longer be described as continuous and are instead discrete, due to the small and finite distance between them. This means that the removal or addition of a few atoms will change the band gap and essentially the wavelength emission. The discrete energy levels are known as quantum confinement. The materials no longer resemble bulk and can be described as a quantum dots. Quantitatively speaking, the band gap which determines the energy of the fluoresced light, is inversely proportional to the square of the size of the quantum dot. Large quantum dots have more energy levels which are more closely spaced, meaning that it allows the quantum dot to absorb photons containing less energy. This means that they are closer to the red end of the spectrum. As the dots get smaller a blue shift is observed as the band gap gets larger and there are less energy levels present (Figure 1.3).

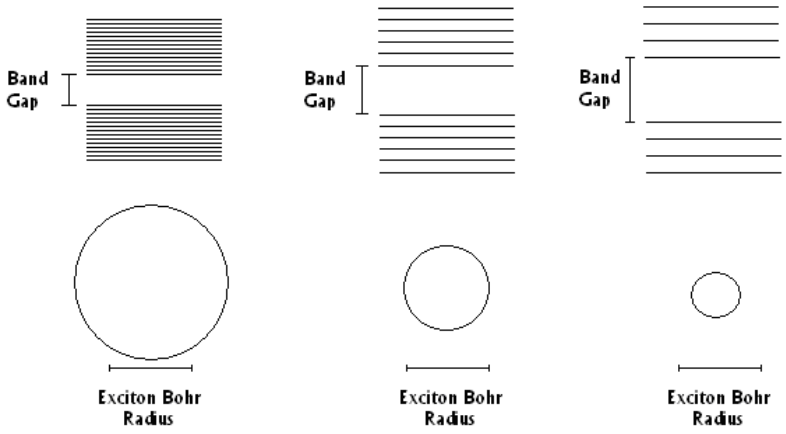

Figure 1.3 The band gap is tuneable once the particle is equal to, or smaller than the exciton Bohr radius.

Since the band gap increases as the size of the particle decreases, the dimensionality of the particles is an important factor as this can affect the size of the band gap. As the dimensions of the materials decrease from 3D to 0D the energy difference between the valence and conduction band increases.[15] Figure 1.4 shows the effect of this schematically.

Similar to the 'particle in a box' theory of elementary quantum mechanics, the Schrodinger wave equation[14] can be solved for an electron and hole in a box having either 1D, 2D, 3D and spatial dimensions of the order of the Bohr radius of the electron, hole or exciton (electron-hole pair).

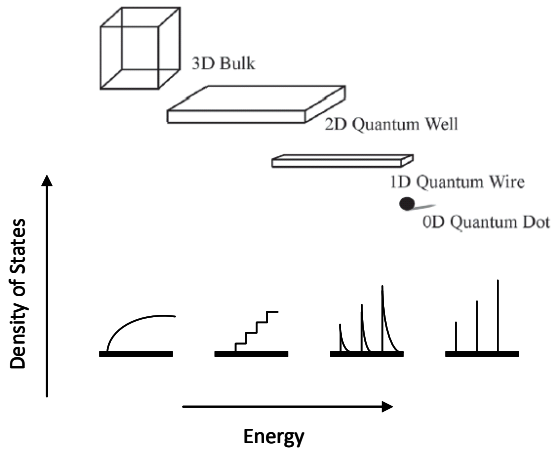

Figure 1.4 Density of states in one band of a semiconductor as a function of dimension.[15]

The density of states alters from the parabolic shape of the 3D bulk materials, first to a 2D stepped parabola, then to a 1D inverse stepped parabola and eventually to a 0D discrete form.

1.7 Types of Semiconductors

There are two different types of semiconductors; these are direct and indirect semiconductors. A number of examples can be seen in Table 1.1.

Type	Semiconductor	Lattice Parameters (Å)	Band-gap (eV)	Direct/Indirect
II-VI	ZnS	5.420	3.68	Direct
II-VI	CdS	5.832	2.42	Direct
II-VI	ZnSe	5.669	2.70	Direct
II-VI	CdSe	6.050	1.70	Direct
II-VI	CdTe	6.428	1.56	Direct
III-V	GaP	5.451	2.26	Indirect
III-V	AlAs	5.661	2.16	Indirect
III-V	GaAs	5.643	1.42	Direct
III-V	InAs	6.058	0.36	Direct
IV-VI	Si	5.437	1.12	Indirect
IV-VI	Ge	5.646	0.66	Indirect
IV-VI	PbS	5.936	0.37	Direct
IV-VI	PbSe	6.124	0.27	Direct
IV-VI	PbTe	6.462	0.29	Direct

Table 1.1 Lattice constants and band gap values of commonly used semiconductor materials.[16]

A direct band gap is when the conduction band lies directly above the valence band in momentum space (Figure 1.5a). Electrons on the threshold of the conduction band, whilst maintaining their momentum, can combine directly with holes in the valence band. This means that when they return to the conduction band the energy will be emitted in the form of a photon of light. This is called radiative recombination or spontaneous emission and means that direct semiconductors have optical properties and large absorption coefficients. An example of a direct semiconductor is gallium arsenide. The relationship between the absorption coefficient and the photon energy of a direct transition near the threshold can be represented by Equation 1.1.

$$\alpha\,(h\nu) \propto (E_g - h\nu)^{1/2} \qquad \textbf{Equation 1.1}$$

Where α is the absorption coefficient, *h* is Planck's constant, ν is wavelength and E_g is the band gap.

Indirect semiconductors are systems in which the transition of the electron between the conduction and valence band is formally forbidden as it is not a direct transition across the band gap (Figure 1.5b). Electrons therefore require more momentum to overcome the offset between the conduction and valence band. Electrons are unable to maintain this momentum causing non-radiative recombination to take place at point defects or grain boundaries on the surface. To help conserve momentum a third body can be introduced, such as a phonon or a crystallographic defect, therefore preventing the excited electrons reaching the non-radiative recombination sites. The electrons therefore have to return to the valence band by radiative recombination. Indirect semiconductors are inefficient at emitting light and have small absorption coefficients, with an example being silicon.

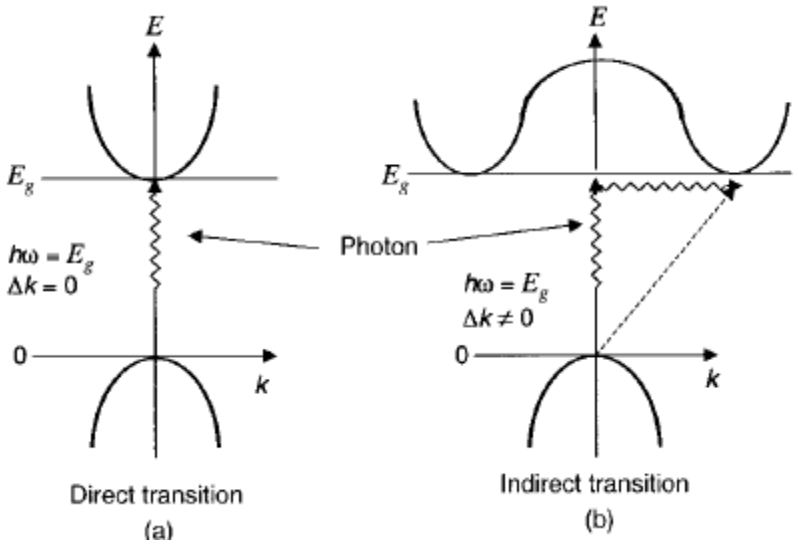

Figure 1.5 Excitation across the band gap by photon absorption (a) Direct process; (b) Indirect process.[16]

The conductivity of semiconductors increases with temperature as the electrons have more energy with which to be excited into the conduction band. When the electron moves to the conduction band it leaves behind a hole in the valence band. In a pure semiconductor, the number of electrons in the conduction band must be equal to the number of holes in the valence band. The conductivity of the semiconductor is also dependent on whether the semiconductor is intrinsic or extrinsic. An intrinsic semiconductor is said to be a pure semiconductor as it is crystalline with no defects. This means that there are an equal number of positive and negative charge carriers therefore displayng conduction based on properties inherit to the material. Extrinsic semiconductors are generally formed from intrinsic semiconductors by a process called doping, i.e. they possess unequal electron-hole concentrations.

1.8 Doping of Semiconductors

The purposeful addition of an impurity to an intrinsic semiconductor is a process known as doping and an extrinsic semiconductor is formed. This impurity can alter the electronic properties of the semiconductor as the addition of doping atoms changes the electron and hole carrier concentrations of the semiconductor at thermal equilibrium. The

electrical properties of extrinsic semiconductors are an important component of many electrical devices.

There are two main types of doped semiconductor, n-type and p-type. Doping of a semiconductor can alter the properties so much as to make it act as a conductor and this type of semiconductor is known as degenerate. The percentage of the impurity compared to the amount of material making up the semiconductor is very small in the order of approximately 1 atom of impurity in every 100,000,000 atoms. N-type semiconductors contain a pentavalent impurity, which means that they will contribute one extra electron. Examples include antimony, arsenic and phosphorus. The addition of extra electrons means that conductivity of the intrinsic semiconductors increases because there are extra electron levels so they can easily be excited to the conduction band (Figure 1.6). Cadmium sulfide is also an n-type semiconductor due to sulfur containing vacancies within the crystal lattice.

P-type semiconductors contain a trivalent impurity making the system deficient of an electron, therefore producing a hole. Examples include boron, aluminium and gallium. These holes are free to move which also means that the semiconductor becomes electrically conductive (Figure 1.6).

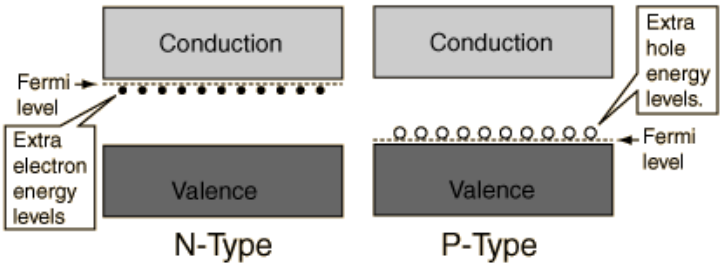

Figure 1.6 The valence and conduction band for n-type and p-type semiconductors.

Compound semiconductors can therefore be either n- or p-semiconductors. This is due to defects within the crystal lattice and the implied deviation from stoichiometry of component elements.

1.9 Classification of Core/Shell systems

Most of the work in this thesis concentrates on the synthesis of core/shell (CS), core/shell/shell (CSS) or quantum dot quantum well (QDQW) semiconductors. There are several qualitatively different possibilities for the alignment of the band edges (Figure 1.7). These are:

- Type I: In type I systems the band edge of the core may lie below the conduction band of the shell, whilst simultaneously the valence band of the core may lie above that of the shell. Therefore the band gap of the core lies entirely within the gap of the shell. Both the electrons and holes are confined in the core. An example of this is CdSe/ZnS or alloy materials, for example $Cd_{x-1}Zn_xSe_{1-y}S_y$.

- Type II: In type II systems the conduction and valence band edges of the core are respectively, below the two edges of the shell. The staggering of the valence and conduction band leads to the excitation of the nanocrystals to a spatial separation of the hole and the electron in different regions of the core/shell structure. An example of this is CdTe/CdSe.

- Type III: these are heterojunctions of type I with a zero energy gap in the core.

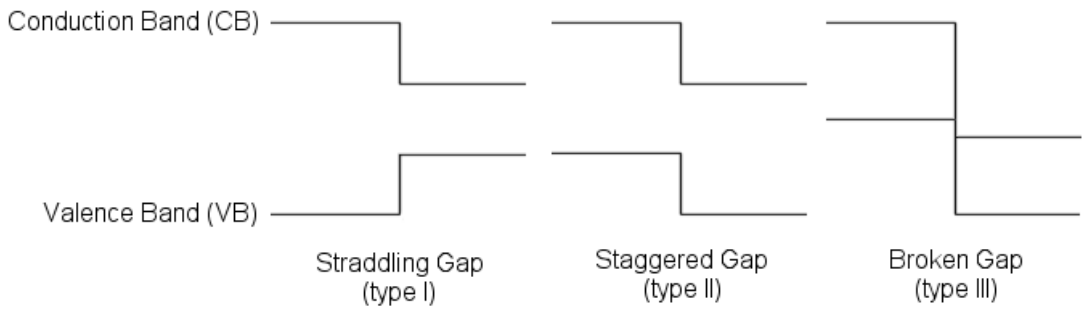

Figure 1.7 The qualitatively different possibilities for the line up of the band edges.

Depending on the position of the electronic energy levels the shell can have different functions in core/shell nanocrystals. The band alignment of the bulk materials usually used in nanocrystalline synthesis is shown in Figure 1.8.

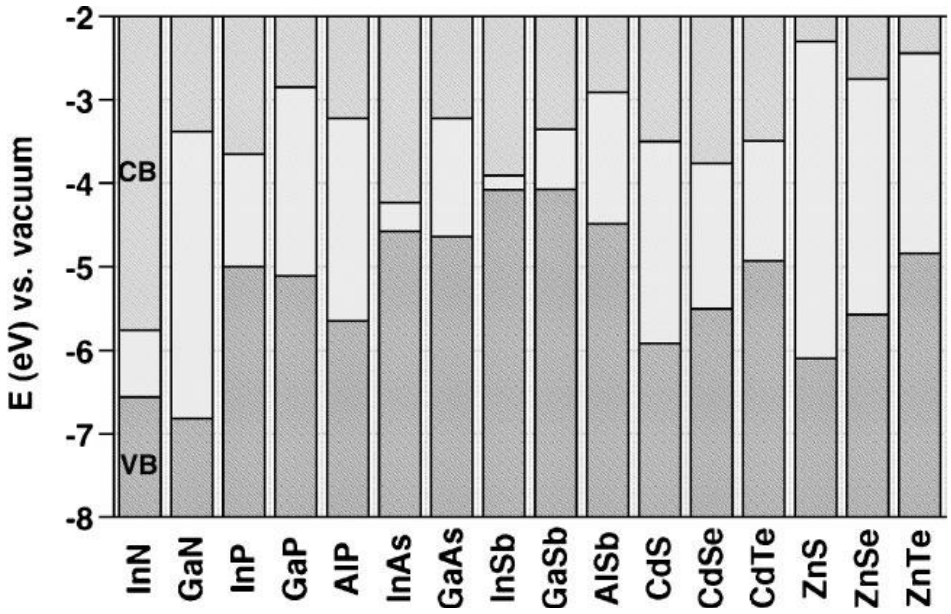

Figure 1.8 Electronic energy levels of some III-V and II-VI semiconductors using the valence band offsets. (VB: valence band, CB: conduction band).[17]

1.10 Structures of Semiconductors

A lattice is a regular array of lattice points in three dimensions. An infinite lattice of spheres is arranged so that it will take up the greatest possible fraction of an infinite 3-dimensional space. This is called close-packing. Carl Friedrich Gauss proved that the highest average density that can be achieved by a regular lattice arrangement is shown in Equation 1.2.[18]

$$\frac{\pi}{3\sqrt{2}} \simeq 0.74048$$

Equation 1.2

The Kepler conjecture states that this is the highest density that can be achieved by any arrangement of spheres both regular and irregular.[18]

There are only two types of packing that are able to achieve the highest average density. These are face-centered cubic (fcc), sometimes known as cubic close packing (ccp), and hexagonal close-packed (hcp) and their names arise from their symmetry, see Figure 1.9.

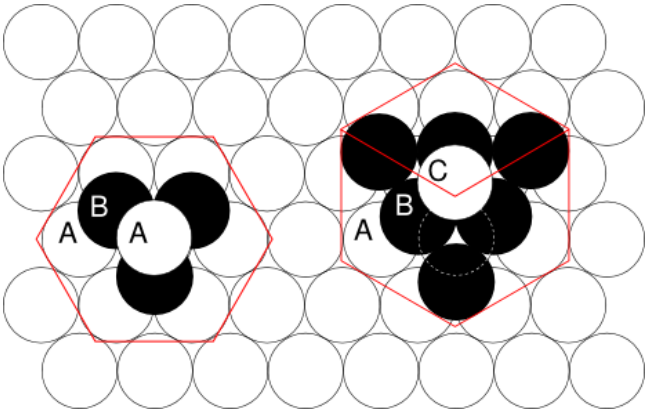

Figure 1.9 The two different types of lattice. HCP (left) and FCC (right).[19]

In both arrangements for every sphere there is a large gap which is surrounded by another six spheres, octahedral, and two smaller gaps surrounded by four spheres, tetrahedral, Figure 1.10. Therefore, each sphere has twelve spheres around it and is said to have a coordination number (CN) of 12 and an atomic packing factor of 0.74.

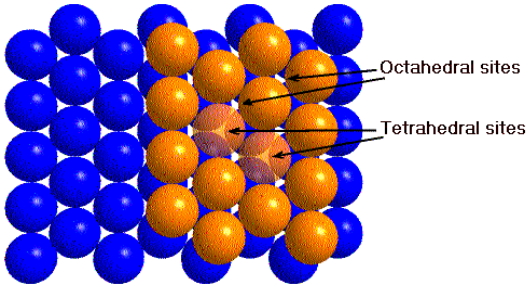

Figure 1.10 Layer A and Layer B, showing both octahedral and tetrahedral sites.[20]

The fcc arrangement is denoted as ABCABC. In Figure 1.10 there is an option for the third layer to arrange the spheres on either the right or left interstices. If the sphere is placed over the right interstice then the layer C is generated but if it is placed over the left interstice then it is the same as the first layer and denoted as A again. When we have a repeating arrangement of ABABAB it is an hcp arrangement.

If there are only 3 layers the third layer in the hcp arrangement is directly above the first layer, however in the fcc arrangement they are staggered. The side view of both systems is shown in Figure 1.11.

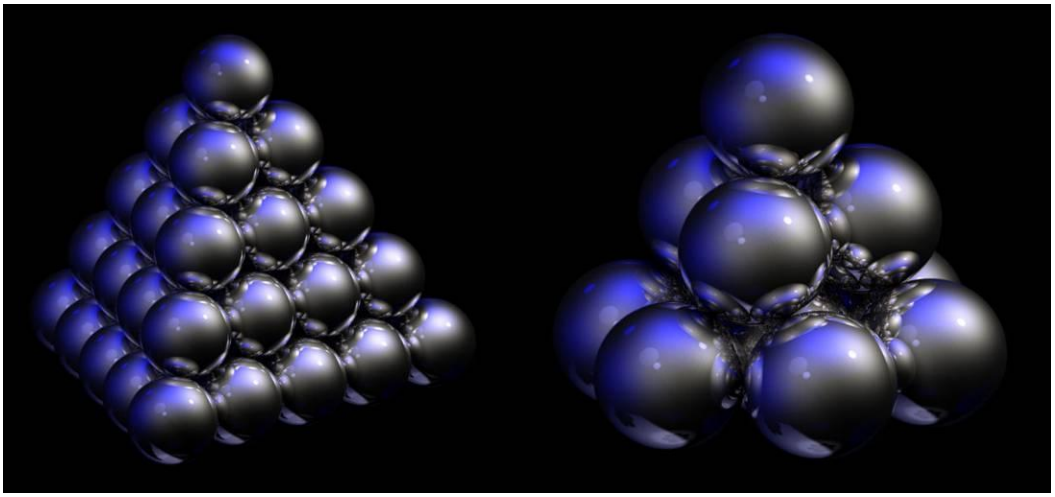

Figure 1.11 Three-dimensional image of fcc (left) and hcp (right) arrangements.[19]

1.11 Growth Methods

The synthesis of nanomaterials is commonly thought of in two terms, 'bottom-up' or 'top-down' processes.[21]

Top-down methods start with large subunits, bulk material, which is then broken down in a more or less controlled fashion using mechanical, chemical or other forms of energy. The majority of microfabrication techniques for inorganic materials, including lithography and milling techniques, fit this description. Applications of nanomaterials prepared by these methods are few. This is because, as expected, particle size and morphology cannot be easily controlled and results would be non-reproducible.

Bottom-up approaches can be used to synthesise some inorganic structures by starting with small subunits that are assembled with varying degrees of control, depending on which method is being used. Control over size distribution and morphology is possible, therefore these methods are preferable to top-down methods. Other advantages of bottom-up over top-down include simple processing steps which can be scaled up to synthesise reproducible monodisperse nanomaterials.

1.11.1 General Nanoparticle Synthesis

The general procedure observed during the synthesis of nanoparticles in solution after the initial nucleation and growth is Ostwald ripening.[22] Generally, Ostwald ripening is

seen as a negative process, for example in sintering of polycrystalline materials, as it results in abnormal grain growth leading to inhomogeneous microstructure and inferior mechanical properties of the products. However, in the synthesis of nanoparticles, Ostwald ripening is used to narrow the size distribution of nanoparticles by the elimination of small particles. A simple schematic of this process is shown in Figure 1.12.

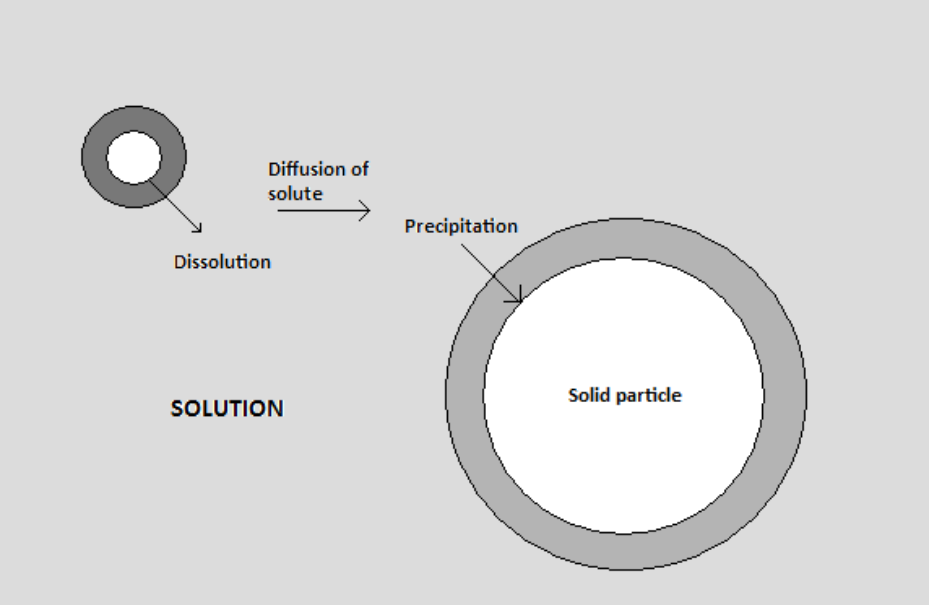

Figure 1.12 Schematic illustrating the Ostwald ripening process. To maintain the local concentration of equilibrium the smaller particles dissolve into the solution. Solute in close proximity to small particles diffuses away and solute at proximity of large particles deposits. The process continues until all the small particles disappear.[22]

Ostwald ripening can be promoted by varying processing temperatures. Ostwald ripening occurs after the initial nucleation and subsequent growth. Generally in nanoparticle synthesis a capping agent is also in the solution to pacify the particle and to increase steric stability. Once the concentration of the material in the solution is equal to the solubility of the larger particles the growth process stops and Ostwald ripening begins allowing the larger particles to increase in size.[23]

Ostwald ripening is a thermodynamically driven process because larger particles are more energetically favoured than small particles. This is due to the surface molecules having unsatisfied surface bonds which leads them to experience an inward force, causing them to be less energetically stable when compared to the well-ordered interior of the particle. Therefore, kinetics will mean that it is easy to nucleate many small crystals but as they have a larger surface area to volume ratio when compared with the larger crystals, the

small crystals will have a greater ratio of unsatisfied bonds. This will lead to the dissolution of the smaller particles into the solution, diffusing towards the larger crystals and depositing on the surface, causing them to increase in size and become even more thermodynamically stable.

As the small crystals decrease in size van der Waals attraction forces and Brownian motion play important roles. Van der Waals forces become significant when the particles are very close together due to its weak nature and Brownian motion ensures that the particles are colliding with each other all the time. The combination of these causes agglomeration, which for the synthesis of nanoparticles needs to be prevented, as once the particles agglomerate they become difficult to disperse. To prevent agglomeration steric or electrostatic stabilization can be implemented. As this thesis only deals with steric stabilization, electrostatic stabilization will not be discussed.

Steric stabilization has many advantages over electrostatic stabilization including:

- The very high concentration that can be accommodated and the dispersion medium can be completely depleted.
- It is a thermodynamic stabilization method meaning that the particles are always redispersible.

Steric stabilization is the method commonly used by scientists synthesising nanoparticles by colloidal methods (discussed in Section 1.11.2). Steric stabilization, also known as capping, can be used for other nanomaterials, for example nanorods, nanowires and nanowafers. The polymer adsorbs onto the surface of the nanoparticles causing a steric barrier which prevents agglomeration and causes diffusion-limited growth. This reduces the size distribution of the initial nuclei, leading to monodispersity of the nanoparticles synthesised. The two main methods of interaction are:

1. An anchored organic stabilizer – it adsorbs irreversibly by one end only and examples include trioctylphosphine oxide (TOPO), Figure 1.13, and primary amines.
2. Adsorbing organic stabilizers – they adsorb at multiple, unregulated points along the polymer and can effectively form bridges between particles.

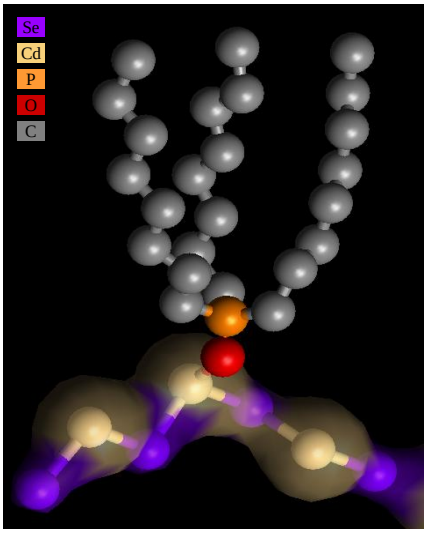

Figure 1.13 TOPO acting as an anchored organic stabilizer on CdSe.

Both methods are heavily influenced by the reaction solvent. The next section describes different methods for the growth of nanoparticles.

1.11.2 Colloidal Chemistry

During the past century colloidal chemistry has been well studied and cadmium sulfide nanoparticles were first synthesised by Brus *et al.* using this method.[24] Colloidal chemistry was the first reported method for producing colloids which were synthesised by controlled precipitation of dilute colloidal solutions of monodispersed sulfur hydrosols and the rapid termination of growth following nucleation.[25] To control high ratio of nucleation to growth, the reactions are carried out at a low temperatures; for example Brus *et al.* carried out their reactions at temperatures as low as -77 ^{o}C to synthesise very small ZnS and CdS crystallites.[26] The disadvantage of this method is that the particles grown have poor crystallinity and agglomerate when annealed, because surface passivation has been insufficient. This would lead to poor quantum yield as these factors result in deep trap luminescence in the nanocrystals formed by this method. Another disadvantage of this reaction is that it cannot be scaled up as monodispersity is only achieved when synthesised in dilute solutions. Fendler *et al.* have made progress with this method so that it is not restricted only to dilute solutions.[27]

1.11.3 Single source precursor approach

The single source precursor approach is the thermal decomposition of a molecule that contains both the metal and chalcogenide required for the synthesis of the metal chalcogenide nanoparticles. This method was first used by Steigerwald *et al.* 20 years ago.[28] The CdSe nanoparticles they isolated were synthesised from $Cd[Se(C_6H_5)]_2$ or $[Cd(SePh)_2][Et_2PCH_2CH_2PEt_2]$ whilst refluxing in pyridine. This was the starting point for using single source precursors however the QDs synthesised *via* this method were still large. The size distribution was also broad due to the lack of a capping agent which caused the nucleation and growth period to occur simultaneously. O'Brien *et al.* have optimised this method using precursors with the general formula $M(E_2CNR_1R_2)_2$ where M = Zn or Cd, E = S or Se and R = Me, Et or Hex. The precursors were thermolysed in high boiling point solvents, for example TOPO or 4-ethylpyridine, which can be also used as capping agents to prevent agglomeration.[29] Using similar techniques this group have also synthesised nickel selenide or phosphide nanoparticles;[30] cadmium phosphide;[31] zinc selenide;[32] lead selenide nanoparticles from $Pb(Se_2CNEt_2)_2$ and $Pb(Se_2CNMeHex)_2$;[33] copper selenide from $Cu(Se_2CNEt_2)_2$[34] and indium sulfide and selenide from $In(E_2CNEt_2)_3$ where E = S or Se, respectively.[35]

The advantages of using single source precursors include:[36]

- The precursors are both air and moisture stable even if the nanoparticles that they form are not.
- By using one precursor the need for using pyrophoric, toxic or volatile precursor routes is not necessary.
- Using one precursor reduces the amount of potential impurities in the reaction, allowing easier purification.
- The core structure of the precursor molecule's phase can be controlled during growth.

1.11.4 Organometallic Chemistry

First reported by Bawendi *et al.,* in 1993, organometallic chemistry still remains a very popular method for the formation of good quality CdE nanoparticles, where E = S, Se

or Te.[37] This method utilises TOPO as both a solvent and capping agent in the thermolysis of Me_2Cd and $E[Si(Me)_3]_3$ at temperatures ranging from 120-250 ^oC. Once the particle has grown to the required size, the reaction is cooled to approximately 60 ^oC and the particles are isolated using either methanol or ethanol. The polar solvent causes the particles to preciptate so that they can be collected by centrifugation. The powder that is collected is capped with TOPO thus allowing the re-suspension in an organic solvent. Many other examples of alkylmetallic compounds being used to synthesise other semiconductors and for shelling can be found.[38-40]

The key disadvantage of this route is the nature of the starting materials as they are pyrophoric and very toxic. This makes them difficult to handle and unamenable to industrial application. In recent years, to combat these problems, synthetic routes have started to move away from organometallics and towards greener methods.

1.11.5 Green Chemistry

As nanochemistry is becoming more main stream, efforts have begun to make this chemistry greener, i.e. moving away from using pyrophoric and toxic starting materials (e.g. Me_2Cd). Over the past few years, shelling methods,[41] alloy synthesis[42] and nanoparticles production[43] have all been undertaken using air stable materials at relatively low temperatures of 190-230 ^oC. Cadmium oxide and cadmium stearate are examples of non-pyrophoric starting materials that can be used to synthesise cadmium based nanoparticles. Zinc stearate can then be used to synthesise zinc xanthate which can be employed to shell nanoparticles with ZnS. High quantum yields (QYs) have been reported using these techniques meaning that the quality of dots is not diminished.[44-46] These reactions have not been limited to small scale, as a large scale synthesis of CdSe nanoparticles produced almost 10 g of product in high yield. This demonstrates that the chemistry is viable for industrial application.[47]

1.11.6 Direct Injection Method

A common method for synthesising nanomaterials is *via* a direct injection. A large majority of the experiments reported in this thesis employed this method. A single source precursor or multiple precursors are injected into the solvent which tends to contain one of

the reactant materials. The role of the precursor dictates the speed at which it is injected into the reaction vessel. If the precursor is to be used to synthesise the core material, it is injected rapidly (less than 1 s). If the precursor is to be used for shelling purposes it needs to be added slowly (e.g. over the period of an hour). The general procedure for direct injection follows these steps:

1. The solvent, e. g. TOP, TOPO, HDA, capping agent and generally one of the starting materials if more than one precursor is being used, e. g. CdO, PbO, are degassed under vacuum.
2. The reaction mixture is heated to the desired temperature under an inert atmosphere.
3. The precursor (e. g. TOP-Se) is injected, into the reaction mixture.
4. The temperature is adjusted to the growth temperature and left for a given length of time.
5. The reaction is then cooled to stop growth.
6. The particles are isolated by addition of polar solvent(s), which causes the particles to precipitate.
7. The particles are collected by centrifugation.

Once isolated, the particles are characterised using several techniques, which are discussed in the next two sections.

1.12 Optical Properties

1.12.1 Absorption

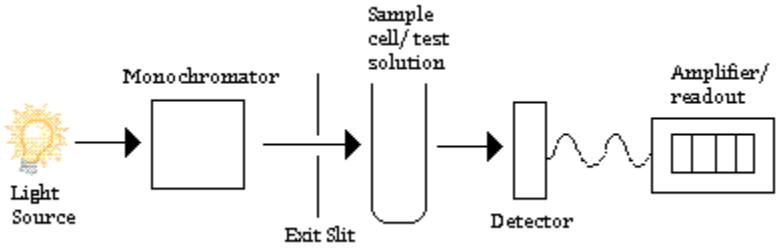

Figure 1.14 Components of a UV/Visible spectrophotometer.[48]

As has already been discussed the band gaps between the highest valence band (HOMO) and the lowest lying conduction band (LUMO) in bulk semiconductors can be described as continuous as the energy levels are so close together and result in broad peaks. However, on the nanoscale the band gaps are now described as discrete as they have a small and finite distance between them, meaning that their absorption and emission peaks will be sharp. Due to the discrete energy levels the photon energy can be accurately determined and used to measure the band gap energy of a semiconductor.

To excite electrons into the conduction band excess thermal energy is generally used as the source; however when the energy provided to excite the electrons is delivered by incident photons then this process is referred to as optical absorption. Optical absorption is the process which results in photoluminescence and photoconductivity.

The principal components of a UV/Vis spectrophotometer are shown in Figure 1.14. The light source is a high intensity tungsten bulb which can operate in the visible region (400-700 nm). Deuterium lamps are used for detecting peaks in the UV region (200-400 nm). These lamps are fitted with quartz rather than glass envelopes due to glass being opaque to UV radiation. The monochromator is used to convert the light source's polychromatic light to a parallel beam of monochromatic light using a diffraction grating. In practice, the light emitted is not of a single wavelength but within a narrow band of wavelengths. This bandwidth is affected by the width of the exit slit which is generally no more than 10 nm; however on some spectrophotometers this can be less than 1 nm. By reducing the size of the slit the bandwidth is reduced, however this then reduces the

amount of light reaching the detector, decreasing the signal-to-noise ratio. Therefore, when deciding the slit width, the sensitivity and stability of the detection/amplification and the presence of stray light must be taken into account. The optical path length (l) of the cuvettes used is 10 mm and made from quartz so that wavelengths in the UV can also be detected.

The two principles that govern the absorption of light passing through a solution are:

1. The absorption of light is exponentially related to the number of molecules of the absorbing solute that are encountered, i.e. the solute concentration [*C*].

2. The absorption of light is exponentially related to the length of the light path through the absorbing solution, [*l*].

These two principles are amalgamated in the Beer-Lambert relationship,[49] Equation 1.3, which is expressed in terms of the intensity of the incident light (I_o), transmitted light (I_t) and where ε is the molar absorptivity, a constant unique to a given molecule.

$$A = \mathrm{Log}_{10}(I_t/I_o) = -\varepsilon l C \qquad \textbf{Equation 1.3}$$

Figure 1.15 is a simple representation of the Beer-Lambert absorption law, showing a beam of light being attenuated as it travels through a cuvette.

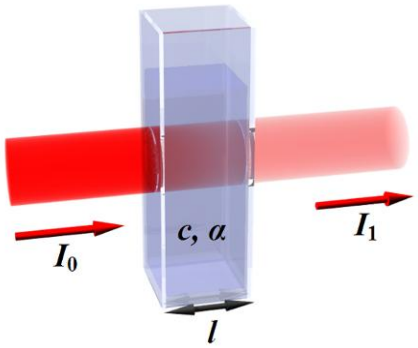

Figure 1.15 A simple representation of the Beer-Lambert law of absorption, showing a beam of light being attenuated as it travels through a cuvette.

1.12.2 Luminescence

Luminescence is the emission of light by a material at room temperature or lower, 'cold light.' Electrons move from the ground state, valence band, into an excited state, conduction band, by an energy source that is not heat. There are many forms of luminescence, but due to the characteristics shown by the nano sized semiconductors, photoluminescence (PL) is a powerful tool for determining quantum confinement and homogeneity. The process of PL is the absorption of photons (electromagnetic radiation) by a substance and then re-emission of the photons. This means that electrons are excited to a higher state and when they return to a lower energy state the energy is released in the form of a photon which is emitted. It is a non-destructive, non-contact method of probing the electronic structure of materials.

In the work carried out for this thesis, the emissions differed greatly and one of the reasons can be due to surface effects of the nanoparticles synthesised. If surface traps, caused by surface defects on the nanomaterials are not dealt with, electrons in the conduction band will lose energy by going *via* surface traps before returning to the valence band. This is instead of returning straight to the valence band as in the case of direct emission. Figure 1.16 shows the possible paths electrons can take, resulting in non-radiative relaxation, direct emission or a loss of PL via surface traps.

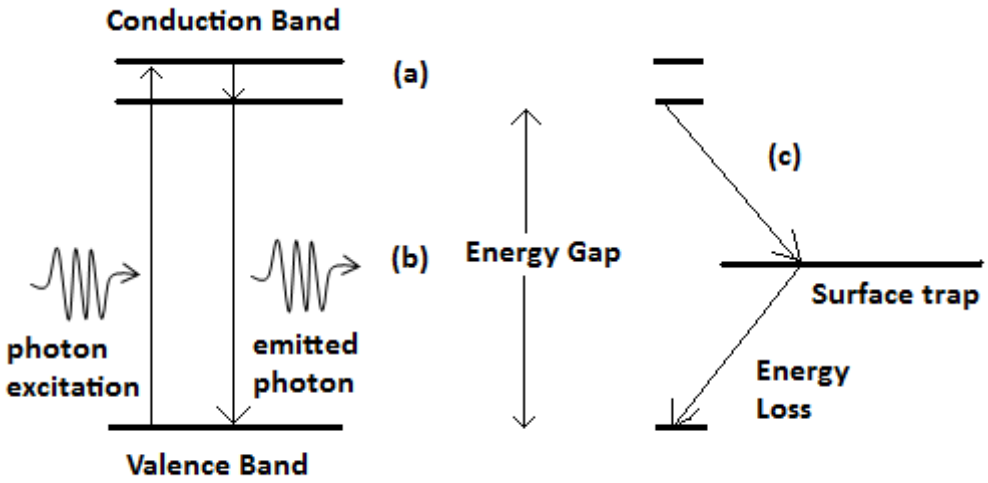

Figure 1.16 (a) Non-radiative relaxation to LUMO; (b) direct emission to ground state, emitting a photon; (c) surface trap disrupting direct emission causing energy loss.

Despite bulk semiconductors recombining almost exclusively via trap states, surface traps affect nanocrystalline semiconductors in a negative way.

The size of the QDs determines where the PL peak will emit. As the QDs become larger a red shift is observed because of the band gap becoming smaller. Once the semiconductor is classed as bulk material there is a large red shift and it can no longer be observed in the visible region.

The ideal PL peak for QDs is sharp and narrow; however broad peaks are sometimes observed and this is caused by either homogeneous or inhomogeneous broadening. Inhomogeneous broadening is more generally observed when there is a large size distribution. The size distribution affects the width of the peak because the band gap is directly related to the size of the particle, therefore a broad peak suggests there is a large size distribution of the QDs grown. Homogeneous broadening is caused by the intrinsic physical properties of the material. This is independent of size distribution and can affect both the width and shape of the PL peak.

1.12.3 Fluorescent intermittency

Fluorescent intermittency, also known as blinking, in emission is common but at the same time it is not a process confined only to QDs. Fluorescent intermittency is observed in dye molecules, fluorescent proteins, single polymer segments, porous silicon and light harvesting complexes. Bohr in 1913 proposed a simple molecular model for this behaviour which was refined in 1985 by Cook and Kimble.[57] It suggests that there is fast fluorescence cycling between ground and excited states, followed by random 'jumps' to a non-fluorescent triplet state which eventually recovers to the ground state (Figure 1.17). This means that this process could reflect the rate of localization of photogenerated carriers into a 'dark' or 'off' exciton state.[51] To return to the 'on' state, slow single exponential decay occurs with a rate (γ). This recovery process could possibly be due to the recombination of trapped carriers.

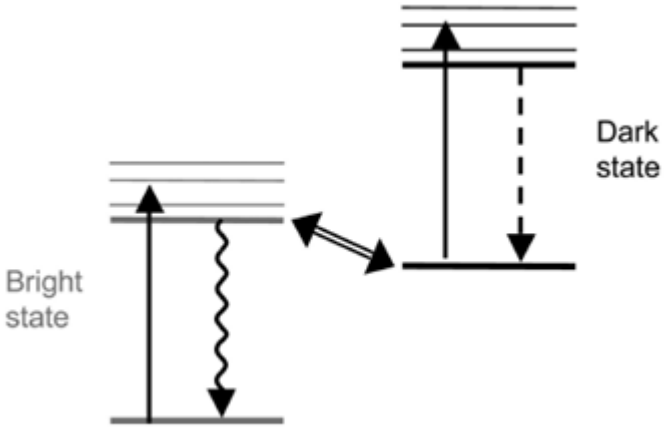

Figure 1.17 Schematic of the states involved in QD blinking. The dot is excited from a lower-energy to a higher-energy state by the absorption of a photon. If the dot is in a bright state, relaxation occurs by photon emission; if it is in a dark state, relaxation occurs by a non-radiative mechanism. Blinking corresponds to transitions between the bright and dark states.[52]

Interest in blinking was stimulated in 2000 when Kuno *et al.* observed that the duration of bright and dark periods follow power-law statistics. This can be more specifically described by probability densities of the form shown in Equation 1.4 where ν is between 0.4 and 1.0.[52] The power law behaviour is unaffected by temperature,[53] QD size or composition,[54] nanoparticle shape[55] or excitation intensity.[56]

$$\rho(t) \propto t^{-(1+\nu)} \qquad \textbf{Equation 1.4}$$

An Auger ionization model was proposed to explain fluorescence intermittency.[57] The process is basically a two-carrier process formed by closely timed absorption. Efros and Rosen have theoretically modelled Auger ionization of single CdSe quantum dots.[58] The model shows how neighbouring carriers can gain energy from a non-radiative recombination so that it has enough energy to eject the remaining electrons. This causes the quantum dot to become ionized.

Neuhauser *et al.* have reported a relationship between ensemble spectral broadening and fluorescence intermittency.[59] On and around an ionized nanocrystal's surface, charge redistribution varies the electric field within the quantum dot and this causes a spectral drift in the single dot spectrum. On a larger scale, the shifts in emission wavelength broaden the ensemble emission spectrum. QDQWs reduce the Auger process and can even possibly eliminate it completely.

Fluorescence intermittency is not observed when large amounts of QDs are used but the reason why this process is important to understand is because single dot spectroscopy can be used to investigate spatially heterogeneous samples, one dot at a time. Where most optical measurements tend to average the results, single dot spectroscopy allows us to eradicate ensemble averaging.

Recently, novel CdSe/CdS QDs have been synthesised where 68% of them do not blink when observed individually at 33 Hz for 5 minutes due to their thick crystalline shell. A thick CdS shell, 5 nm thick, is grown on small CdSe cores, 2.5 nm, leading to a homogeneous population of 13 nm core/shell nanoparticles. The small lattice mismatch (4%) leads to very homogeneous crystal structures, as core/shell nanoparticles with larger lattice mismatches (CdSe/ZnS with a lattice mismatch of 10%) cannot exhibit the same level of crystallinity. Shell thickness strongly affects the blinking behaviour of QDs. This realisation allowed these novel QDs to be used in single molecule tracking and also in photonics as robust and continuous photon emitters.[60]

1.12.4 Quantum Yield

The quantum yield (QY) is the ratio of emitted to absorbed photons and is the measure of luminescence efficiency of QDs.

Two different methods were used to calculate QYs in this work. The first method was a comparative method between the unknown sample and a standard organic dye, e.g. rhodamine or coumarin, with a known QY. First the optical density (OD) is required which is found using the Beer-Lambert law (Equation 1.3) and the value should be less than 0.1. The OD of the solution may then be obtained by the following equation (Equation 1.5).

$$OD = Log_{10}[I_o/I_o-I_a] = Log_{10}\,1/[1-(I_a/I_o)] = -Log_{10}([1-I_a/I_o)] \qquad \textbf{Equation 1.5}$$

Where I_o is the incident light intensity and I_a is the absorbed light.

Once the OD has been acquired for both the unknown sample and the dye they are both then excited at the same wavelength. The area under the PL peak of the sample (A_X), the standard (A_{STD}), the QY of the standard (QY_{STD}) and the refractive index of the sample and standard solvent (n_X and n_{STD} respectively) can be entered into Equation 1.6 to calculate the QY of the sample (QY_X).

$$QY_X = QY_{STD} \times (A_X/A_{STD}) \times (OD_{STD}/OD_X) \times (n_X/n_{STD})^2 \quad \textbf{Equation 1.6}$$

A second method was applied for solid QD samples or those with an OD greater than 0.1. A photoluminescent spectrometer with an integrating sphere attachment was used. A background excitation and fluorescence emission spectrum, e.g. the solvent being used or empty polystyrene microspheres, is obtained before the excitation and fluorescence emission spectrum for the QD sample is recorded. Inbuilt software can then be used to calculate the QY.

1.12.5 Multiple Exciton Generation (MEG)

This is the process of producing more than one electron-hole pair (exciton), in semiconductor materials, *via* excitation by an energetic photon. When photons with an energy larger than the band gap of the material are absorbed, the excess energy will be distributed between the electron and hole depending, upon their effective masses. These 'hot' carriers will then relax to the band edge through electron-photon scattering before emitting phonons. This heat loss can be identified as the dominant loss factor which limits the energy conversion. Conversion of energy is greater in nanomaterials when compared with bulk semiconductors due to the discrete energy levels, see Figure 1.19. Intraband spacing of hundreds of meV and carrier cooling *via* phonon emission can only occur through very inefficient multi-phonon processes. This is known as the phonon bottleneck and was expected to slow the cooling rate in QDs. Observations, however, have shown that the relaxation rate in QDs is still relatively fast compared to that expected due to the phonon bottleneck.[61] This problem has been explained in CdSe by an enhanced Auger cooling mechanism due to the quantum confinement and comparatively large coulomb interaction, in which the electron transfers its energy to the hole *via* scattering, which in turn relaxes to the band edge through the denser valence band states.[62] Crystal momentum, k, is not a good quantum number in QDs since confinement allows the position of the electron and hole to be known, Heisenberg's Uncertainty principle dictates that momentum is not. Thus the relaxation of momentum conservation, discrete energy spectra and enhanced coulomb interactions will act to increase the rate of Auger processes and so MEG in QDs.

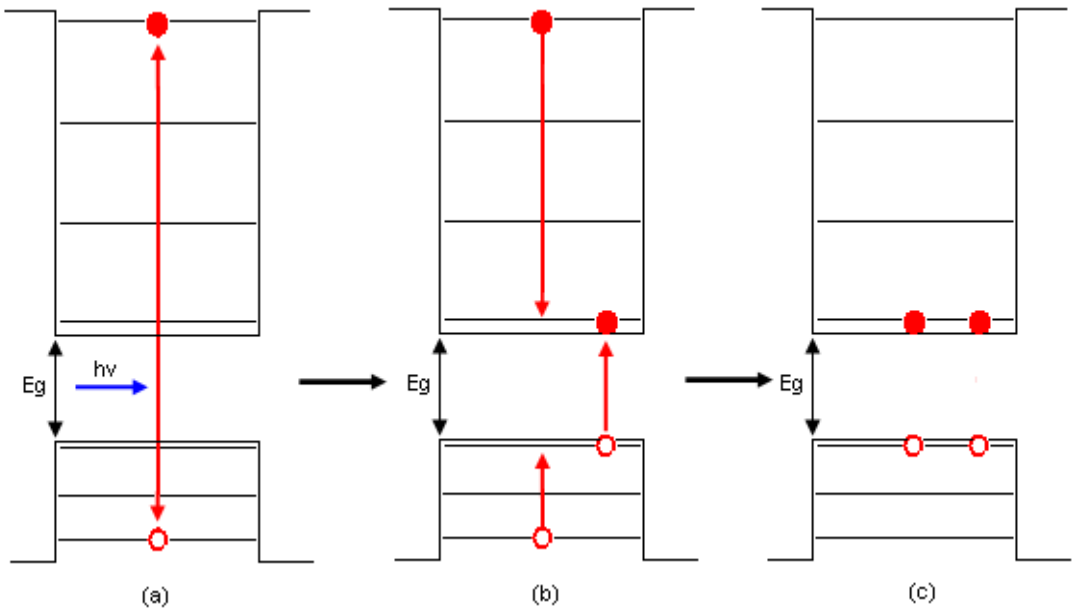

Figure 1.18 Schematic of MEG showing (a) excitation by energetic photons, (b) carrier multiplication and (c) relaxation.

To determine if MEG occurs in QDs, an experiment to monitor the transient decay curves after photo-excitation is predominantly employed. The spectroscopic techniques of transient absorption (TA) and fluorescence lifetime measurements by time correlated single photon counting (TCSPC) are well suited to making this kind of measurement. In these two experiments it is not MEG that is observed directly, as this happens on a femtosecond time scale, but rather the signature of MEG which is the emergence of a fast time component characteristic of Auger recombination. This can only be attributed to MEG, however, when excited by photons with energy above the threshold for MEG ($>2\ E_g$) and when the fluorescence is low enough such that the nanocrystals in the excited population absorb no more than one photon.[63]

1.12.5.1 Time-Correlated Single Photon Counting (TCSPC)

The time-correlated single photon counting (TSCPC) technique is used to obtain characteristic fluorescence lifetime measurements and gives superior sensitivity and dynamic range than any other method. The use of picosecond and femtosecond lasers alongside fast multichannel plate detectors (MCP) and constant fraction amplifiers and discriminators (CFDs) allows the measurement of lifetimes down to a few picoseconds. It is

a digital counting technique that detects single photons which are time correlated to a reference signal, usually the excitation light pulse. The sample is excited by a rapidly pulsing light source and uses the time taken from the excitation pulse to the observation of the first fluorescence photon to create a probability histogram. TCSPC is a statistical method and so a high repetition rate (> kHz) light source is required to quickly obtain a sufficient number of time measurements for high statistical precision. TCSPC has many benefits which has made it attractive to researchers as the method of choice for lifetime measurements. The technique allows time resolved measurements at the quantum limit, and measurements and observations in real time. The temporal resolution is determined by the transit time spread of the detector rather than the overall detector pulse response width. As a digital technique, TCSPC is not subject to the Gaussian noise associated with analogue techniques. The counting or Poisson noise is the only significant data noise and is well defined as the standard deviation of the square root of each data point. This has significant benefits for data reconvolution and fit evaluation.[64]

The method is dependent upon the measurement of the time between the excitation pulse and the detection of the single photon, see Figure 1.19. The electronics involved act as a very fast timing mechanism which is initiated by the start signal pulse from the excitation pulse and stopped by the detection of a single photon due to fluorescence. Each time measured between the start and stop signals is plotted in a histogram, where the channels represent time. This graph of histogram counts against time channels represents the fluorescence intensity versus time.

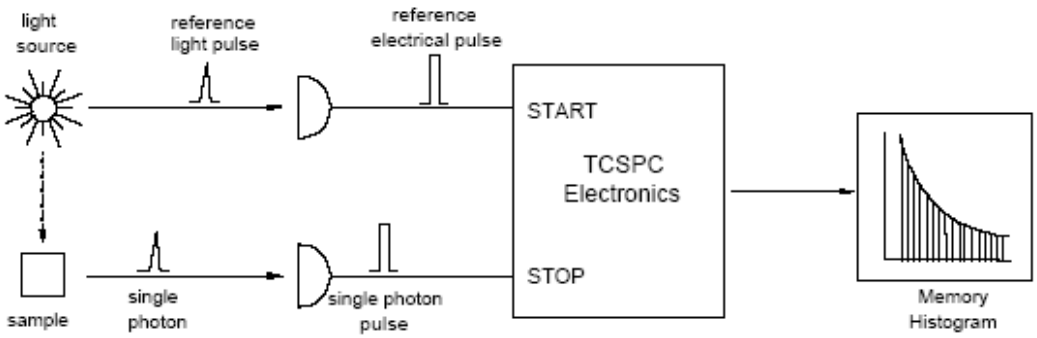

Figure 1.19 Schematic of TCSPC technique.[65]

1.12.5.2 Transient Absorption (TA)

Femotosecond transient absorption is a second type of spectroscopic technique which is a powerful and more widely used technique for measuring MEG with some benefits over TCSPC. Although TCSPC is exceptionally sensitive to weak light sources, the temporal resolution in TA is only limited by the width of the exciting laser pulse, and with modern ultra-fast laser systems offering sub 100 fs pulses the time resolution obtainable is unrivalled. By incorporating lock-in amplifiers and gated box car integrators it is possible to detect very small signals as well as tiny modulations in these signals. This experiment is a type of pump-probe spectroscopy whereby changes in absorption are monitored by a probe pulse following excitation by a pump source. The set up is shown in Figure 1.20. As the band edge of the dots is monitored the amplitude of the absorption change is proportional to the number of electron-hole pairs that are created in the dots.[66]

Figure 1.20 Transient absorbtion set up, blue beam drawn represents initial excitation beam and red beam drawn represents probe pulse.[67]

1.12.6 Multiphoton Excitation

This process was predicted by Maria Göppert-Mayer in 1931.[68] Up to this point only one-photon excitation processes have been focused on. Two-photon and three-photon excitation photoinduced processes can be seen in Figure 1.21 .

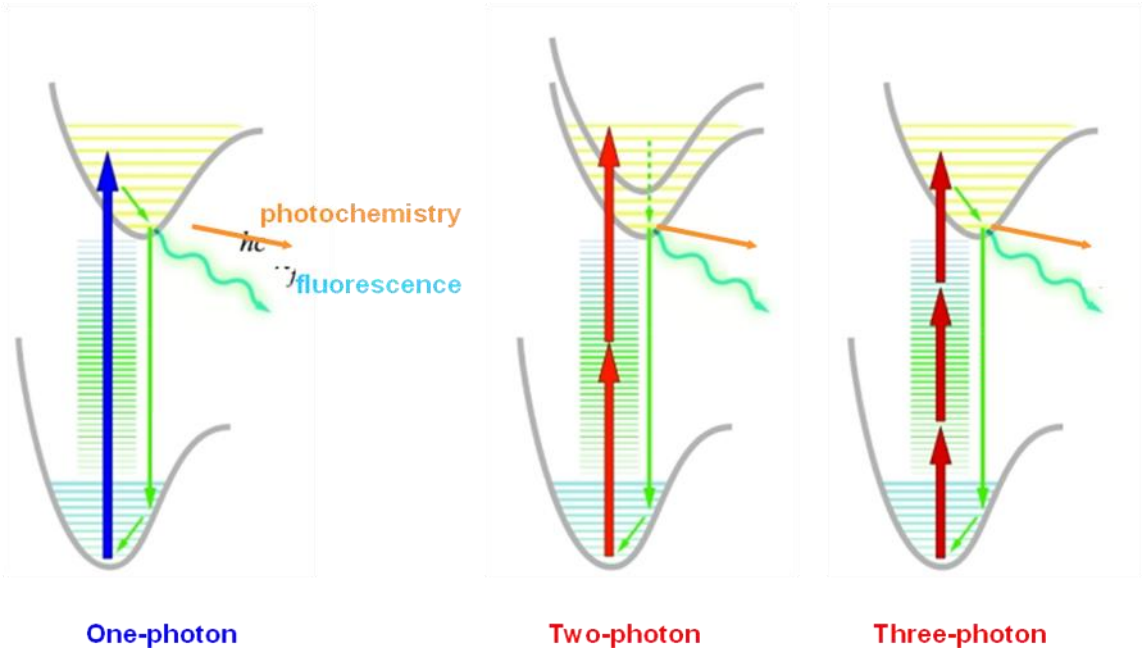

Figure 1.21 Photoinduced one-photon, two photon and three-photon processes processes which are possible using an intense coherent light source.[69]

These processes are possible using an intense coherent light source such as an ultrafast pulsed Ti:sapphire laser with 100 fs pulses at 80 MHz repetition rate, low energy (10 nJ) but with high peak power (0.1 MW). The wavelength is tuneable between 700 and 1000 nm. A diagram comparing the process of single excitation versus two-photon excitation can be seen in Figure 1.22.

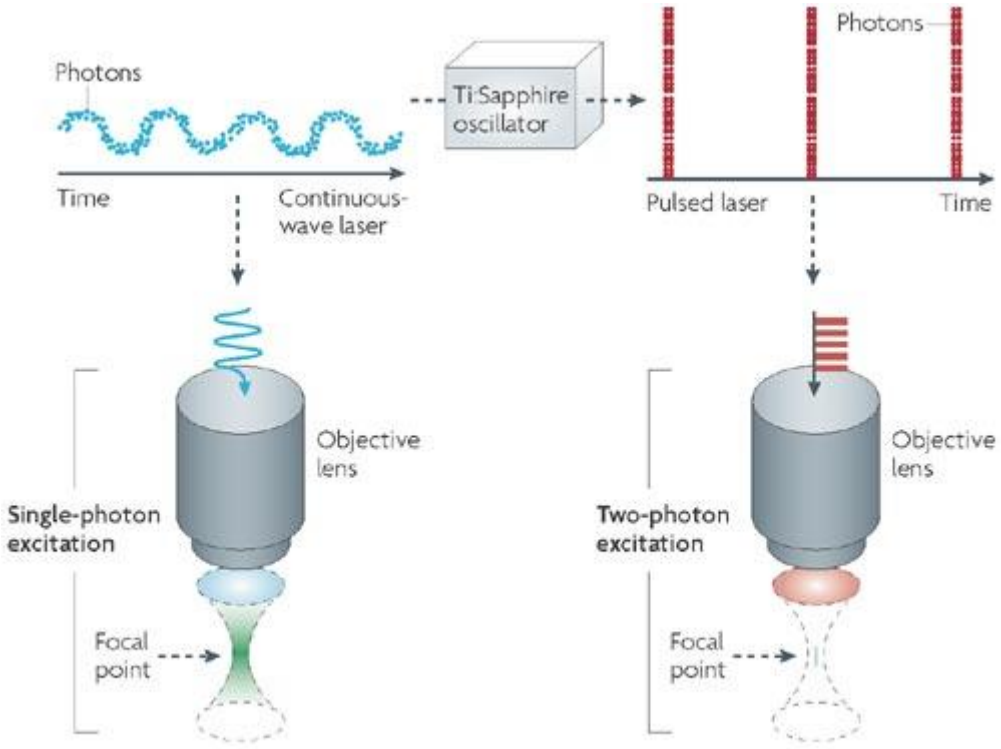

Figure 1.22 A comparison of single-photon excitation vs. two-photon excitation showing that the focal point is much more intense due to self-confocality for the two-photon process.[70]

It can be seen that the focal point is much more intense due to self-confocality for the two-photon process and this allows for 3D localisation of photoactivation with deep penetration into optically dense media (less scattering and absorption); they are also good at discriminating against scattered light. Another advantage of this process is the reduction of damage and photobleaching of QDs. The disadvantages are the high cost of the laser and that strong water absorption with wavelengths above 1000 nm causing thermal damage.

1.13 Characterisation of Nanoparticles

The characterisation of the materials synthesised is incredibly important. One of the reasons that research in this area has only become so popular towards the end of the 20th Century is because equipment to view the particles is a recent invention. In 1857, Faraday was unable to prove with images that he had successfully made colloidal gold nanoparticles. Only after the development of transmission and scanning electron

microscopy has this now become possible. These are among methods which allow us to structurally analyse the material on the micro- and nano-scale and transmission electron microscopy is discussed in the following section. In addition, powder X-ray diffraction, as this is another common method for structural analysis, will also be discussed in more detail.

1.13.1 Transmission electron microscopy

This technology is extremely useful as it provides a visual image of the nanomaterials being studied. The size, morphology and homogeneity of the sample can all be confirmed.

The transmission electron microscope (TEM) works in a similar way to conventional light microscopes however due to the small de Broglie wavelength of electrons the resolution of the modern TEM can approach the order of 0.1 nm. The wavelength of electrons is a lot smaller than those of light therefore limiting optical microscopes in the order of 100 nm.[71]

Information on the crystal structure of the nanomaterials can also be determined using TEM by using selected-area diffraction (SAD). SAD patterns can also determine Bravais lattices. The high magnification allows us to see lattice spacing, which when compared to crystallographic data for the sample can determine the plane of growth.

The TEM works by passing a stream of high energy electrons, with energies ranging from 100-400 eV, through a thin sample. High energy electrons are essential as this keeps scattering to a minimum. A high vacuum, *ca.* 10^{-6} mmHg, is also essential as electrons can easily be scattered in air. The electrons are focused using electromagnetic lenses which also correct astigmatisms and the magnification can be adjusted by changing the lenses' current. The electron beam passes through the sample and depending on the density some of the electrons are scattered and lost from the beam. The image, a collection of all the unscattered electrons, is viewed on a phosphor screen or special photographic film. The image appears as a shadowy image and the denser the material the darker the image. A cross section of the TEM is shown in Figure 1.23.

The most important methods in the TEM are bright field and dark field imaging, electron diffractions, electron energy loss spectroscopy (EELS) and energy dispersive X-ray

spectrometers (EDX). EELS and EDX are used to determine the elemental composition of a sample. Using EELS with high resolution transmission electron microscope (HRTEM) or super transmission electron microscope (STEM) imaging can be extremely useful when looking at core-shell nanoparticles as it can provide the elemental composition of a single particle as opposed to EDX which analyses the sample as a whole.[72]

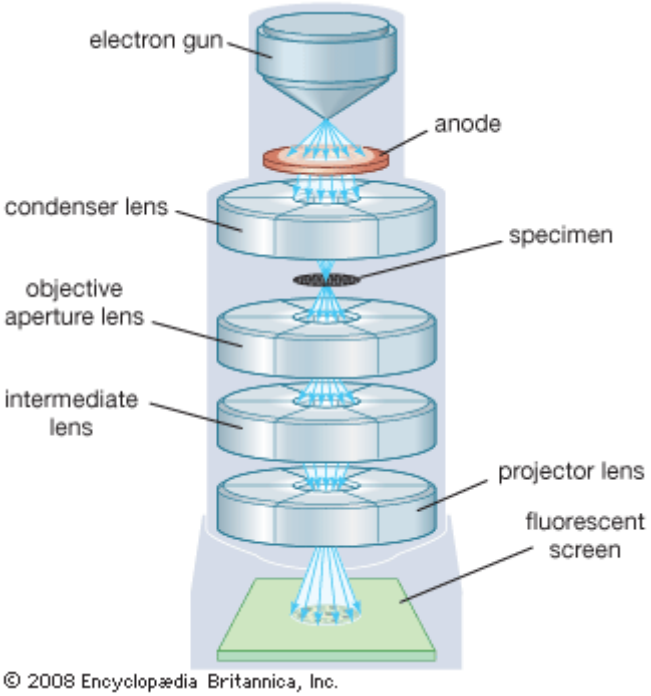

Figure 1.23 Schematic of a standard TEM.[73]

1.13.2 Powder X-ray diffraction (pXRD)

pXRD is a method to characterize the crystallographic structures by analysing their diffraction pattern. This is possible because each crystalline solid has its own unique characteristic X-ray powder diffraction pattern which can be used as a 'fingerprint' to identify it.[74]

Monochromicatic X-rays, with a wavelength λ, are projected onto a sample, at an angle of θ, and this causes secondary diffracted beams of X-rays in the form of cones. X-rays which are reflected from the surface travel a shorter distance than those which penetrate into the internal layers of the sample. The distance travelled by the X-ray depends on the angle at which the X-ray entered and the separation of the layers. For this wave to be in the same phase as the wavelength which was reflected from the surface it

needs to have travelled a whole number (*n*) of wavelengths whilst inside the material thus leading to constructive interference. This means the greater the number of wavelengths in phase the greater the intensity. If the distance is not an integral number then deconstructive interference occurs and the reflected wavelength is not detected. Bragg expressed this in an equation now known as Bragg's Law (Equation 1.7).[75]

$$n\lambda = 2d\sin\theta \qquad \textbf{Equation 1.7}$$

Where d is the lattice spacing between the planes.

The intensity of the wavelengths detected are plotted against the angles at which the X-rays hit the sample to give a graph of the diffracted peaks and this can be compared to databases containing patterns which are characteristic of many different crystalline materials. A schematic diagram of the apparatus is seen in Figure 1.24.

Using pXRD it is also possible to determine the size of the particles being measured and this is done using Scherrer's equation (Equation 1.8).[76]

$$d = K\lambda / \beta\cos\theta \qquad \textbf{Equation 1.8}$$

Where d is the average dimension of the crystallite, K is the Scherrer constant (this generally falls between 0.87 – 1, and is usually assumed to be 1), β is the full width of height maximum of the peak, λ is the wavelength of X-ray and θ is the angle of diffraction.

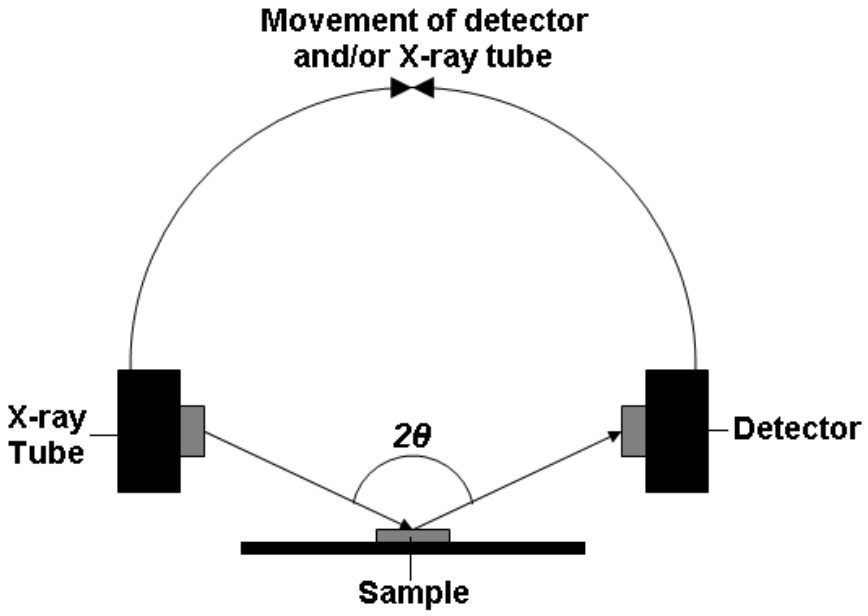

Figure 1.24 Schematic of p-XRD apparatus.[77]

1.13.3 Inductively coupled plasma atomic emission spectroscopy (ICP-AES)

This is an analytical technique used for detecting trace metals. It is a type of emission that uses the inductively coupled plasma to produce excited atoms and ions that emit electromagnetic radiation at wavelengths characteristic of a particular element.

To run a sample, the machine is first calibrated with a blank and standards with concentrations of 0.01 ppm, 0.05 ppm, 0.1 ppm and 0.5 ppm. The blank and standards are then run as samples to ensure the accuracy of the results. Ten samples are run and then the actual sample is measured before the blank and standards are run again to again check that the machine has not deviated and the results measured are accurate. The emission wavelength is noted for the elements being measured, which for the purpose of this thesis were cadmium, zinc, sulfur and selenium. The reported concentrations are measured in parts per million (ppm) and they are the data that are extracted. The standard deviation is also provided and informs as to how accurate the results are. As the blank and standards are run before and after the sample, the reproducibility can be determined by looking at the difference between the concentrations measured before and after. Also a rough approximation of the detection limit can be taken as three times the standard deviation of the blank.

1.14 Applications

Nature has always been ahead of us and capable of many things; and one of these is working on the nanoscale. Many functions in living things, which keep them alive, work on the nanoscale, including actin and myosin that drive the contractions of muscles.[78] Now that the benefits of nanomaterials are being realised there are many applications which take advantage of them. There is massive potential in this field as nanotechnology transcends the conventional boundaries of biology, chemistry, physics, information technology, engineering and mathematics.[79] This means that it has the possibility of having a large impact on our everyday lives and Figure 1.25 shows a cartoon illustrating some of the potential ways nanotechnology could do this. Some existing and potential applications of nanomaterials, which cover a range of different fields, will be discussed in the following sections.

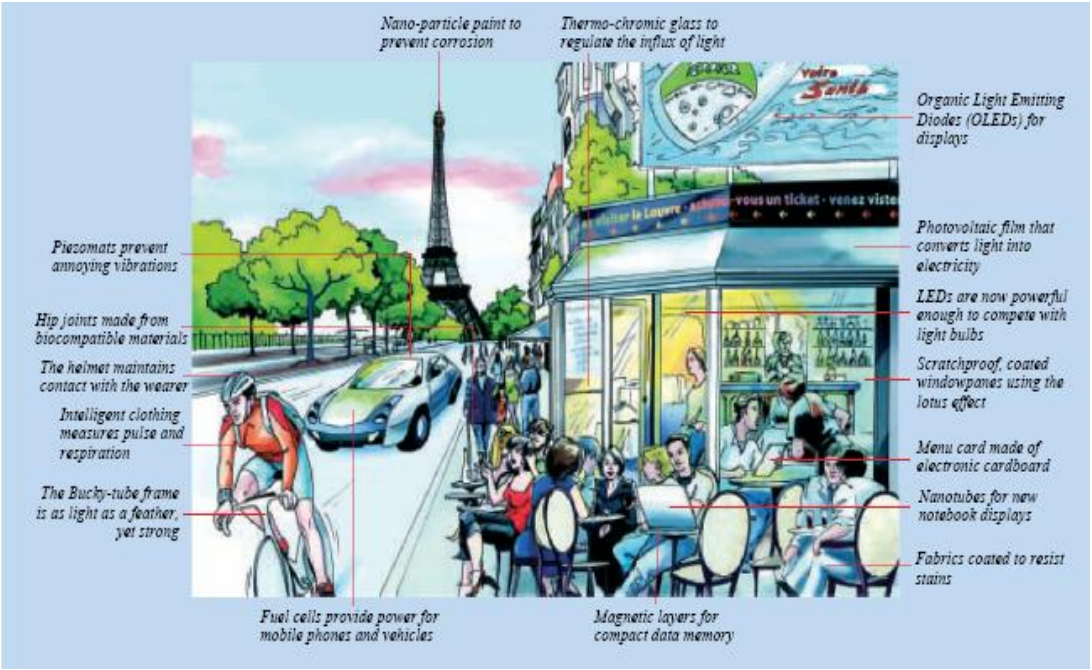

Figure 1.25 Nanotechnology possibilities for everyday life in tomorrow's world.[79]

1.14.1 Biological Applications

QDs, as discussed earlier in this chapter, have tuneable band gaps and this proves to be useful in biological applications. Currently, many of them rely on using organic dyes with limited wavelengths which are sometimes in a region of the spectrum which proves inconvenient as most absorb in the same regions as biological materials with water being a major interferant. This is why two-photon excitation technology has found many applications in biology, using IR radiation instead of UV to excite conventional dyes however, that causes the excitation of multiple organic dyes to be difficult and expensive. QDs tend to be brighter than dyes because of the compounded effects of extinction coefficients that are an order of magnitude larger than those of most dyes with comparable QYs and similar emission saturation levels. The main advantage of QDs over dyes is their resistance to bleaching over long periods of time. Dyes tend to have short lifetimes meaning that it is difficult to get sharp and well contrasted images. The increased photostability of QDs is very useful for three-dimensional optical sectioning. The new generation of QDs have far reaching potential for the study of intracellular processes at the single-molecule level, high-resolution cellular imaging, long-term *in vivo* observation of cell trafficking, tumour targeting and diagnostics.[80] Other applications of QDs being explored in the biological field can be seen in Figure 1.26.

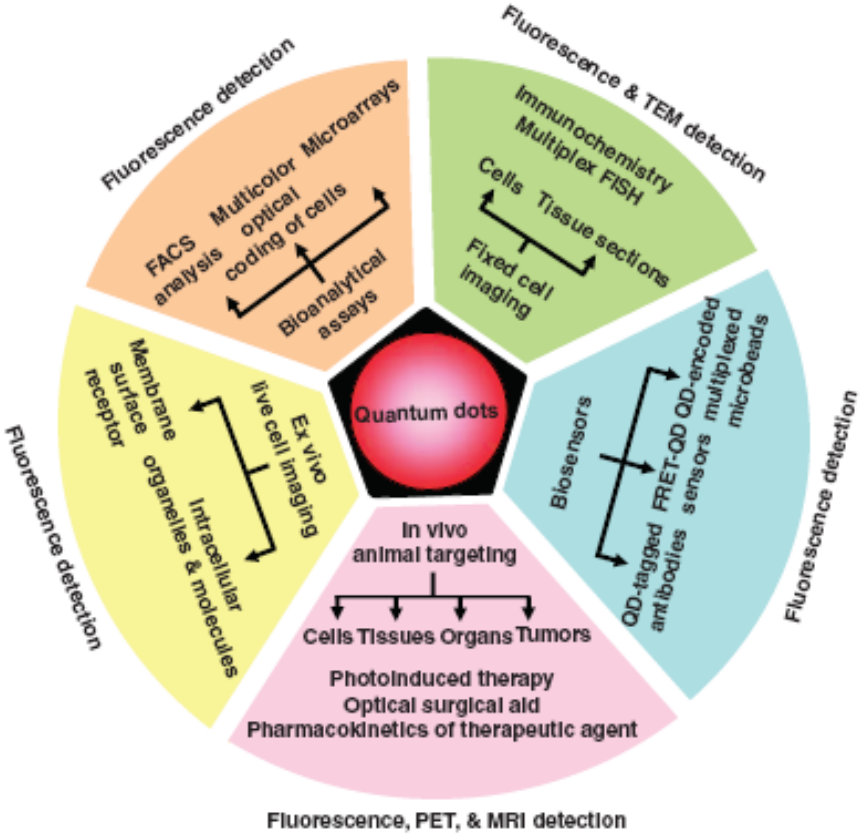

Figure 1.26 Applications of QDs as multimodal contrast agents in bioimaging.[80]

Some of the most successful uses of QDs have been the immunofluorescence labelling of fixed cells and tissues and fluorescence immunocytochemical probes. QDs are photostable, have high QYs, narrow emission spectra and an apparent large Stoke's shift meaning that they have several advantage over organic fluorophores in immunocytochemical studies of erythrocytes, for example.[81] The probes are generally used to detect antigens in tissue (Figure 1.27). QDs dramatically speed up the process of detecting antigens, from two to six days using the conventional method, to a few hours.

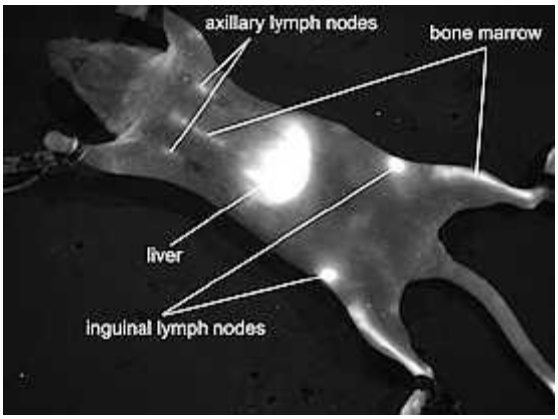

Figure 1.27 Immunocytochemical probes are used in the dead rodent. The probes in the body have circulated and now show up under fluorescent light, creating a much safer alternative to the x-ray.[81]

Future work in this area includes the introduction of QDs in beads which are being inserted into the body to target infected cells. Near-infrared (NIR) quantum dots are showing promise in the biomedical imaging of living tissue because nanocrystals emitting in this region (700-1000 nm) possess well known optical transparency in biological tissues.[82]

Technology is being developed that may exploit libraries of interfering RNA (RNAi), proteins and peptides with high-throughput (HT) performance evaluation of these libraries in a cell-based environment. This technology may deliver a platform for HT manipulation of embryonic stem (ES) cells through encoded bead-based delivery of RNAi and protein libraries ('beadfection'). Subsequent *in vivo* HT phenotypic analysis at the single cell level, coupled with QD encoding may provide a molecular framework for the control of ES cell self renewal and differentiation. Specifically, this work may provide a completely novel bead-based methodology for the delivery of biological macromolecules which may enable:

- Highly efficient delivery of RNAi and proteins to embryonic stem cells.
- Simultaneous, real time *in vivo* analysis of up to 100 independent 'beadfections'.
- Efficient RNAi mediated multiple transcript knockdowns which could allow up to 1,000,000 different gene knock-down profiles to be assayed.
- Controlled dosage of regulatory proteins in ES cells for analysis of differentiation fate choice.
- HT discovery of novel ligands for organelle targeting.

- Generation and delivery of bespoke randomized protein libraries to map the synergistic molecular motifs controlling ES cell pluripotency.

1.14.2 Cosmetic Applications

Cosmetic applications of nanoparticles are widespread and aid in the creation of superior cosmetic products. The nanoparticles can be evenly dispersed into a wide range of cosmetics which include moisturisers, colour foundations and lipsticks. These all provide high UV protection without the use of other chemicals and can even be transparent to visible light when desired, for example in sunscreens. They all tend to include titania (TiO_2) dispersions and FE45b (brown iron oxide). Titania, due to its wide band gap is able to absorb UV light and exhibits photo-catalytic properties upon radiation by UV which kills microbes upon contact. Therefore, as well as being commonly used in sunscreens, textile manufacturers are targeting the market with items of clothing, such as T-shirts, with disinfecting properties. It is the titania nanoparticles which kill germs by absorbing UV radiation from sunlight. As well as disinfecting properties, another interesting property of titania nanoparticles is that they provide a 'self-cleaning' coating. Known as the 'lotus effect'[83] water does not stick to its surface, like the lotus leaf or insects with large wings, as the nanoscale roughness combined with a hydrophobic substance increases its ability to repel water. This effect has been used to create a range of products including facade coating due to the self-cleaning efficiency of artificial superhydrophobic surfaces.[84] NASA is also researching this technology to be used as a lunar dust mitigation tool.[85] There are also some ointments and sunscreens which contain nano-sized zinc oxide powder.[86]

1.14.3 Microelectronic Technology

Over the past decade technology has been getting smaller and much more powerful. Moore's Law is used to describe a long term trend in the history of computing hardware and states that the density of devices on a chip doubles every 18 months, due to the of size of the transistor (Figure 1.28).

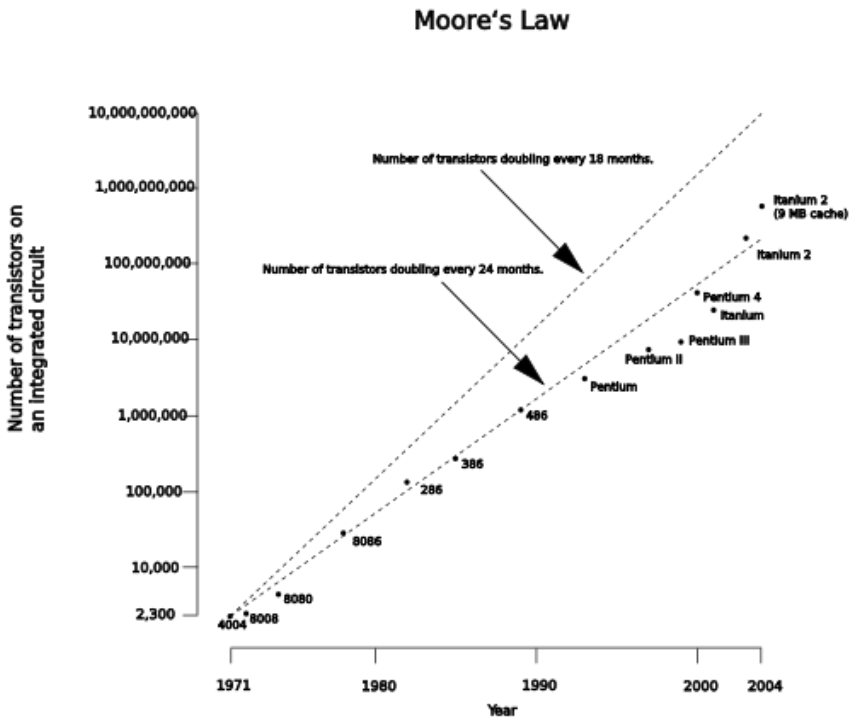

Figure 1.28 Logarithmic vertical scale of Moore's Law.[87]

Microelectronics are getting smaller and smaller resulting in new emerging fields such as nano-fabricated catalysts and nano-electromechanical systems where device performance relies on metal-oxide junctions often only a few atomic layers thick, are some of the many applications relying on the need to learn how to make things atom by atom, i.e. nanotechnology. Nanotechnology is the next logical step in producing high performing technological advances whilst reducing the device dimension in order to keep up with Moore's Law. Using QDs for information storage is also advantageous due to there being no need for electrons to flow to transmit a signal, electrical current does not need to be produced so heat problems are avoided.

The future of microelectronics is exciting. Once it is possible to have greater control on dot ordering and positioning it may be possible to address and store information optically on a single QD, therefore opening up the opportunity of ultra-high density memory devices.

1.14.4 Counterfeiting

Counterfeiting can affect every market, causing a massive economic loss due to illegal activities that aim to cheat large amounts of money from corporations and governments all across the world. In the field of counterfeiting pharmaceuticals, customers' health and finances may be adversely affected. This is because as well as the loss of revenue for the companies they are then at risk of large law suits which in turn leads to higher insurance rates and effectively a higher price for the drugs required by the customer. Anti-counterfeiting technology has to be continually upgraded and developed to stay ahead of criminals. Legitimate products are currently tagged with fluorescent inks, dyes, watermarks or codes which mark the item as unique. Authentication of products is split into three categories:

1. Overt security – features which are apparent and visible to everyone and require no special instruments to detect them, e. g. Watermarks, holographic foil.

2. Covert security – features which are hidden but with the aid of a simple instrument, e. g. UV lamp, magnifier, they can be identified, e. g. QDs, holograms containing microtext.

3. Forensic level security – features which are very secret and present on a 'need to know' basis only, e. g. IR analysis, memobeads, addition of low concentrations (ppm) of a taggant.

Quantum dots can be used for covert and forensic level security as they are beginning to be used to produce unique 'bar-codes' that will be very difficult to re-create by people trying to produce counterfeit copies. This is due to their narrow and tuneable emission peak which can range from the infrared to UV. An almost infinite variety of different spectral codes can be created by changing the concentration, the number of quantum dots used and the emission peak of the QDs. They could be used as security tags for documents, such as passports, credit card, or banknotes and they can also be used in pharmaceuticals. Work is looking into the incorporation of memobeads for in-tablet labelling which would act as a form of forensic level security as it can only be visualised by confocal microscopy when viewing the central plane leaving the label invisible otherwise. Incorporation of taggants in drug formulations is not at all in use currently as the FDA still requires extensive toxicological screening of the taggant.[88]

1.14.5 Solar Cells

QDs have the potential to increase the capabilities of solar cells that are currently in use today. It is well known that current energy sources are beginning to run out and alternatives need to be found. Photovoltaic (PV) solar cells are one of the sources aiming to convert light energy to electrical. Current research is trying to increase the efficiency of this conversion, which currently needs a large surface area and only a small percentage of light captured is converted. Silicon is the main material used in commercial solar cells, but research using different nanomaterials is currently been carried out. Leading contenders are cadmium-indium-gallium-selenide (CIGS)/ cadmium-indium-selenide (CIS), TiO_2, cadmium telluride/cadmium sulfide, gallium-arsenide and lead sulfide or selenide. Efficiencies over 25% have been achieved with gallium arsenide and this is one of the highest possible currently, although 30% has been measured for gallium-indium phosphide/gallium arsenide.[89] Thermodynamics show that 93% is the limit of conversion of sunlight to electricity as opposed to the upper limit of 33% for a single junction solar cell. Double and triple junction cells based on GaInP/GaAs/Ge have been developed on space craft with terrestrial conversion rates reaching nearly 30%, which increases under concentrated sunlight.[90] Quadruple junction cells are now approaching 40% efficiencies and are currently under development.[91]

1.14.6 Other

"Inverse" QDQW structures, CdSe/ZnS/CdSe, as described previously are unique heterostructures. As stated CdSe is a tuneable semiconductor as the wavelength it emits is dependent on size, therefore, this system emits at two different wavelengths coming from the CdSe core and CdSe shell. This phenomenon is being used for the generation of white light.[92] The ZnS shell must be at least 3 monolayers to ensure there is electronic decoupling of the CdSe core and outer shell.[93]

Other applications of nanomaterials include light emitting diodes (LEDs) and fluorescent paints. QD use in LEDs (QLEDs) is to combat the shortfalls of LEDs which include the non-tunability of their light emission. Due to the tunability of QDs and their photostability, they are the obvious choice for the future of LEDs as they can potentially help cut costs and save fuel in the production of white light.

Fluorescent paints work by incorporating QDs which can then be used for a variety of applications. A major example is the incorporation of infrared QDs into paint which is then used on military uniforms, helmets or other military gear. With the use of night vision goggles and intimate knowledge of the exact make up in question it would appear as either unrecognisable noise or invisible to hostile forces. As QDs can emit at desired wavelengths, the art of identifying and copying the correct wavelength signature to fool enemy forces would be almost impossible.

QDs can also be used as anti-trespass tags in the form of Evidust.© QDs can be placed into tiny beads of Evidust,© which is just like normal dust but with the ability of emitting in the IR region and adhering to passersby. This dust can be placed on any terrain and used as a tracking device, as without intimate knowledge of the signature being used, it is almost impossible to identify, detect and mimic by hostile forces, therefore making it a useful tool for intelligence agencies.

1.15 Conclusion

Nanomaterials have gained a lot of attention from the world's press and research scientists alike due to the large possibilities these small molecules could potentially achieve. By reducing bulk materials to a size smaller than the bulk-exciton Bohr radius, which varies for different materials, they exhibit different properties which can be advantageous for multiple applications. This is part of the reason why advances in this field have continued at a rapid pace. Other reasons include the ability to view nanomaterials with TEM and SEM, increase quantum yields, improved monodispersity, specific morphologies and electronic properties and efficiency. Improved quality of samples have aided the establishment of correlation between experimentally observed phenomena and predictions based on theory. This has enabled the physics of nano-dimensional materials to be understood to a better degree.

The work reported in this thesis is to synthesise QDs that can be used to deliver a technology platform for high-throughput (HT) manipulation of embryonic stem cells through encoded bead-based delivery of RNAi and protein libraries ("beadfection"). This will be in the form of advanced "tagged" polymer bead technology to possibly generate "molecular pills" that deliver discrete library molecules directly to embryonic stem cells

thus circumventing all the problems normally connected with current gene and protein delivery. To do this a large library of QDs emitting at different wavelengths over a large range needs to be generated. Different materials, Figure 1.29, and the use of different methods will be used to fulfil the criteria. The QDs synthesised must have high QYs as the action of putting them into beads immediately reduces the luminescence but they still must be highly visible so that fluorescent-activated cell sorter (FACS) measurements can be taken.

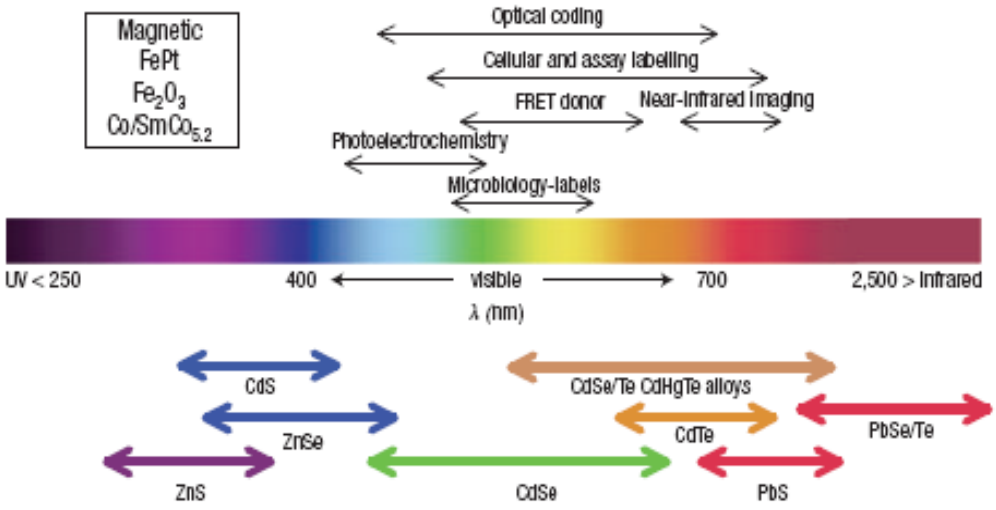

Figure 1.29 Representative QD core materials scaled as a function of their emission wavelength superimposed over the spectrum. Representative areas of biological interest are also presented corresponding to the pertinent emission highlighting how most biological usage falls in the visible–near infrared region. Inset representative materials used for creating magnetic QDs.[94]

CHAPTER 2 SYNTHESIS OF TYPE I LUMINESCENT NANOPARTICLES

2.1 Introduction

Cadmium selenide (CdSe) nanoparticles are the subject of intense research as the position of their light emission can range across the entire visible region simply by varying the mean diameter of the nanocrystals.[95] CdSe has a direct band gap of 1.74 eV at 300 K and 1.85 eV at 0 K. CdSe nanoparticles are of interest for applications that utilize their light emission and absorption properties including use in photovoltaic cells[95] and optical devices such as biomarkers[96] and light emitting diodes.[97]

Bulk CdSe exists in two different crystalline lattice structures and can be either wurtzite (W, hexagonal) shown in Figure 2.1 or zinc blende (ZB, cubic) dependent on the packing form it takes. The W structure has an ABABAB stacking sequence along the [001] direction, whereas the ZB structure has a stacking sequence of ABCABC along the [111] direction.

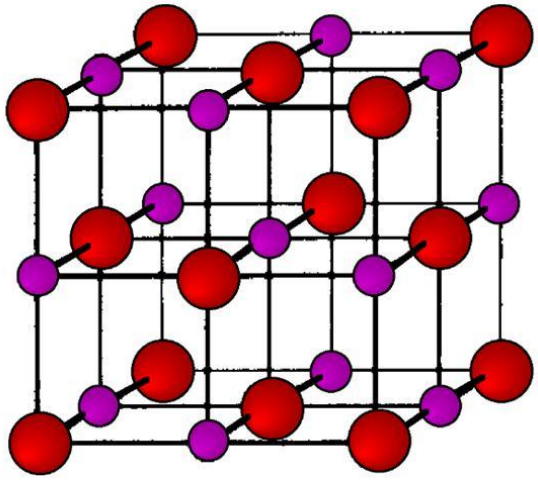

Figure 2.1 CdSe Hexagonal/Wurtzite unit cell.

Bawendi *et al.* in 1993 successfully synthesised highly luminescent CdSe nanoparticles using a high temperature organometallic process.[37] This method however is not potentially viable for scale up due to the nature of the organometallic precursors, such as dimethyl cadmium ($Cd(CH_3)_2$), which are pyrophoric, toxic and explosive. In addition, the process is not cost effective on a large scale.

A common method for synthesising CdSe nanoparticles involves the use of inorganic clusters as single-source precursors. These are compounds which have the basic unit of the semiconductor covalently bonded directly to each other within the precursor molecule, for example the cadmium is directed bonded to selenium within the complex. The nucleus of the semiconductor is preformed within the precursor so that the growth process is simplified. Steigerwald *et al.*, in 1989, first reported the synthesis of colloidal quantum dots using single-source precursors involving the reaction of two different precursors, $Cd(SePh)_2$ and $[Cd(SePh)_2]_2[Et_2PCH_2CH_2PEt_2]$. Both successfully decomposed to form CdSe quantum dots in refluxing pyridine.[98] Since then multiple methods for synthesising CdSe nanoparticles, as well as other types of nanoparticles, from single-source precursors have been developed. O'Brien *et al.* had originally set out to form precursors for chemical vapour deposition of thin films. However, using high boiling point coordinating solvents, such as HDA or TOPO, to thermolyse the precursors , dialkylcarbamates of the type $[M(E_2CHRR')_2]$ (where M = Cd/Zn/Pb/In/Cu/etc., E = S/Se, R or R' = Me/Et/Pr/^{i}Pr/^{n}Bu/^{n}Hex/etc.), the precursors are decomposed to form high quality, size controllable monodispersed nanoparticles.[34,99-100] The effects of the symmetrical and asymmetrical alkyl R and R' groups on decomposition were studied by MOCVD and they found that changing from a symmetrical diethyl to an asymmetrical methyl (*n*-hexyl) derivative hinders the formation of diethyl diselenide, thus inhibiting the deposition of selenium during film growth. This resulted in successful deposition of ZnSe or CdSe, depending on which precursor was used. It has been demonstrated by Cumberland *et al.* that molecular inorganic clusters, which are stable under ambient conditions, are convenient single-source precursors for the controlled formation of 2-9 nm CdSe nanocrystals.[101] The use of a cluster-based single-source precursor allows nanomaterial growth to be initiated at low temperatures, omitting the pyrolytic step for nucleus formation traditionally required for lyothermal growth processes. The elimination of the pyrolytic step means there is low toxicity, greater synthetic control is possible, that the stoichiometry of metal atom to chalcogenide atom is governed by the design of the organometallic complex, slow thermodynamic growth at low temperatures due to the high degree of association, and that high crystallinity and reaction scalability (> 50 g/L) can be achieved while maintaining size dispersity at ~5 %. Also due to it being a single-source precursor, homogenous pre-reaction is limited as there is only a single molecule in the supply stream when using MOCVD. Further study revealed that it is possible to control the

impurity incorporation into the films by ligand design and that the phase of the material grown can be controlled by the core structure of the precursor compound.

As selenium is prone to oxidation, CdSe nanoparticles are generally shelled to protect them from the oxygen in the atmosphere. The most popular shelling materials are zinc sulfide or selenide and have been used by many research groups. Although shelling with ZnSe results in a greater increase in PL intensity when compared with shelling with ZnS, the same problem persists; the selenium in the ZnSe will oxidise causing the PL intensity to decrease. On the other hand, when shelling with ZnS the PL intensity increases and the stability of the dots is improved due sulfur's greater resistance to oxidation. The reason why the PL and QY increase upon shelling is due to the passivation of the crystallite CdSe core, therefore removing surface traps.[102] The thickness of the shell plays an important role as the shell is unstable beyond a certain depth due to the lattice mismatch, therefore resulting in a low QY if the shell is too thick.[103] A thin shell however means that the lattice strain is less and provides only a small impediment to high energy electrons. The shelling methods often require the use of metal alkyls causing the reactions to be potentially dangerous due to the pyrophoric, toxic and explosive nature of the reagents. In addition, the reactions are expensive to carry out.[104]

The 'green' methods generally used to synthesise CdSe and CdSe/ZnS nanoparticles reported in this chapter are an area of great interest in this field of chemistry. By using alternative cadmium sources pyrophoric organometallic precursors can be avoided. Several methods are available for the synthesis of CdSe nanoparticles,[105-105] however it is only very recently that 'green' ZnS shelling techniques have been developed. The replacement of hazardous organometallic reagents with monomolecular precursors, such as zinc ethylxanthate and zinc stearate provides an excellent alternative.[42] These precursors are both air stable and zinc ethylxanthate is easy to prepare with a low decomposition temperature of 150 ^{o}C.

CdSe/ZnS core/shells have reproducible synthetic methodologies which result in high photoluminescence quantum yields (30-50 %).[107] In recent years, L. Qu and X Peng have reported QYs of up to 85 % which means that only a small amount of decay occurs via a nonradiative mechanism.[108] However, spectral drift and intermittency effects are still being observed in many CdSe/ZnS nanoparticles showing the effects of carrier escape onto

surface states.[109-111] More work is therefore required in this area in order to achieve even higher QYs.

2.2 Results and Discussion

2.2.1 Synthesis of CdSe nanoparticles

CdSe quantum dots (QDs) were grown by means of high temperature colloidal synthesis using cadmium oxide in a mixture of oleic acid and octadecylamine (ODE) and elemental selenium dissolved in trioctylphosphine (TOP). The diameter of the CdSe nanoparticles varied depending on the amount of selenium injected into the solution, in order to vary the emission wavelengths. Table 2.1 shows a selection of a range of selenium concentrations and annealing times used.

Sample ID	Amount of TOPSe (0.2M) solution (ml)	Time left to anneal (min)	Resulting emission wavelength (nm)
KP68a	3	0.33	No emission
KP68b	3	18	No emission
KP69a	6	1	539
KP69b	6	18	545
KP70a	8	0.33	578
KP55	8	18	588
KP70b	8	18	617

Table 2.1 Table showing sample ID, quantity of selenium solution injected, reaction time and resulting emission wavelength of a selection of the CdSe QDs synthesized excited at 480 nm.

The normalised luminescence spectra for this range of nanoparticles are shown in Figure 2.2 and show emission from 539 – 617 nm which were all excited at 480 nm. A range from 501-617 nm was achieved by varying the concentration of TOPSe used and the reaction time as these were the two major factors which affect the size of the resultant nanoparticles and effectively where they emit.

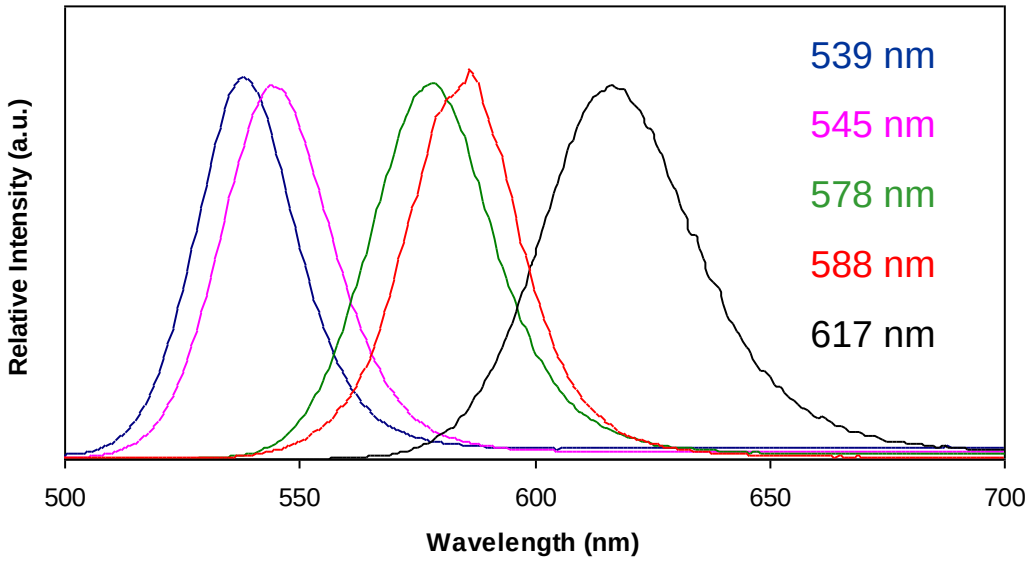

Figure 2.2 Normalised PL spectra of CdSe nanoparticles emitting at 539 nm, 545 nm, 578 nm, 588 nm and 617 nm which were excited at 480 nm.

It was initially believed that tetradecylphosphonic acid (TDPA) was only essential for structural purposes, however when omitted from the reaction it was detrimental to the overall luminescence of the nanoparticles. The concentration of selenium used had a large effect on the size and growth of the CdSe nanoparticles synthesised. This was confirmed when a low concentration of selenium was used and this resulted in no luminescence being observed. A red shift was observed as the concentration of selenium was increased and this is expected as it meant that the particles can grow larger. By increasing the concentration of selenium, but keeping the reaction time, the red shift observed was greater than 70 nm highlighting that this has a larger effect on the size of the nanoparticles when compared with changing the length of the reaction.

The size of the CdSe nanoparticles were determined by high resolution TEM and Figure 2.3 shows the sample which emitted at 545 nm and was 4 nm in size.

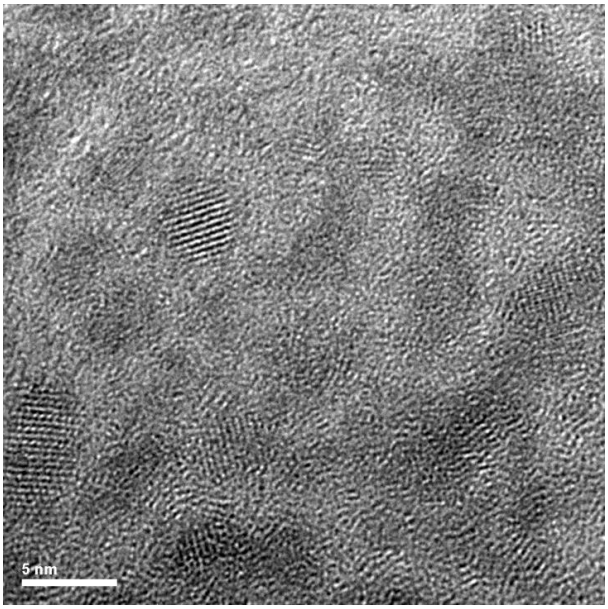

Figure 2.3 High resolution TEM image of CdSe nanoparticles emitting at 545 nm and 4 nm in size (scale bar = 5 nm).

The reaction time was still an important factor as the times used for this reaction were between 20 s and 18 min. To ensure that the reactions finished after the desired time, the flasks were cooled using a water bath or compressed air. As expected, with a short reaction time the particles synthesised were small and luminescent towards the blue region of the visible spectrum. By increasing the reaction time, but keeping all other variables constant, a red shift of ~6-10 nm was observed. This is expected because the particles are larger as more time has been allowed for them to grow.

2.2.2 Synthesis of zinc ethylxanthate

The synthesis of zinc ethylxanthate (see Figure 2.4a) is a simple procedure using air stable reagents in distilled water. Zinc chloride in distilled water was slowly added to potassium ethyl xanthogenate in distilled water at room temperature. Zinc ethylxanthate immediately formed as a white precipitiate which was then collected. The TGA (under N_2, 10 ^{o}C/min), Figure 2.4b, shows that this precursor decomposes at ~130 ^{o}C in a single step leaving ~38% residue which corresponds well with bulk ZnS (cal. 40%). This is therefore an

ideal precursor for ZnS for the intended reaction as the shelling occurs at 200 °C, which is higher than the decomposition temperature.

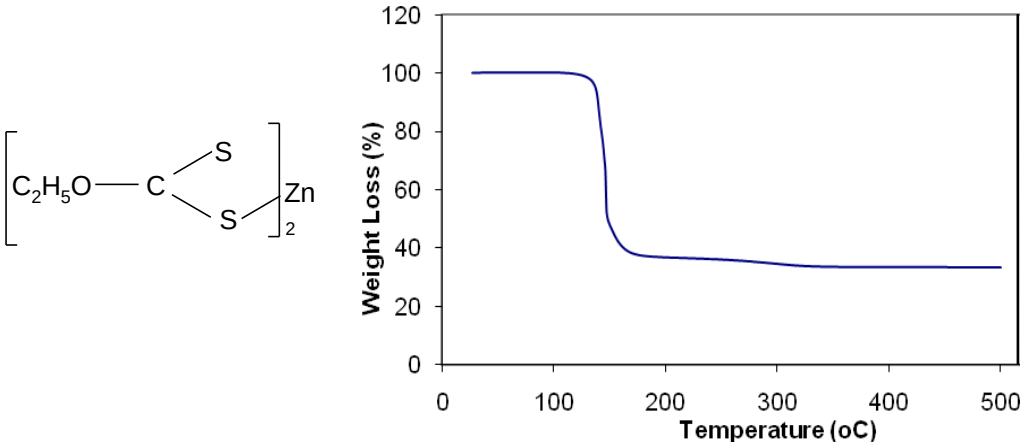

(a) (b)

Figure 2.4 (a) Structure of zinc ethylxanthate; (b) TGA plot (under N_2, 10 °C/min) of zinc ethylxanthate which decomposes at 130 °C in a single step leave ~38% corresponding well with bulk ZnS (cal. 40%).

2.2.3 Synthesis of CdSe/ZnS nanoparticles

The CdSe nanoparticles synthesised in 2.2.1 were then used as the cores for following set of shelling reactions. The CdSe nanoparticles were added to oleylamine and ODE. Two zinc solutions were prepared, zinc ethylxanthate dissolved in TOP and zinc stearate dissolved in TOP. These two solutions were combined and then were added slowly at a steady rate to the CdSe solution. Once all the zinc solution had been added, the solution was cooled and the particles were isolated. The emission range of cores used was 501-617 nm. Table 2.2 shows the emission and absorption data. It can be seen that the absorption value is generally 10 – 20 nm less than the emission value.

Sample ID CdSe	Emission (nm)	Sample ID CdSe/ZnS	Absorption (nm)	Emission (nm)
KP103	501	**KP108**	493	509
KP92	540	**KP93**	530	548
KP95	546	**KP97**	541	560
KP104	557	**KP111**	570	581
KP55	588	**KP63**	590	606

Table 2.2 Table showing sample ID of the CdSe cores used and CdSe/ZnS QDs synthesised and the resulting emission when excited at 480 nm and the absorption wavelengths.

The UV-vis spectra of these samples can be seen in Figure 2.5 with the absorption peaks ranging from 493 – 590 nm.

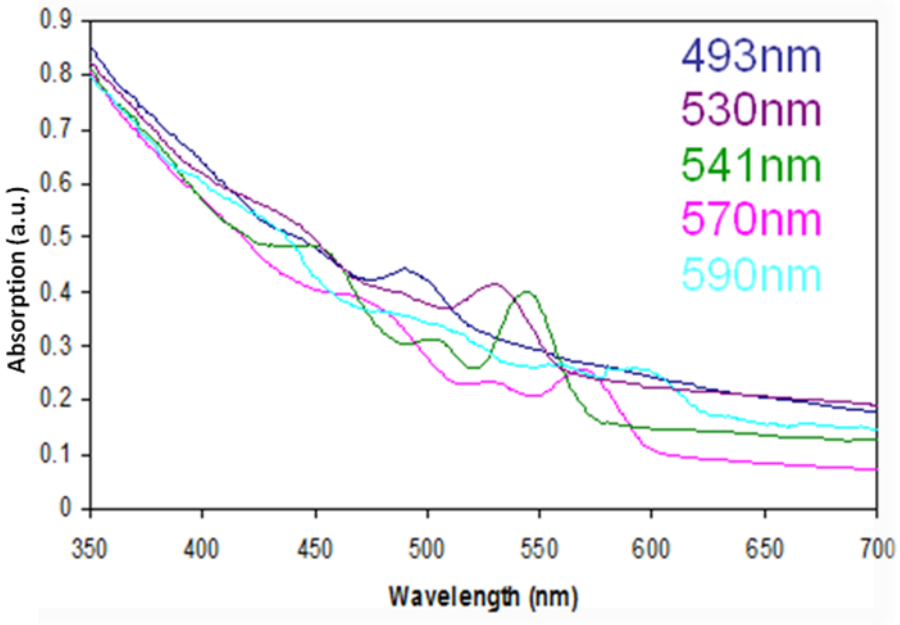

Figure 2.5 UV-vis absorption spectra of CdSe/ZnS absorping at 493 nm, 530 nm, 541 nm, 570 nm and 590 nm synthesised using a range of different sized CdSe cores (see Table 2.2).

Figure 2.6 shows the normalised PL spectra for a sample of the core/shell CdSe/ZnS nanoparticles synthesised which were excited at 480 nm. A range from 509 – 621 nm was achieved.

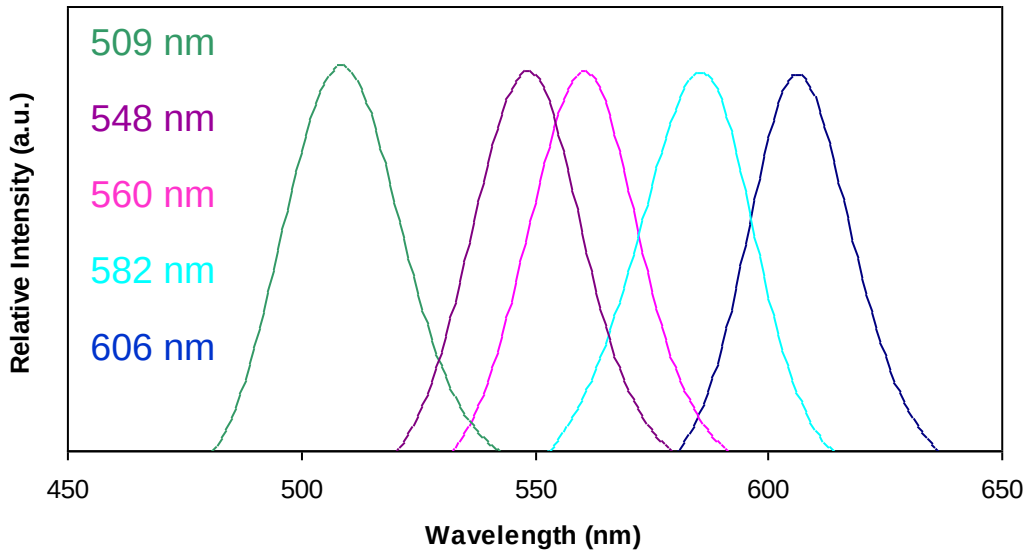

Figure 2.6 Normalised PL spectra of CdSe/ZnS emitting at 509 nm, 548 nm, 560 nm, 581 nm and 606 nm which were excited at 480 nm and synthesised using a range of different sized CdSe cores.

A photograph of these CdSe/ZnS nanoparticles luminescing under UV light can be seen in Figure 2.7.

Figure 2.7 A photograph of five different CdSe/ZnS samples emitting at (L-R) 509 nm, 548 nm, 560 nm, 582 nm and 606 nm under a UV lamp.

The QY of four of these samples were measured using the absorption and PL data. The blue sample emitting at 509 nm had a QY of 9.2%, the two green samples had a similar QY of ~ 15% and the red sample emitting at 606 nm had the highest QY which was 28.8%. The graph in Figure 2.8 shows the increase of QY as the particles increase in size in this case. This could be due to the surface of the QDs being more passivated therefore reducing suface defects so that electrons recombine radiatively.

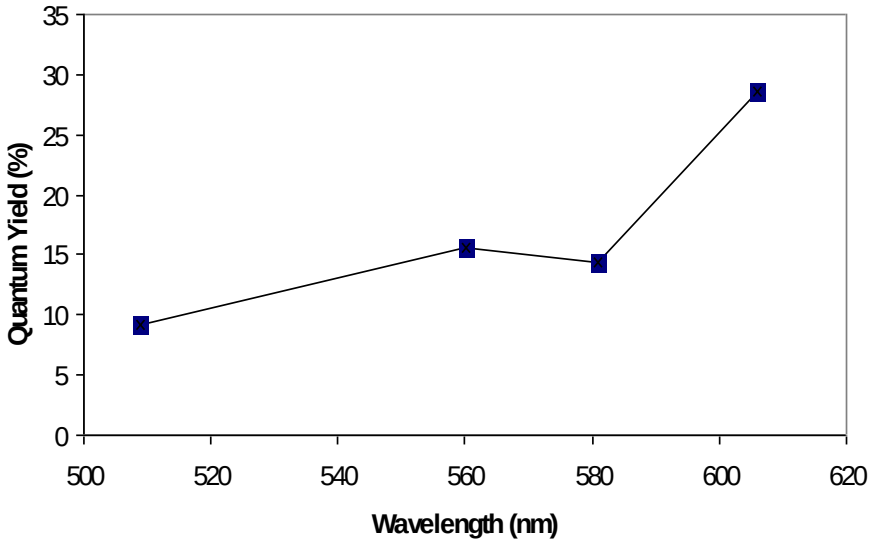

Figure 2.8 A graph showing an increase of QY as the wavelength increases for a few of the CdSe/ZnS samples synthesised.

The pXRD of CdSe/ZnS (KP97) is shown in Figure 2.9. For the CdSe core, the (100), (102) and (110) CdSe peaks can be found at 24.4 ^{o}, 36.1 ^{o} and 43.0 ^{o} respectively. (002) ZnS peak was found at 27.6 ^{o}. There is a range of peaks that could be either due to the CdSe core or the ZnS shell at 25.8 ^{o}, 46.8 ^{o} and 50.6 ^{o}.

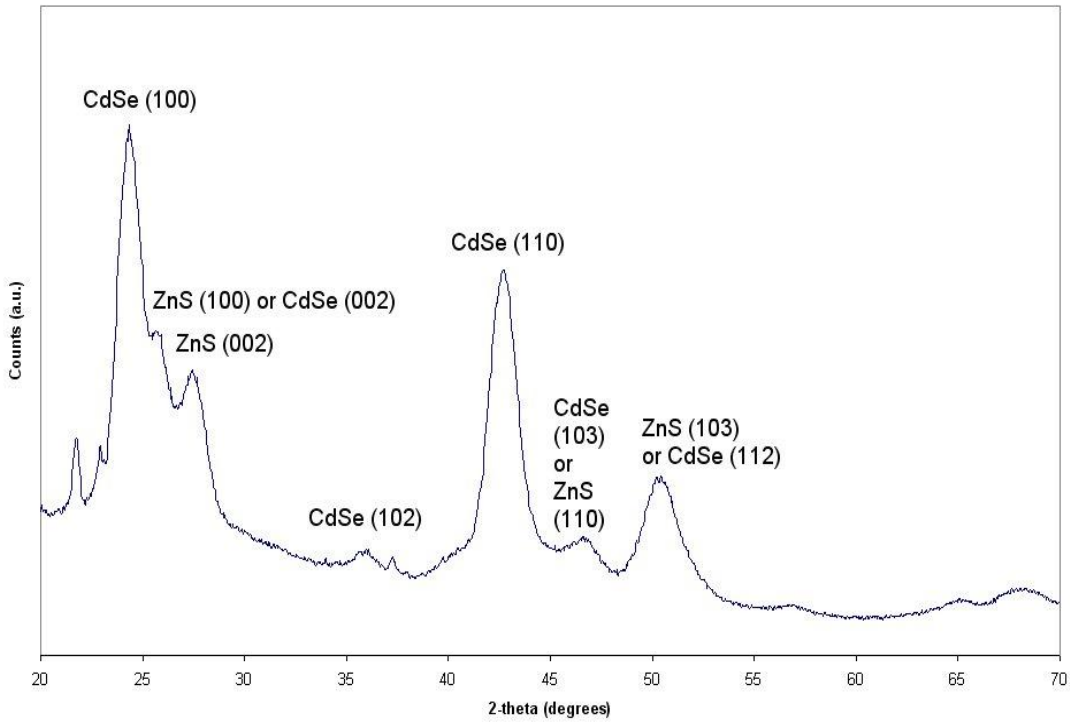

Figure 2.9 pXRD pattern of CdSe/ZnS (KP97) which emits at 560 nm is made up of 7 main peaks. The CdSe core, the (100), (102) and (110) CdSe peaks can be found at 24.4 °, 36.1 ° and 43.0 ° respectively. (002) ZnS peak was found at 27.6 °. There is a range of peaks that could be either due to the CdSe core or the ZnS shell at 25.8 °, 46.8 ° and 50.6 °.

Figure 2.10 shows the TEM image of CdSe/ZnS sample which emits at 560 nm. The size of the particles was measured to be approximately 4.2 nm and they were observed to be close to spherical in shape.

Figure 2.10 TEM image of the CdSe/ZnS sample (KP97) emitting at 560 nm and approx. 4.2 nm in size (scale bar = 100 nm).

2.2.4 Synthesis of red CdSe/ZnS HDA capped nanoparticles

During the previous set of experiments we were unable to tune the emission range beyond 617 nm. Therefore it was attempted to prepare larger CdSe nanoparticles by the following methods.

The first method involved the use of hexadecylamine (HDA) as the capping agent and the thermal decomposition of the cadmium cluster precursor $[HNEt_3]_4[Cd_{10}Se_4(SPh)_{16}]$.[112] The cluster was added to TOPSe and cadmium acetate in TOP, before being added to the degassed HDA:oleylamine mixture. The temperature was then increased with the slow addition of more TOPSe and cadmium acetate in TOP. The growth time for this reaction was 60 h; however we were unable to grow CdSe nanoparticles that emitted at wavelengths longer than 608 nm.

In an attempt to increase the size, the CdSe nanoparticles were shelled with ZnS using zinc ethylxanthate and zinc stearate. Figure 2.11 shows the PL spectra of CdSe and then the CdSe core shelled with ZnS. From this we can see that shelling with ZnS has no significant effect on the size of the nanoparticles as a slight blue shift is observed rather than an expected red shift; as they are emitting at 607 nm. This could be due to PL spectroscopy machine inaccuracy rather than an actual blue shift. The accuracy value of the machine is +/- 0.5 nm. Despite this it can be seen that the intensity of the peak emitted by CdSe/ZnS is greater than CdSe.

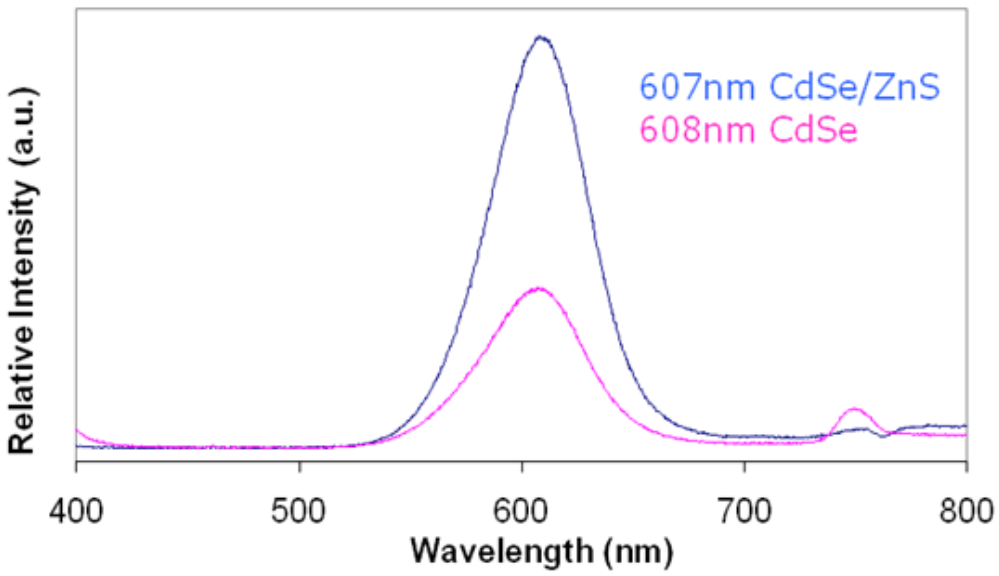

Figure 2.11 PL of CdSe core emitting at 608 nm and CdSe/ZnS emitting at 607 nm after being excited at 480 nm.

2.2.5 Synthesis of red CdSe/ZnS oleic acid capped nanoparticles

Another synthetic method was attempted in order to synthesise red emitting CdSe nanoparticles. This used cadmium oxide as the cadmium source in oleic acid and ODE. Separately, selenium was dissolved in TOP and oleylamine. The cadmium solution was then injected quickly into the selenium solution and the growth period was only 5 min. Figure 2.12 shows the PL spectrum of the CdSe nanoparticles grown which emit at 641 nm.

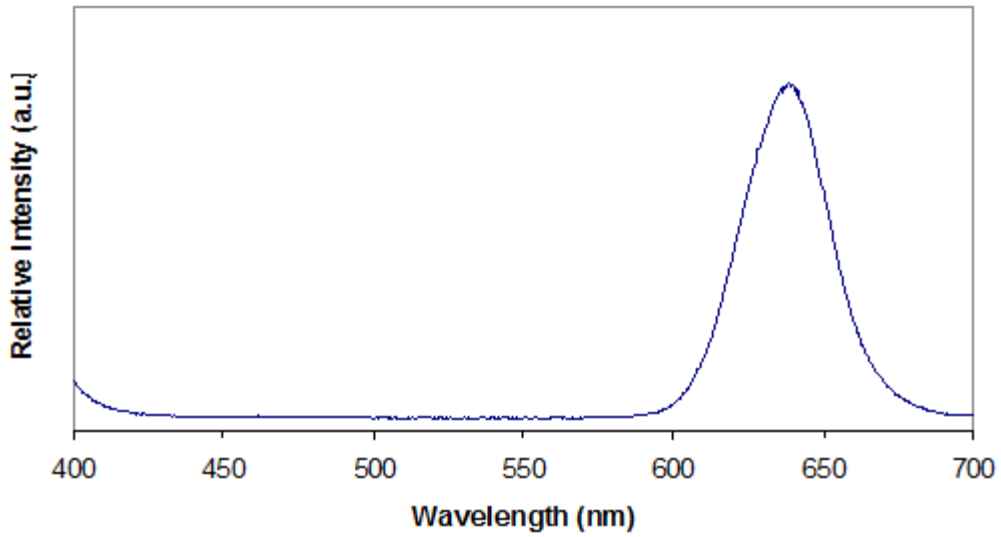

Figure 2.12 PL of CdSe emitting at 641 nm after being excited at 480 nm.

This second method was the preferable method for the synthesis of red nanoparticles. The two main reasons for this include the reaction time being much shorter for this method, 5 min in comparison with 60 h, and also more importantly the particles emit further into the red region using the second method and remain stable.

As was seen in the previous experiment in section 2.2.4, shelling with ZnS increased the intensity of the peak emitted by the nanoparticles. Therefore, the red CdSe nanoparticles synthesised were also shelled with ZnS. CdSe nanoparticles with a thin ZnS shell and thick ZnS shell were synthesised to see what effect shell thickness has on the size of the particles, emission and stability of the quantum dots. This was controlled by using different concentrations of the shelling mixture. Figure 2.13 shows the UV-vis absorption spectra of both CdSe/ZnS nanoparticles comparing the effect of using a thin or thick ZnS shell. It can be seen that whether a thick or thin shell is utilized it has little effect on where

the quantum dots absorb as the thin shelled sample absorbs at 618 nm and the thick shelled sample absorbs at 621 nm.

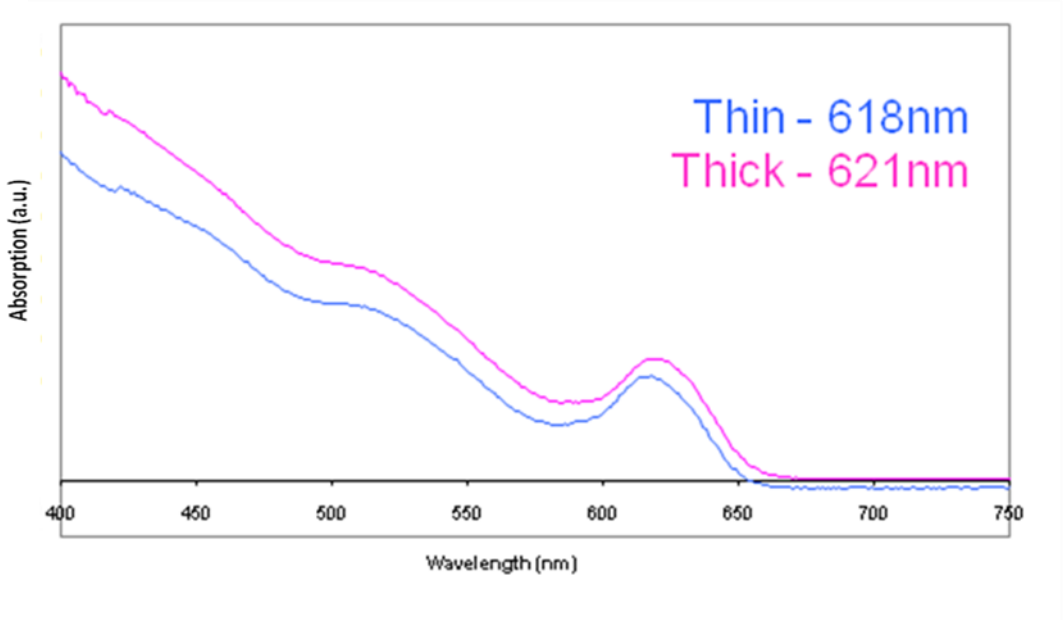

Figure 2.13 UV-Vis spectra of CdSe/ZnS nanoparticles comparing the effect of a thin and thick ZnS shell. The thin shelled CdSe absorbed at 618 nm whilst the thicker ZnS shelled CdSe absorbed at 621 nm.

Figure 2.14 shows the PL spectra comparing the effect of shelling CdSe with a thin ZnS shell and thick ZnS shell. The CdSe/ZnS nanoparticles with only a thin shell emit at 650 nm and the CdSe/ZnS nanoparticles with a thick shell emit at 651 nm. Therefore, there is only a negligible difference in emission wavelength.

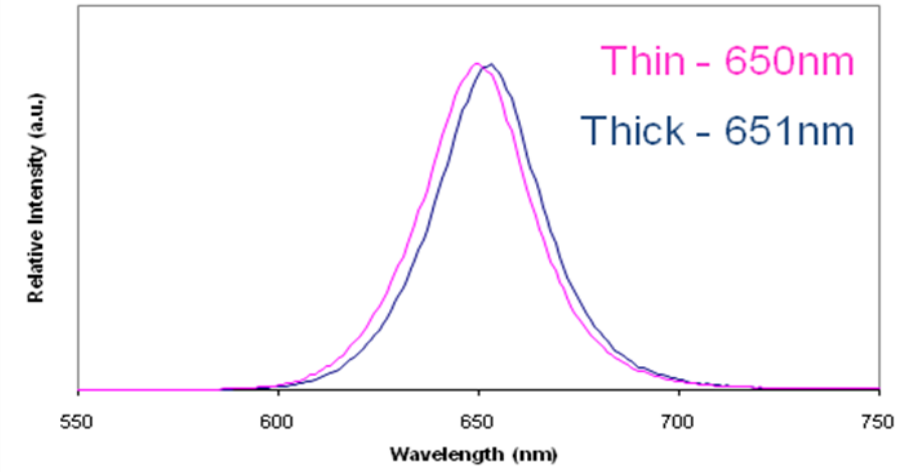

Figure 2.14 PL spectra of CdSe/ZnS nanoparticles comparing the effect of a thin and thick ZnS shell after being excited at 480 nm. The thin shelled CdSe/ZnS QDs emitted at 650 nm and the thick shelled CdSe/ZnS QDs emitted at 651 nm.

The QY of the CdSe/ZnS nanoparticles with a thin ZnS shell was measured to be 21%. Growth of a thick ZnS shell resulted in a lower QY; which was measured to be 19%. The QY was greater for the CdSe nanoparticles shelled with a thin shell as it seems the strain may be too large when the shell becomes too thick. The stability will therefore be greater for the thin shelled nanoparticles, due to less lattice strain being present resulting in a higher QY. The CdSe/ZnS nanoparticles with a thick and thin shell are pictured in Figure 2.15.

Figure 2.15 Picture of red CdSe/ZnS nanoparticles being excited by a UV lamp, the right vial contains CdSe/ZnS with a thin shell (emitting at 650 nm) and the left vial contains CdSe/ZnS with a thick shell (emitting at 651 nm).

The pXRD pattern of the CdSe/ZnS nanoparticles is shown in Figure 2.16. The XRD is made up of 3 main peaks at angles 25.8^{o}, 42.7^{o} and 50.4^{o}. The peak at 42.7^{o} is indexed to the (110) CdSe plane. The peak at 25.8^{o} could be due to either the (002) CdSe or (100) ZnS and the peak at 50.4^{o} could be due to either the (112) CdSe or (103) ZnS.

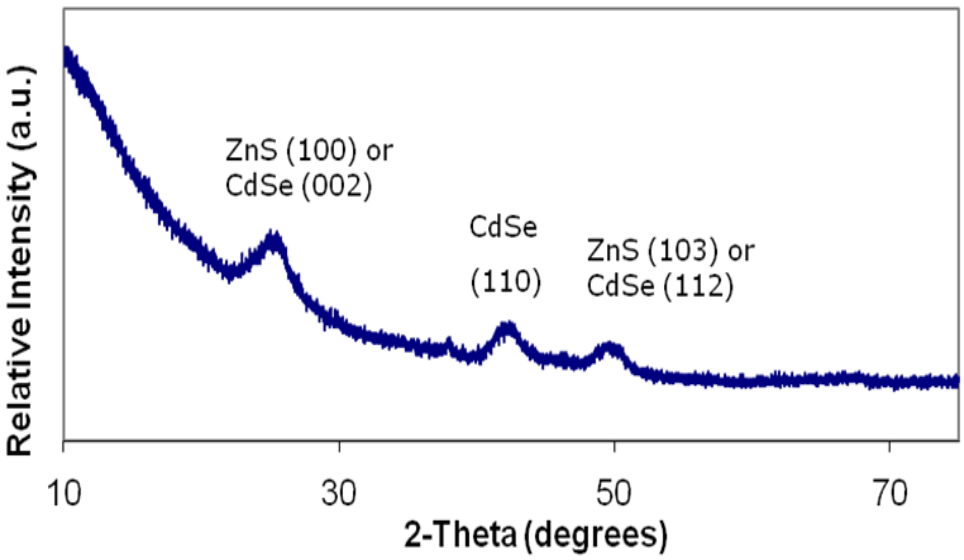

Figure 2.16 pXRD pattern from CdSe/ZnS. The XRD is made up of 3 main peaks at angles 25.8°, 42.7° and 50.4°. The peak at 42.7° is indexed to the (110) CdSe plane. The peak at 25.8° could be due to either the (002) CdSe or (100) ZnS and the peak at 50.4° could be due to either the (112) CdSe or (103) ZnS.

The TEM image of CdSe/ZnS QDs with a thick ZnS shell is shown in Figure 2.17. It was determined that the size of the particles was 4.5 nm. The CdSe/ZnS QDs with a thin shell were also 4.5 nm in size. The excess oleic acid in the sample is difficult to remove completely and some of the remaining capping agent could be seen in the image as it is blurry.

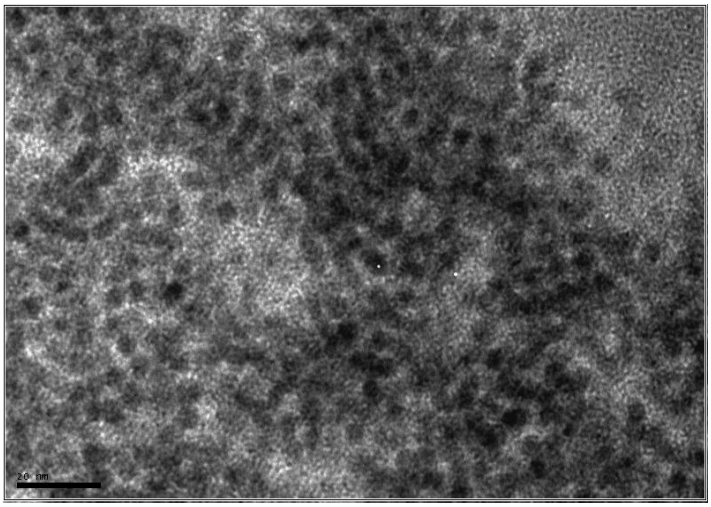

Figure 2.17 TEM image of CdSe/ZnS QDs with a thick ZnS shell approximately 4.5 nm in size (scale bar = 20 nm)

2.3 Encapsulation of the QDs

Collaborative work with A. Sutherlands' group was carried out and concentrated on thiol-containing microspheres as polymeric ligands for the immobilisation of QD samples.[113] Core/shell CdSe/ZnS QDs emitting between 548 nm and 583 nm were encapsulated and immobilised. Table 2.3 shows the samples used and the QY before and after immobilisation.

QD sample	Emission wavelength (nm)	QY in toluene (%)	QY immobilized (%)
QD1	548	16	4
QD2	562	11	4
QD3	583	14	9

Table 2.3. QD samples emission wavelengths, QY prior to immobilisation (in toluene) and following immobilisation in 1% thiol microspheres.

Jon Behrendt synthesised thiol microspheres. 4-vinylbenzyl *iso*-thiouronium chloride was first prepared for which the reaction scheme is shown in Figure 2.18. Once the thiol microspheres were synthesised the QDs were then immobilised into them. This was done by adding a solution of QDs in toluene to a suspension of thiol microspheres, also in toluene. The reaction mixture was ultra sonicated for 5 min at room temperature before being centrifuged to decant off non-immobilized QDs. The QD microspheres were resuspended in toluene by ultrasonication for 5 min before centrifugation and decantation of the supernatant. This washing procedure was repeated four more times with toluene and then twice with methanol.

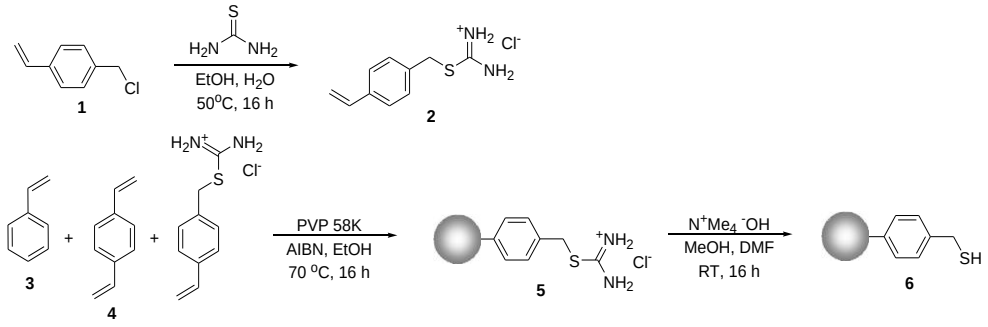

Figure 2.18 Synthesis of 4-VBTU[114] (2), dispersion co-polymerisation of 4-VBTU (2), styrene (3) and divinyl benzene (4) and conversion of thiouronium groups to thiols

Thiols were used as the binding site for the QDs as they form stable bonds with cadmium and zinc surfaces as well as being routinely used as ligands for solubilising QDs in aqueous media. Low levels of thiol groups within the polymer matrix of polystyrene microspheres allow them to function as "polymeric-ligands" for the immobilisation of QDs. Doping the microspheres with excess QDs (6-16 wt. % of the conjugate materials) remain trapped after repeated washing in swelling solvents (e.g. toluene). This is a high level of trapped QDs compared to microspheres that contained no thiol groups which immobilised very low levels of QDs (0.3 wt. %). The scanning electron microscope image, Figure 2.19, shows how the polymer particles are uniformly spherical and 1 µm diameter.

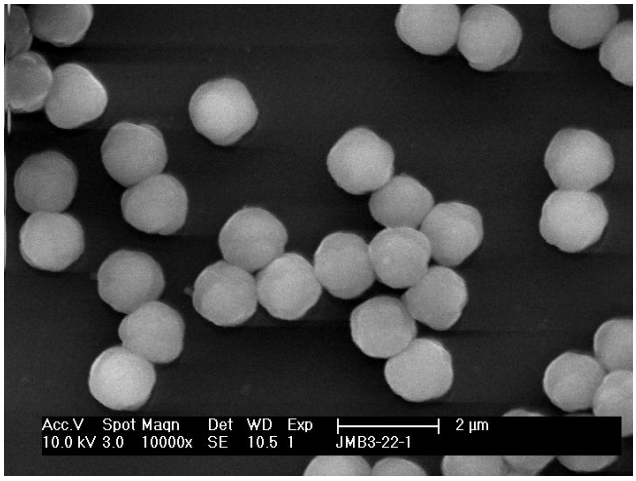

Figure 2.19 SEM image of 1 µm diameter, thiouronium-containing polystyrene microspheres 5.

Initially, one sample of QDs, emitting at 583 nm, was immobilised into the thiol microspheres. Using an optical fibre fluorescence probe a bright, characteristic PL signal was observed with no broadening or shift in the PL spectra relative to the corresponding non-immobilised QDs in toluene. Also solutions were prepared containing QD1 and QD3 in different signal ratios, and wavelengths, with respect to their PL intensity (1:2 and 2:1) and demonstrated that this ratio was closely reproduced by the QD-microspheres following immobilisation. QD encoding strategies have been explored in both biological[115-116] and combinatory chemistry,[117-118] by immobilising two or more QD samples with different emission wavelengths into a single bead. This result indicates the potential for a robust, reproducible encoding strategy, using the thiol microsphere immobilisation protocol. The PL spectra can be seen in Figure 2.20. The peak at 740 nm is due to the sample being excited at 370 nm and is caused by the machine not the samples.

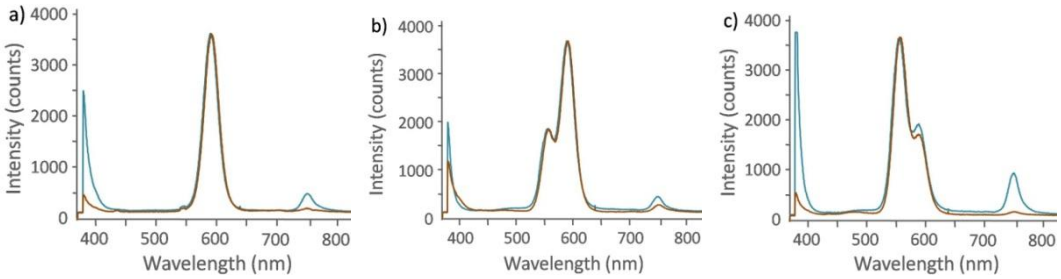

Figure 2.20 Photoluminescence spectra of QDs in solution in toluene (brown line) and immobilised into thiol microspheres (blue line). a) QD3 only, b) QD1:QD3 1:2 and c) QD1:QD3 2:1. The samples were all excied at 370 nm.

A correlation could be seen between the thickness of outer shell and overall decrease of quantum efficiency of the QDs before and after immobilisation. QD1 emitted at 548 nm and before immobilisation had a QY in toluene of 16%. However, the resultant QD-polystyrene conjugate material formed by immobilisation with 1% thiol microspheres had a QY of 4%; a 75% decrease in QY being observed. For another sample of CdSe/ZnS QDs, emitting at 562 nm, the QY decreased from 11% to 4% also; a reduction of 64%. However, for QD3 which had a thicker ZnS shell, emitting at 583 nm, the QY only reduced from 14% in solution to 9% when immobilised; a reduction in quantum efficiency of only 36%. CdSe QDs with no protective second shell were immobilised using the same procedure, however the QD-microspheres formed retained no fluorescence.

Confocal imaging studies (Figure 2.21) took cross section images at multiple focal planes of the microspheres establishing that the fluorescence emitted by the QDs was localised within the microspheres.

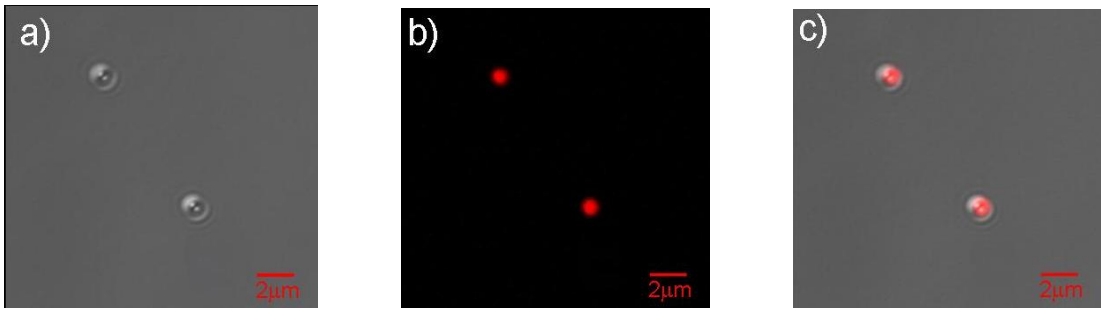

Figure 2.21 Confocal images of QD3 immobilised within thiol containing polystyrene microspheres; a) no excitation, b) argon laser excitation at 488 nm, c) composite image.

2.4 Single Nanocrystal Investigation

Work was carried out at Oxford by the J. Smith group to investigate the quality of the nanocrystal (NC), observe the heterojunction interface and to characterise the optical performance of the NC using single NC spectroscopy. The reason single NC spectroscopy was looked at was whilst ensemble data can give a good indication of the optical properties of the NC much of the information can be obscured or lost. Single NC enables vast information to be obtained which would otherwise be lost.

Initial work began with using core/shell CdSe/ZnS nanoparticles emitting at 602 nm. Phase of restored exit wave from aberration corrected TEM data shown in Figure 2.22 shows restorations obtained from data sets consisting of a focal series of 10-20 images which were combined and reconstructed using the focal and tilt series resotoration (FTSR) method which is commercially available as a plug-in online.

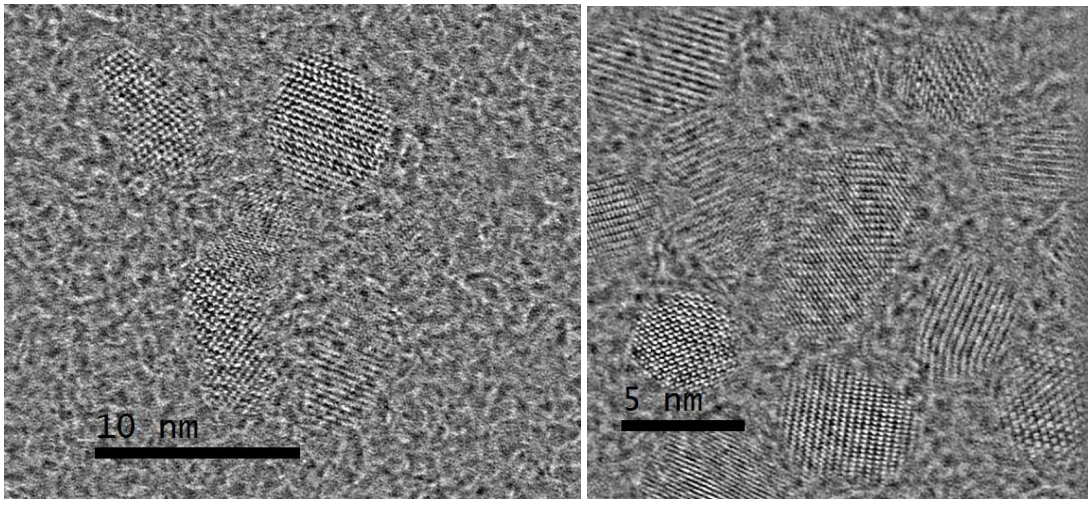

(a) (b)

Figure 2.22 Phase of restored exit wave from aberration corrected TEM data of nanoparticles emitting at 602 nm consisting of a focal series of 10-20 images that have been combined and reconstructed. (a) scale bar = 10 nm; (b) scale bar = 5 nm.

It can be seen that this sample is of a fairly homogenous size distribution however the restorations are unable to show evidence of the ZnS capping layer.

A single NC was isolated which can be seen in Figure 2.23. The single crystals was taken using a Joel 2200 aberration corrected TEM microscope used in bright field

configuration. An image series of 10 images were taken with a varying defocus. The images were combined and reconstructed using FTSR plug in for Joel Digital Micrograph.

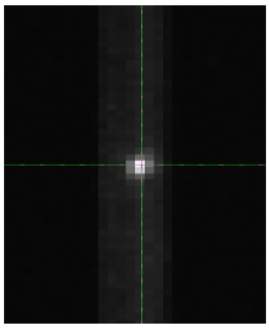

Figure 2.23 Image of a single nanocrystal taken using a Joel 2200 aberration corrected TEM microscope used in bright field configuration. A image series of 10 images were taken with a varying defocus which were combined and reconstructed using FTSR method.

A spectrum of individual quantum dots with a FWHM of 15 nm, integrated over a long timescale can be seen in Figure 2.24. Typical PL from ensemble data shows a gaussian line shape which would have a FWHM proportional to the size distribution of the ensemble. Single NC should show a lorentzian line shape which reflects the spectral line width of the band gap edge transition.

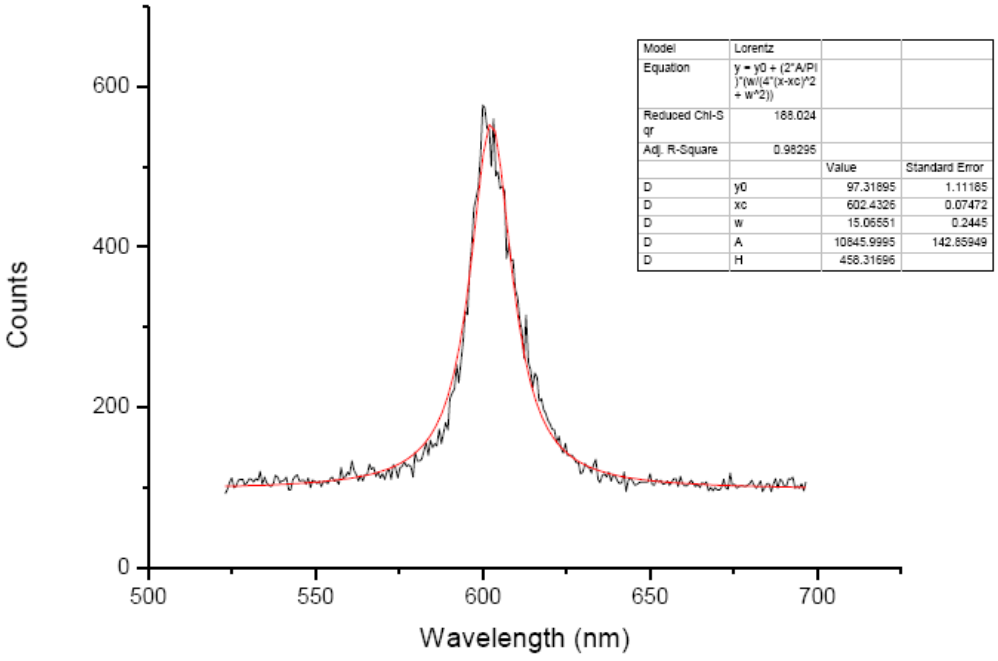

Figure 2.24 Spectra of a single nanocrystal with a 0.5 second integration time emitting at 602 nm.

Spectral data for two single CdSe/ZnS NCs are shown in Figure 2.25 shows that they are predominantly “off” with some spectral drift confirming that these NCs are not bright emitters and this was confirmed by the QY which was only 8%. The shift shows that the nanocrystal is not well passivated allowing oxygen to permeate the system therefore enhancing confinement potential (blue shift) through oxidation.[119]

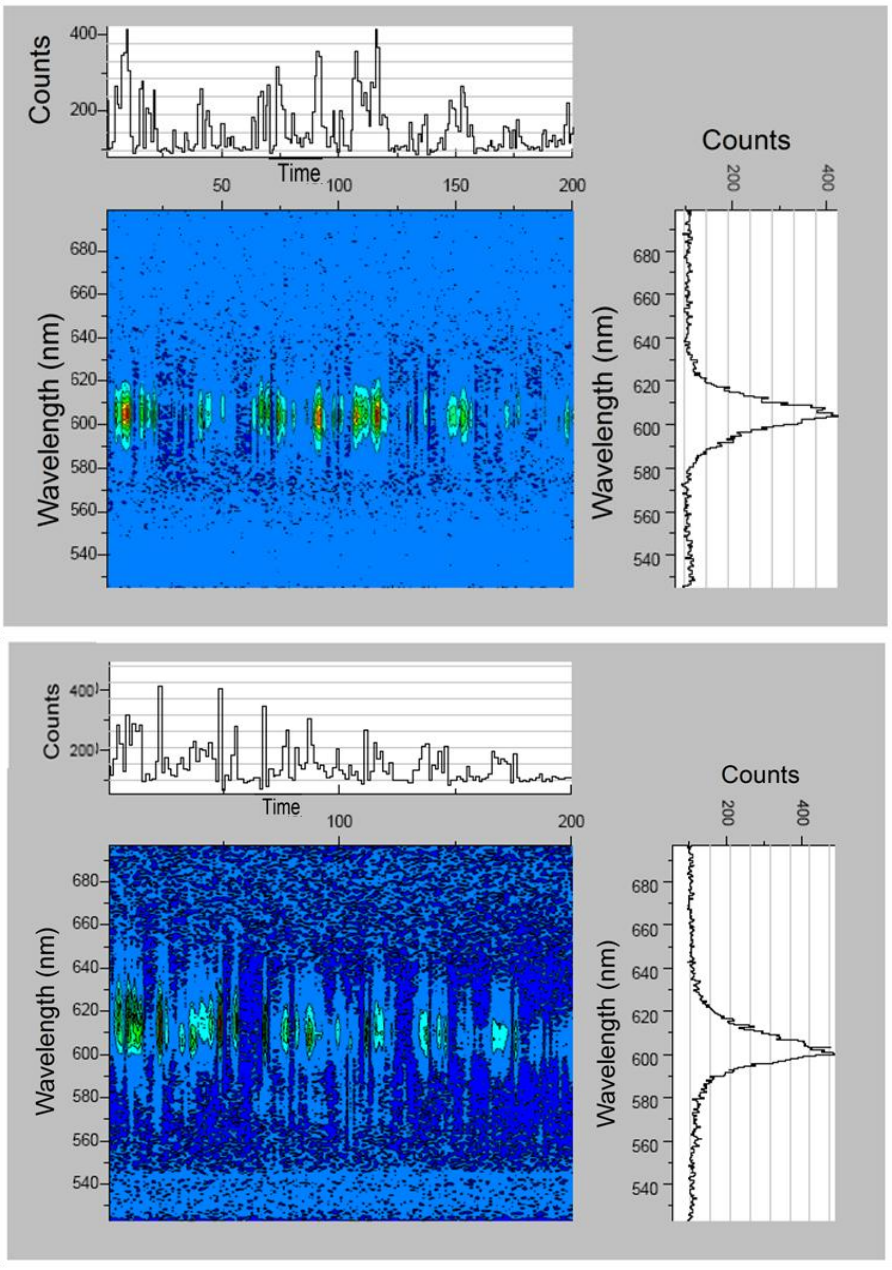

Figure 2.25 Spectral data for two single CdSe/ZnS nanocrystals emitting at 602 nm, over 200 spectra with each spectrum having a 0.5 integration time. The top graph shows how the intensity varies with time at the peak wavelength whilst the right hand graph shows the typical line shape.

To further analyse the blinking effect a further time resolved photoluminescence experiment was conducted for a period of 10 minutes. This uses a single photon avalanche detector to improve the resolution of the intensity time graph. A threshold value was taken as can be seen by the red line and a graph of frequency of the "on" and "off" durations was calculated. The blinking events were shown to have a power law dependence as shown by the linear relationship on a log log graph. The intensity time graph measured during time resolved photoluminescence can be seen in Figure 2.26. This shows how the dot was predominantly in the "off" state. The "on" and "off" states follow a power law distribution so the log graphs below the intensity time graph are to show that the sample does follow this law.

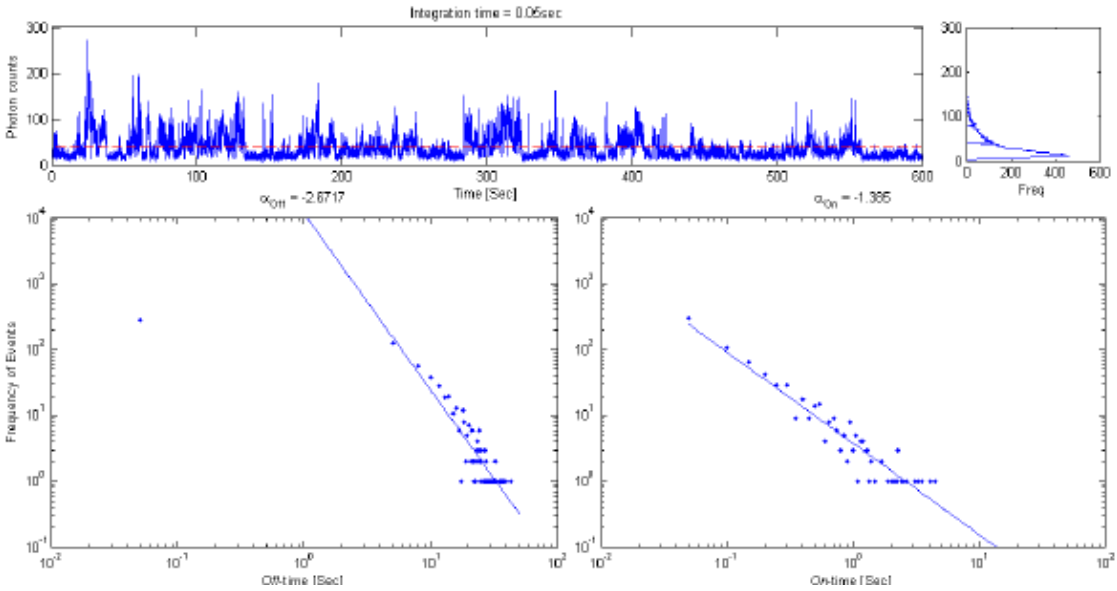

Figure 2.26 Intensity time graph showing the "off" period (left) and "on" period (right). These graphs also show that the QDs follow the power law as they form a straight line when a log graph is plotted. The QDs are considered "on" when the intensity is greater than the red line.

The lifetime of the quantum dot was measured. It can be seen that the single exponential fits with an initial fast component of 3 ns and a longer tail of34 ns. Tri exponential fits with lifetimes of 2, 14 and 63 ns. This can be seen in Figure 2.27.

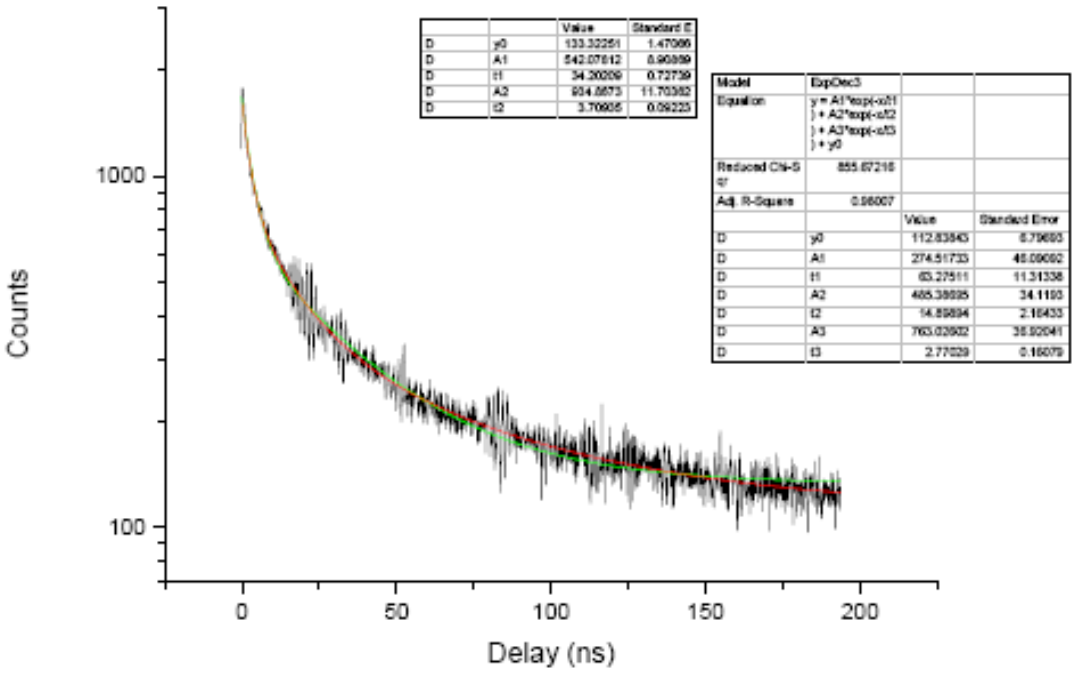

		Value	Standard E
D	y0	133.32251	1.47099
D	A1	542.07812	0.90899
D	t1	34.20209	0.72739
D	A2	934.8673	11.70382
D	t2	3.70935	0.09225

Model	ExpDec3		
Equation	y = A1*exp(-x/t1) + A2*exp(-x/t2) + A3*exp(-x/t3) + y0		
Reduced Chi-Sqr	855.67216		
Adj. R-Square	0.98007		
		Value	Standard Error
D	y0	112.83845	0.79693
D	A1	274.51733	48.09662
D	t1	63.27511	11.31338
D	A2	465.39935	34.1193
D	t2	14.85894	2.18433
D	A3	763.02932	39.92041
D	t3	2.77029	0.16079

Figure 2.27 Lifetime measurements showing single exponential fitting the lifetimes of 3 and 34 ns and tri exponential fitting with lifetimes of 2, 14 and 63 ns.

The equation relevant to Figure 2.27 is shown in Equation 2.1.

$$I = y_o + A_1 e^{-t/\tau}{}_1 + A_2 e^{-t/\tau}{}_2 + A_3 e^{-t/\tau}{}_3 \qquad \textbf{Equation 2.1}$$

As these nanocrystals were poor emitters the spectral data show that they tend to be in an “off” state. The lifetime data show that despite showing single exponential fitting, it also shows tri exponential fitting meaning that there are surface traps causing recombination via non radiative routes resulting in the “off” state.

2.5 Conclusion

In conclusion, we have grown many CdSe/ZnS core/shell nanoparticles. The cadmium selenide nanoparticles cores synthesised by the initial method of injecting the selenium into the cadmium reaction mixture provided a range which emitted from 501 – 617 nm with TDPA being essential to the overall luminescence as well as the structure.

Concentration and time were the major variables with concentration of selenium having more of an effect than increasing the growth time. Using zinc ethylxanthate and zinc stearate the CdSe cores were shelled with ZnS to have a range of CdSe/ZnS QDs emitting from 509 – 621 nm with QYs ranging from 9 – 28%. The pXRD patterns showed that peaks for both CdSe and ZnS.

Another method for the synthesis of CdSe cores enabled the growth of larger CdSe QDs which emitted at 641 nm, which when shelled by the same method as the previous CdSe QDs increased the size of the particles so that they emitted at 651 nm and absorbed at 621 nm. The pXRD pattern concluded that the peaks were typical for CdSe and ZnS.

TEM images of all CdSe/ZnS nanoparticles showed that they were all spherical in shape and monodispersed.

Immobilisation of these CdSe/ZnS QDs was successful and also with different ratios of two different QD samples. This demonstrated that this ratio was closely reproduced by the QD-microspheres following immobilisation. It was confirmed that the QDs were within the microspheres by confocal microscopy. However, the QYs of the QDs were low so that after immobilisation the highest QY was 9%. This is not high enough to be picked up by fluorescent-activated cell sorter (FACS) machines so QDs with higher QYs before immobilisation are still required.

Single nanocrystal investigations show that the QD of CdSe/ZnS measured is predominantly in the “off” state which explains why the QY was low at only 8% and that it follows the power law. Phase of restored exit wave from aberration corrected TEM data showed that the QDs were fairly homogenous in size but could not find evidence of the ZnS capping layer.

CHAPTER 3 ALLOYED NANOPARTICLES

3.1 Introduction

As described in the previous chapter, CdSe nanoparticles have tunable photoluminescence (PL) across the visible spectrum and have been extensively investigated. One problem that has been encountered by our own and other groups over the years was that growing quantum dots (QDs) tended to have some surface trap states resulting in relatively low QY's. The highest QY recorded in the previous chapter was 21%. Problems were also encountered in the synthesis of small nanoparticles that emit in the blue region.

Recent studies[120-121] have shown that the full passivation of the surface traps using ligands and thick shells can eliminate blinking. These routes can be tricky to implement and can not be used in all situations. Non blinking nanoparticles are of particular interest for biomedical imaging and opto electronics specifically for biological tagging and single photon sources. A recent study by Wang *et al.* has shown that having a graduated potential can also eliminate this phenomenon.[120] A further theoretical study by Efros *et al.* later showed that the graduated potential reduces the effect of auger recombination which is largely attributed to the recombination route for the off state in blinking.[121]

Realising that little attention has been paid to the synthesis of QDs formed with an alloyed structure through changing the constituent stoichiometries we decided to investigate the potential of QDs of this type for wider tuning of emission with high PL efficiency.

3.2 Results and Discussion

3.2.1 Synthesis of $Zn_xCd_{x-1}S$ Nanoparticles

The synthesis of blue nanoparticles is very challenging using core/shell systems that include cadmium, so work turned to using alloyed systems that could successfully produce blue nanoparticles. Sulfur powder was dissolved in ODE which was injected quickly into a solution of cadmium oxide and zinc oxide dissolved in oleic acid and ODE at 200 ^{o}C. A series of nanoparticles was prepared where the proportion of zinc was changed with the proportion of cadmium remaining the same throughout. The PL spectra of two of the

samples show that as the value of x increases a blue shift is observed. Table 3.1 shows the emission wavelength and the size of the nanoparticles synthesised. x is equal to the number of mmols of zinc oxide and sulfur that was used.

x	Wavelength (nm)	Size (nm)
0.2	426	2.5
0.3	400	2

Table 3.1 Table showing the value of x, emission wavelength and size of $Zn_xCd_{x-1}S$ nanoparticles synthesised.

When x is equal to 0.2 the particles emit at 426 nm, however when x is increased to 0.3 the particles that are synthesised are smaller as they emit at 400 nm. The normalised PL spectra are shown in Figure 3.1. When x = 0.2 the sample was excited at 360 nm and when x = 0.3 the sample was excited at 350 nm.

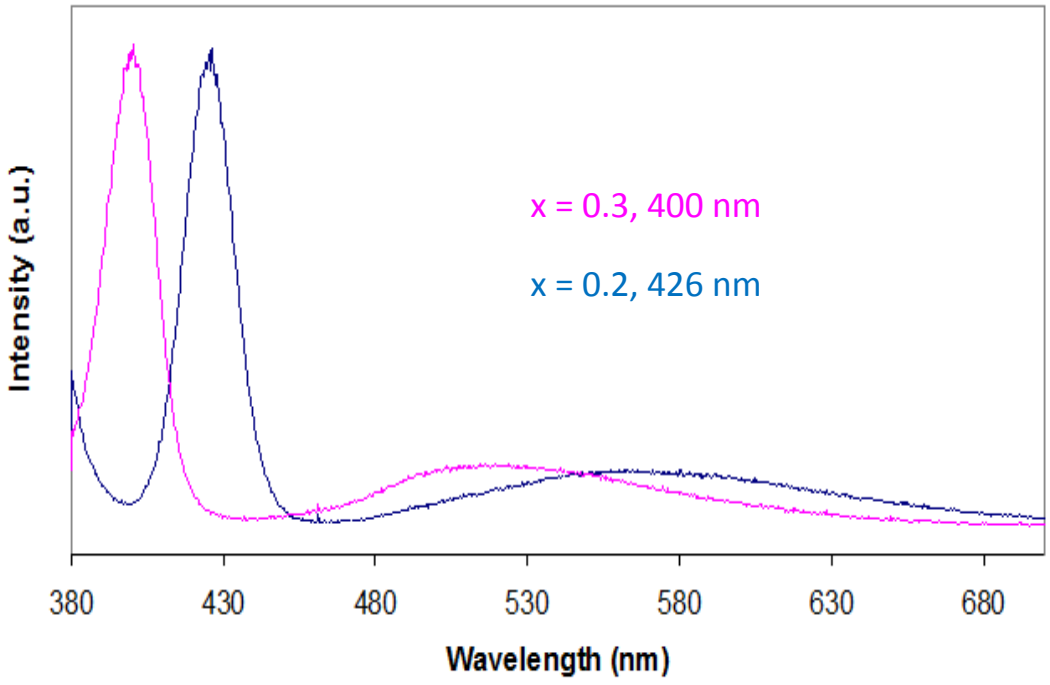

Figure 3.1 Normalised PL spectra of 2 different $Zn_xCd_{x-1}S$ samples. When x = 0.2 the sample was excited at 360 nm and when x = 0.3 the sample was excited at 350 nm.

The TEM image shown in Figure 3.2a shows that the size of the nanoparticles formed when x = 0.2 the nanoparticles was ~2 nm. However, when x = 0.3 they were ~2.5 nm, shown in Figure 3.2b.

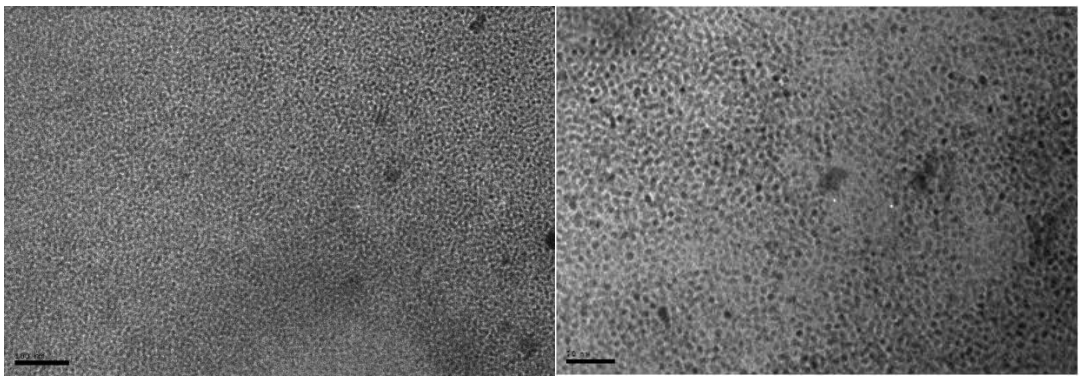

(a) (b)

Figure 3.2 TEM image of $Zn_xCd_{1-x}S$, where (a) x = 0.2, ~2 nm in size (scale of 100 nm), emitting at 400 nm; b) x = 0.3, ~ 2.5 nm in size (scale of 50 nm), emitting at 426 nm.

The pXRD pattern of the ~2.5 nm $Zn_{0.53}Cd_{0.47}S$ alloy is shown in Figure 3.3. Strong reflections can be seen at angles of 27.7°, 46.4° and 54.8° which are indexed to the scattering from (002), (110) and (112) planes respectively. It is consistent with the pattern expected for alloyed nanoparticles as the peaks are considerably shifted from the bulk reflections for both CdS and ZnS due to Vegard's law which is an approximate linear empirical rule that states that there is a linear relation between the concentrations of the constituent elements and the crystal lattice parameter of an alloy.[122]

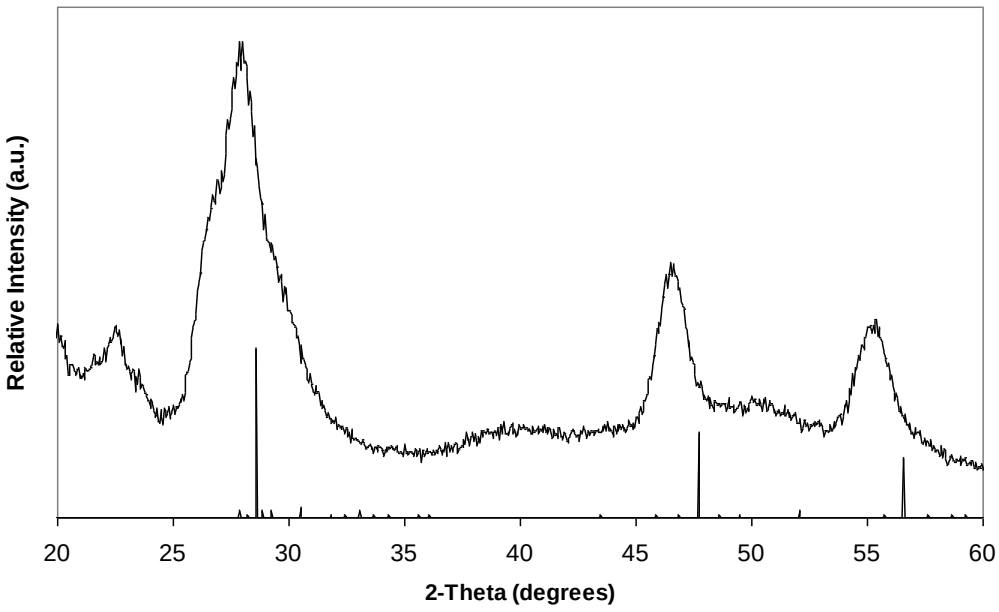

Figure 3.3 p-XRD pattern of $Zn_xCd_{1-x}S$ core nanoparticles. The XRD is made up of 3 main peaks at angles 27.7°, 46.4° and 54.8° that are indexed to the scattering from (002), (110) and (112) planes respectively of the zinc cadmium sulfide alloy. Also indicated are the bulk peaks for wurtzite-8H ZnS.

3.2 $Cd_{1-x}Zn_xSe_{1-y}S_y$ Nanoparticles

To increase the emission range of the alloyed nanoparticles, work began on a different alloy system that also contained selenium. This should lead to an increase in size of the particles with these larger particles emitting in the red region with a blue shift being observed as the particles decreased in size when smaller concentrations of selenium were used. The particles were synthesised using cadmium oxide and zinc acetate dissolved in oleic acid and ODE. The degassed solution was raised to 310 °C whereupon dissolved sulfur and selenium prepared separately in TOP were added together and then quickly injected into the hot cadmium/zinc solution. There was a 5 min growth period at 300 °C before cooling and isolation took place.

There is an indication that selenium is more reactive than sulfur towards cadmium under rapid nucleation and growth conditions.[123] This would suggest that the core of these alloyed nanoparticles is pure CdSe; once the concentration of selenium decreases, sulfur begins to react with cadmium and then finally zinc. The reactivity of these chemicals when

in proximity with each other would suggest the outermost part of these particles is primarily ZnS, as cadmium is more reactive than zinc.

We therefore prepared a series of QDs where the concentrations of cadmium and zinc were kept constant but the concentrations of sulfur and selenium were varied. Firstly, the sulfur concentration was kept constant at 4 mmol whilst the concentration of selenium varied from 0.025 mmol to 0.4 mmol. A range from 582 – 626 nm was achieved with QYs ranging from 7- 70%. The normalised PL spectra of these nanoparticles can be seen in Figure 3.4. All samples were excited at 480 nm.

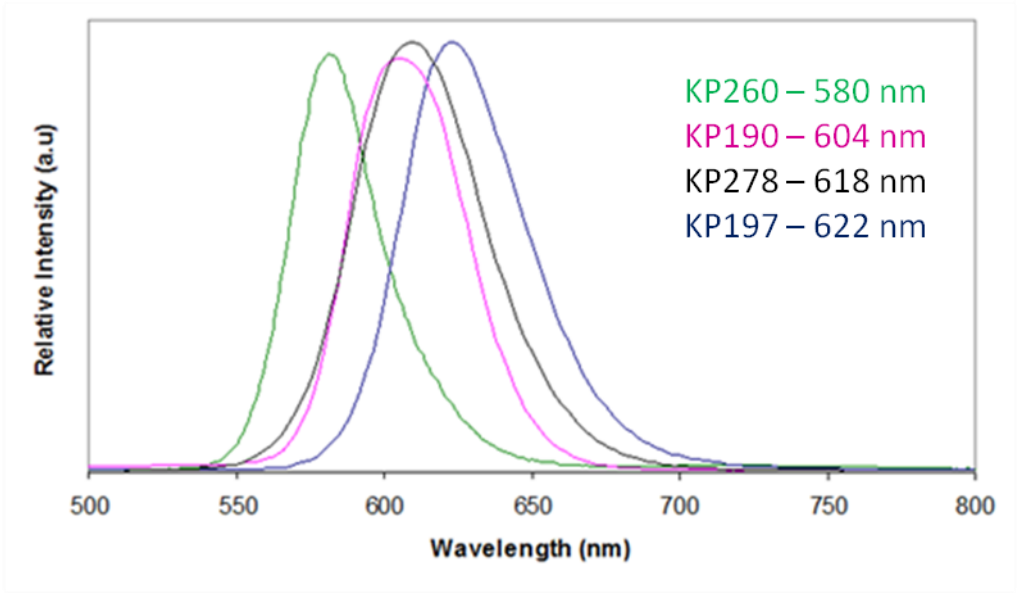

Figure 3.4 Normalised PL spectra where Cd, Zn, S concentrations were kept constant and Se concentrations were varied which were all excited at 480 nm. The samples emitted at 580 nm, 604 nm, 618 nm and 622 nm.

It can be seen that by changing the concentration, the size of the particles is affected and a dramatic effect on the QY of the resulting nanoparticles is also noted. Table 3.2 summarises the reaction conditions and the resultant emission maxima and quantum yields recorded. In this set of experiments it was seen that the using 0.1 mmols of selenium gave nanoparticles with a QY of 70% which is very high, emitting in the orange region at 580 nm. Two samples used the same amount of sulfur and selenium but there is a difference of 41 nm. The reason for this is that the growth period for these two experiments was different. The sample that emits at 580 nm had a growth period of 3 min, however by increasing this to 5 min the sample emits at 621 nm. A growth period of 3 min seems to be the optimum growth time as the extra 2 minutes caused a QY drop of 20%.

Experiment	Selenium (mmol)	Sulfur (mmol)	Emission (nm)	QY (%)
KP260	0.1	4	580	70
KP190	0.025	4	604	7
KP278	0.3	4	618	25
KP197	0.1	4	622	50

Table 3.2. Table showing the different selenium concentrations used and the resulting emission wavelengths and QY. All samples were excited at 480 nm.

The sizes of the particles were measured by TEM to be ~5 nm and Figure 3.5 shows the alloyed sample with the greatest QY measurement of 70%.

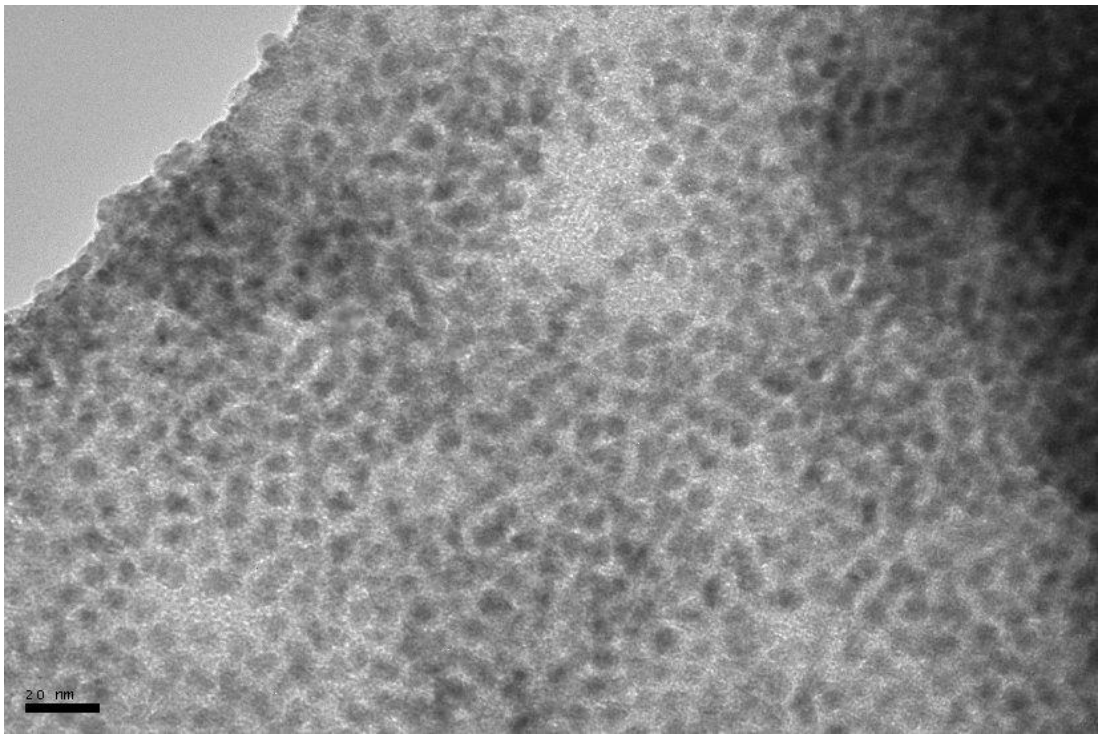

Figure 3.5 TEM of $Cd_{1-x}Zn_xSe_{1-y}S_y$ QDs emitting at 580 nm with a QY of 70%, ~5 nm in size (scale bar = 20 nm).

The pXRD patterns were recorded for four different samples and can be seen in Figure 3.6. This includes a sample that was prepared using 2.3 mmol of sulfur and 1 mmol of selenium. This sample emitted at 622 nm and had a QY of 30%. The pXRD pattern is made up of 3 main peaks at angles of approximately 27°, 45° and 53.5°. The diffraction

patterns of these alloys show how the change in selenium concentration causes a difference in the resulting position of the diffraction peaks. It can be seen that as the concentration of selenium increases with respect to sulfur, the peaks shift to a smaller angle as it is moving towards the position of bulk CdSe and away from bulk CdS and ZnS. Also, the sample containing the most selenium in relation to sulfur has broad peaks and as expected, the sample containing the least amount of selenium has the sharpest peaks. The peaks are significantly shifted for these alloys when compared to what is expected for the peaks for bulk CdS and ZnS. This is consistent with what is expected for alloyed nanoparticles.

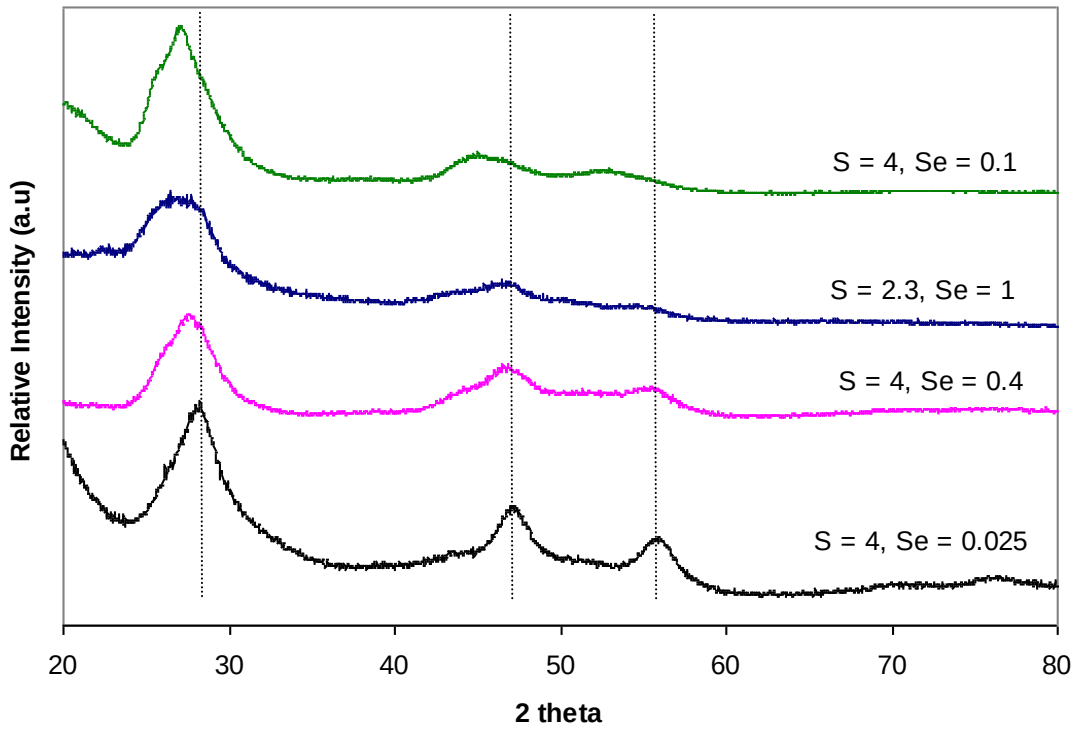

Figure 3.6 The pXRD patterns of $Cd_{1-x}Zn_xSe_{1-y}S_y$ nanoparticles have 3 main peaks at angles of approximately 27°, 45° and 53.5° that are indexed to the scattering from (002), (110) and (112) planes respectively of the cadmium zinc selenium sulfide alloy.

A second series of nanoparticles was prepared where the concentration of selenium was kept constant at 0.1 mmol and the number of moles of sulfur used was varied. The normalised PL spectra of these samples can be seen in Figure 3.7. Most of the samples emitted over a narrow range of 40 nm, however one sample emitted at 390 nm

with a QY of this sample to be only 3%. This is attributed to the sample probably possessing a lot of surface traps.

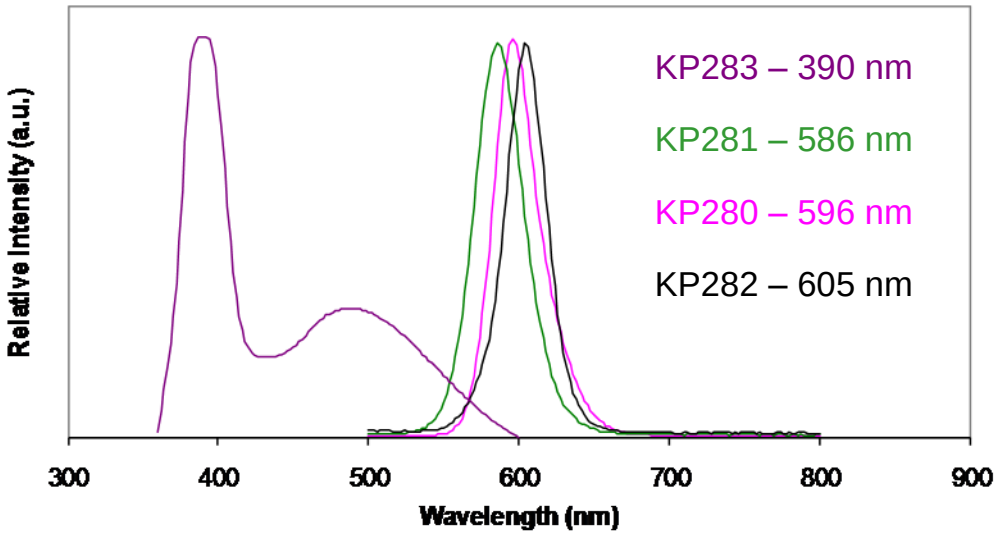

Figure 3.7 Normalised PL spectra where Cd, Zn, Se concentrations were kept constant and sulfur concentrations were changed which were all excited at 480 nm except the sample emitting at 390 nm which was excited at 340 nm. The samples emitted at 390 nm, 586 nm, 596 nm and 605 nm.

Table 3.3 shows how varying concentration of sulfur effects the position of the emission wavelength and the resulting QY.

Experiment	Selenium (mmol)	Sulfur (mmol)	Emission (nm)	QY (%)
KP283	0.1	10	390	3
KP284	0.1	8	400	7
KP281	0.1	6	586	67
KP280	0.1	3	596	65
KP282	0.1	1	605	59

Table 3.3 Table showing the different sulfur concentrations and the resulting emission wavelength and QY. All samples were excited at 480 nm.

The QY increases with increasing sulfur concentrations for 1 to 6 mmol then decreases dramatically from nearly 70% to less than 10% when more than 6 mmol of sulfur is used. It is also observed that as the concentration of sulfur increased the size of the particles synthesised decreased. The TEM of the sample using the smallest amount of sulfur and therefore the largest particles and can be seen in Figure 3.8. The nanoparticles are ~ 5 nm in size.

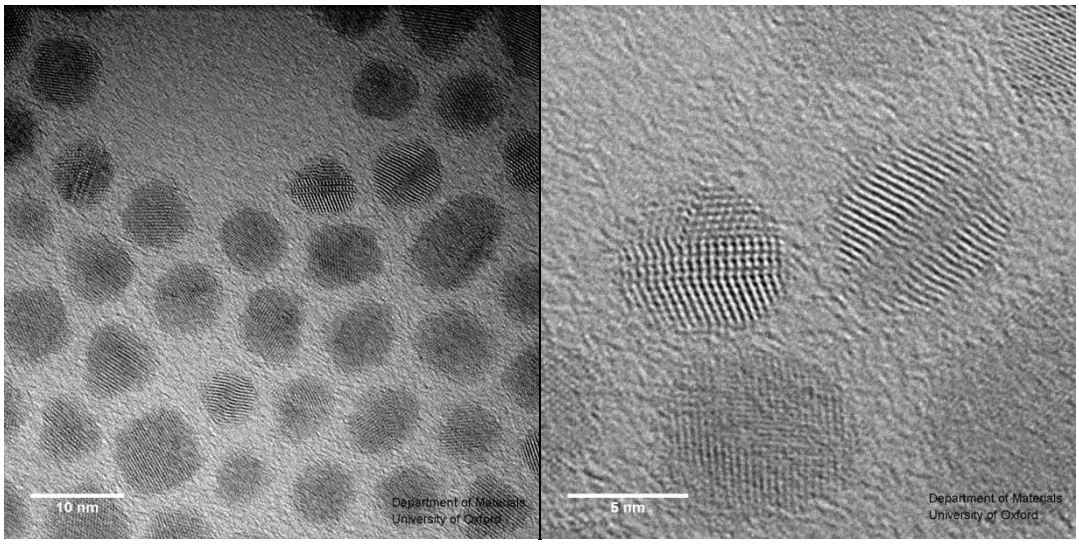

(a) (b)

Figure 3.8 TEM image of $Cd_{1-x}Zn_xSe_{1-y}S_y$ QDs emitting at 605 nm (KP282) (a) scale bar = 10 nm, (b) scale bar = 5 nm.[124]

The pXRD patterns of $Cd_{1-x}Zn_xSe_{1-y}S_y$ with different sulfur concentrations are shown in Figure 3.9. The pXRD patterns are made up of 3 main peaks at angles of 26.5°, 44.5° and 54°. The diffraction patterns of these alloys show how the change in sulfur concentration causes a difference in the resulting position of the diffraction peaks. As discussed, the peaks can be indexed to wurtzite ZnS with an angle shift due to the influence of CdSe and CdS in the alloy (Vegard's law).[122] The XRD shows that as the concentration of sulfur increases, the position of the peaks shifts to a greater angle.

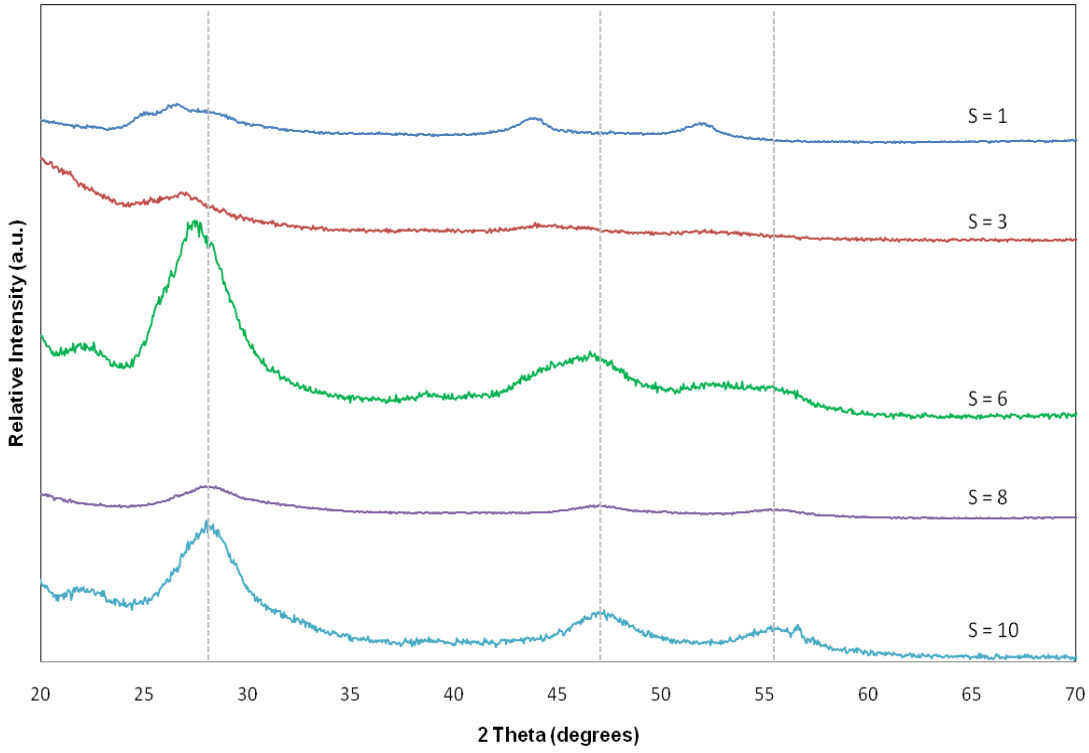

Figure 3.9 pXRD patterns of $Cd_{1-x}Zn_xSe_{1-y}S_y$ with increasing concentrations of sulfur and selenium concentration being kept at 0.1 mmol. The 3 main peaks being compared at approximately 26.5°, 44.5° and 54° indexed to the scattering from (002), (110) and (112) planes respectively.

The results reported here are reproducible as all these reactions using the different concentrations of selenium and sulfur were carried out multiple times resulting in comparable emission wavelengths and QYs.

Inductively coupled plasma atomic emission spectroscopy (ICP-AES) was carried out on a few samples to identify the difference in chemical composition. The three samples run had emissions of 580 nm (QY = 70%), 616 nm (QY = 25%) and 596 nm (QY = 68%). Each sample was prepared using 4 mmol of zinc acetate and 0.4 mmol of cadmium oxide with varying concentrations of sulfur and selenium. For the sample emitting at 596 nm the concentration of sulfur was 3 mmol and selenium was 0.1 mmol. The concentrations of the four main elements within the nanoparticles synthesised was measured and can be seen in Table 3.4. It also shows the number of moles entered into the reaction and the number of moles that were incorporated into the nanoparticles. The empirical formula for this sample is $Cd_{0.8}Zn_1S_{1.7}Se_{0.02}$ with an error in stoichiometry of 5.56%. The standard deviation for this is approximately 0.2 at 0.5 ppm with the reproducibility of 0.003 ppm.

Element	Concentration (ppm)	Input (mmol)	Output (mmol)
Cadmium	60.39	0.35	0.537
Zinc	47.07	1.43	0.72
Sulfur	38.91	3	1.216
Selenium	1.041	0.1	0.0131

Table 3.4 ICP-AES data for sample emitting at 596 nm. Sulfur = 3 mmol, selenium = 0.1 mmol.

A graph to show the output versus input ratios can be seen in Figure 3.10.

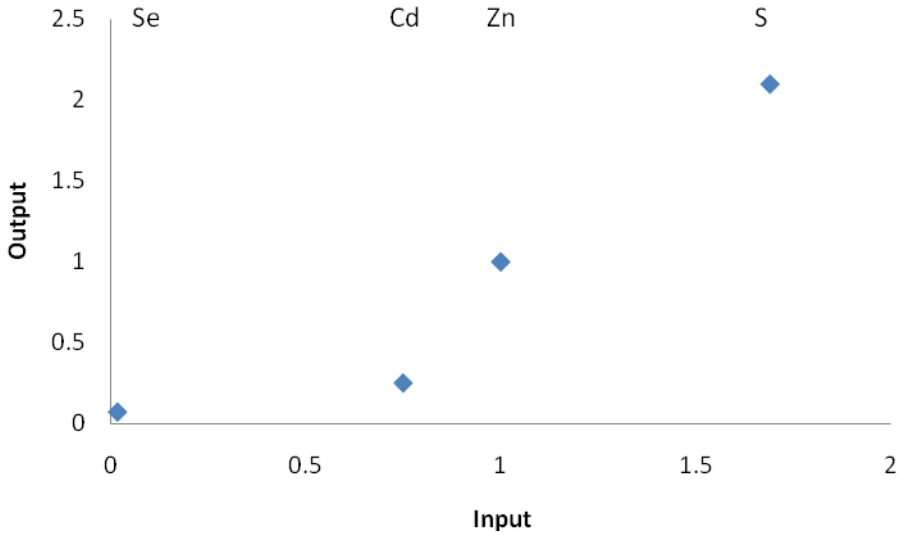

Figure 3.10 A graph showing the input and output ratios of cadmium, zinc, sulfur and selenium in the sample emitting at 596 nm.

The concentration of the sample emitting at 580 nm, containing 4 mmol of sulfur and 0.1 mmol of selenium, is shown in Table 3.5. The empirical formula for this sample is $Cd_{0.7}Zn_1S_{2.64}Se_{0.03}$ with a large error in stoichiometry of 51%. The reason for this large error is unknown but follows the same pattern as the other two samples with smaller stoichiometry errors. A graph of input versus output can be seen in Figure 3.11.

Element	Concentration (ppm)	Input (mmol)	Output (mmol)
Cadmium	72.75	0.35	0.647
Zinc	55.39	1.43	0.847
Sulfur	71.72	4	2.24
Selenium	2.234	0.1	0.0283

Table 3.5 ICP-AES data for sample emitting at 580 nm. Sulfur = 4 mmol, selenium = 0.1 mmol

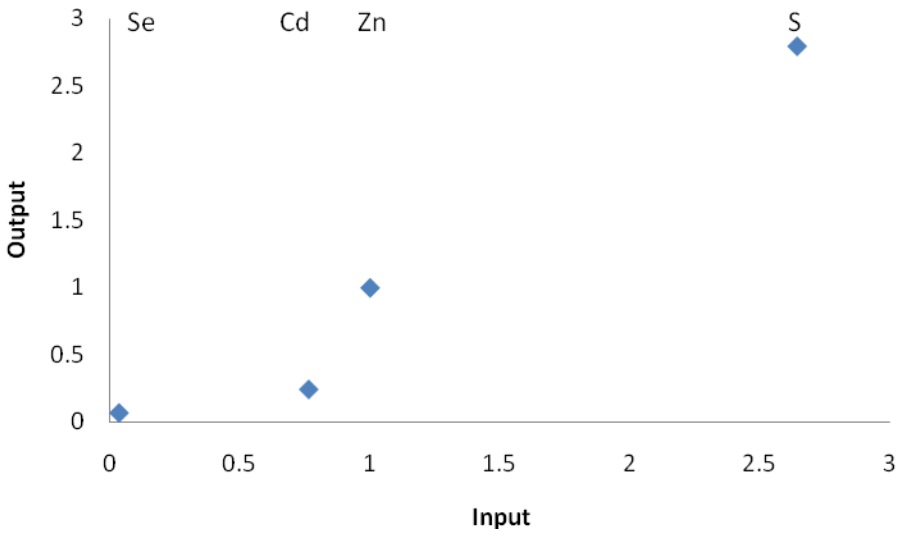

Figure 3.11 A graph showing the input and output ratios of cadmium, zinc, sulfur and selenium in the sample emitting at 580 nm.

The final sample that had the concentrations measured emitted at 616 nm which was synthesised using 4 mmol of sulfur and 0.3 mmol of selenium, is shown in Table 3.6. The empirical formula for the sample is $Cd_{0.45}Zn_1S_{1.54}Se_{0.02}$ with an error in stoichiometry of 3%. A graph of input versus output can be seen in Figure 3.12.

Element	Concentration (ppm)	Input (mmol)	Output (mmol)
Cadmium	26.59	0.35	0.23
Zinc	34.33	1.43	0.52
Sulfur	25.22	4	0.79
Selenium	0.727	0.3	0.009

Table 3.6 ICP-AES data for sample emitting at 616 nm. Sulfur = 4 mmol, selenium = 0.3 mmol

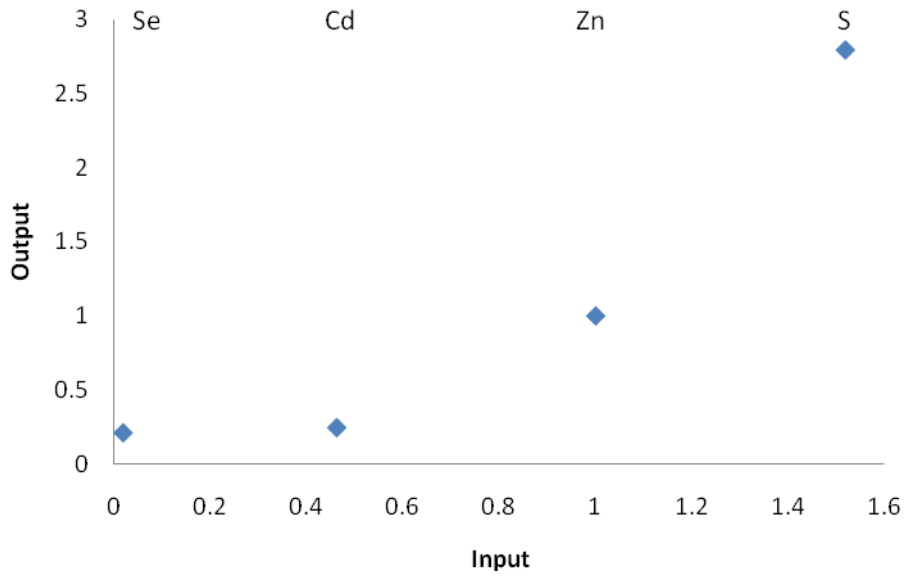

Figure 3.12 A graph showing the input and output ratios of cadmium, zinc, sulfur and selenium in the sample emitting at 616 nm.

Reproducibility is 0.01 for the second two samples and the standard deviation is also better than 0.01 at 0.5 ppm.

3.3 Encapsulation of QDs

As discussed in Chapter 2 collaborative work with the group of A. Sutherlands' concentrated on thiol-containing microspheres as polymeric ligands for the immobilisation of QD samples.[113] It was observed that before immobilization QYs were no higher than 16%. QDs described in this chapter had much higher QYs and seemed more stable so

immobilization of these was also carried out. The two samples used emitted at 605 nm and 622 nm with QYs of 60% and 50% respectively.

The QY of the sample emitting at 605 nm was reduced from 60% in solution to 23% when immobilised (a reduction of 62%), and the QY of the sample emitting at 622 nm was reduced from 50% in solution to 25% immobilised (a reduction of 50%). Despite this loss of QY upon immobilisation, the QD-polymer composite materials formed have relatively impressive quantum efficiencies compared to other QD-microspheres in the literature.[125] Also, for all QD samples, there was no broadening or shift in the PL spectra of the immobilised QDs compared to the corresponding non-immobilised QDs in toluene, suggesting that they have not been subject to chemical surface degradation.

Following several washes with toluene to remove any excess QDs, the "as formed" QD-microspheres can be resuspended in a range of aprotic (e.g. chloroform, toluene) and protic (e.g. methanol) solvents. However, upon resuspension in water, the microspheres have a tendency to aggregate. This phenomenon is thought to be due to inter-particle hydrophobic interactions caused by QDs located near the surface of the polystyrene particle, which are partially exposed.[126] It was found that these interactions can be masked by treating the QD-microspheres with an aqueous solution of the amphiphilic polymer PVP (Mn = 58 000 g mol^{-1}, 1% w/w). Following repeated washes with water (up to 10 times), the resultant PVP-QD-microspheres can be resuspended in water to form stable colloids, suggesting that the hydrophobic region of the PVP is coating any surface QDs, while exposing its hydrophilic region to the aqueous environment. Following treatment of a sample of QD-microspheres (QY = 23%) with PVP in this manner, the PL maxima remained unchanged and the QY was reduced to 14%. This is a less marked reduction than has been reported previously where non-immobilised QDs (made by a very similar synthetic method) have been rendered aqueous compatible by ligand exchange with mercatopropionic acid.[114] Due to their suitable sizes,[127] high colloidal stability (>24 hours at concentrations of 1 mg ml^{-1}) and relatively high quantum efficiency, we believe our PVP-QD-microspheres may find utility in bioimaging and encoding applications.[127]

3.4 Two-photon excitation

Multiphoton excitation was carried out by the Magennis group on one of the alloyed samples that emitted at 580 nm with an initial quantum yield of 70%. The emission spectrum of this sample, excited at 700 nm with a femtosecond Ti-Sapphire laser is shown in Figure 3.13. Quantum dot emission at 580 nm and scattered laser light is observed. The sample does not absorb at 700 nm (via one-photon absorption), hence a multiphoton process must be operating.

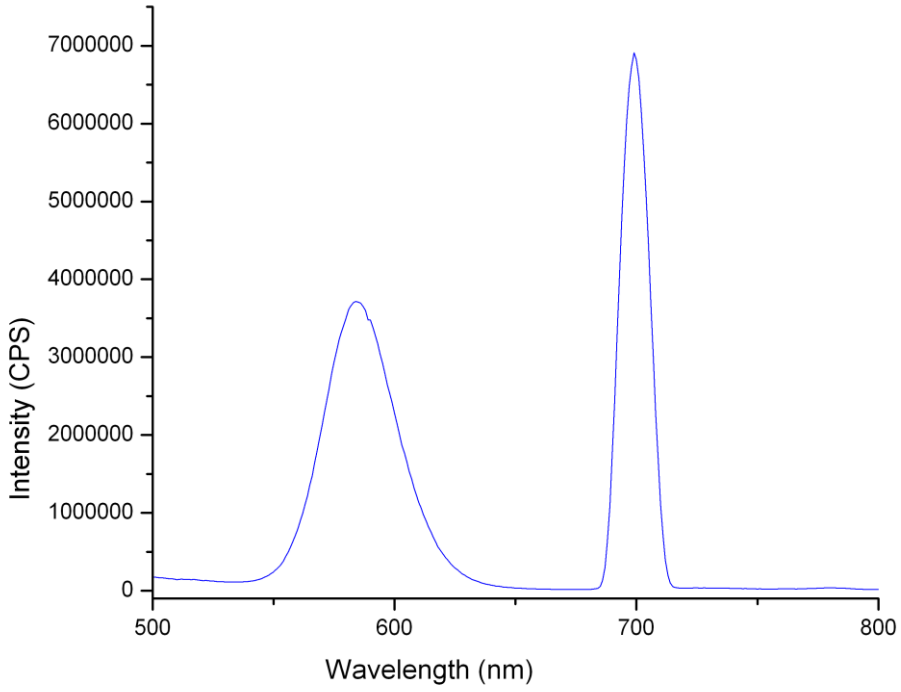

Figure 3.13 Emission spectrum of a sample emitting at 580 nm following excitation at 700 nm.

It was established that a multiphoton process was taking place but it was not clear whether it was a two or three photon process. Intensity is proportional to power^N where N = 1 is a one photon process, N = 2 is a two-photon process and N = 3 is a three-photon process and so on. A plot of log-intensity versus log-power was done and can be seen in Figure 3.14. The slope of the log-log plot is ~2 showing that a two-photon excitation process is what is occurring. The R^2 value shows that all the points lie in a straight line and has a value of ~1. This line is a perfect fit for a two-photon process.

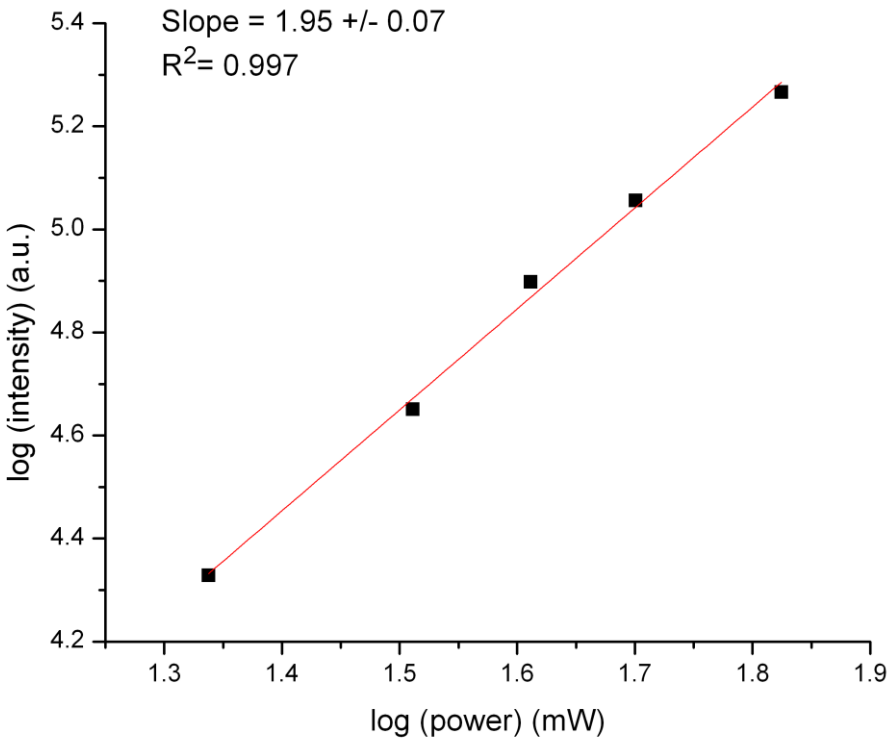

Figure 3.14 Plot of emission intensity vs. power. Slope of log-log plot is 2.

As a two-photon process is possible, it has multiple advantages. These include the reduction of photobleaching and damage to quantum dots using this method.[128] It may also allow the use of these quantum dots as biomarkers and 3D localisation of photoactivation allowing 3D imaging and data storage.

3.4 Single Nanocrystal Investigation

In the previous chapter we saw that by carrying out a single nanocrystal investigation blinking of the nanocrystals can be observed. J. Smith's group did the same studies on two separate alloyed nanocrystals synthesised. The KP282 sample had a QY of 59%, emitting at 605 nm, so it was known that they were bright emitters; however lifetimes of the nanocrystals were unknown. Figure 3.15 shows the spectral data of a nanocrystal over 0.5 s integration time.

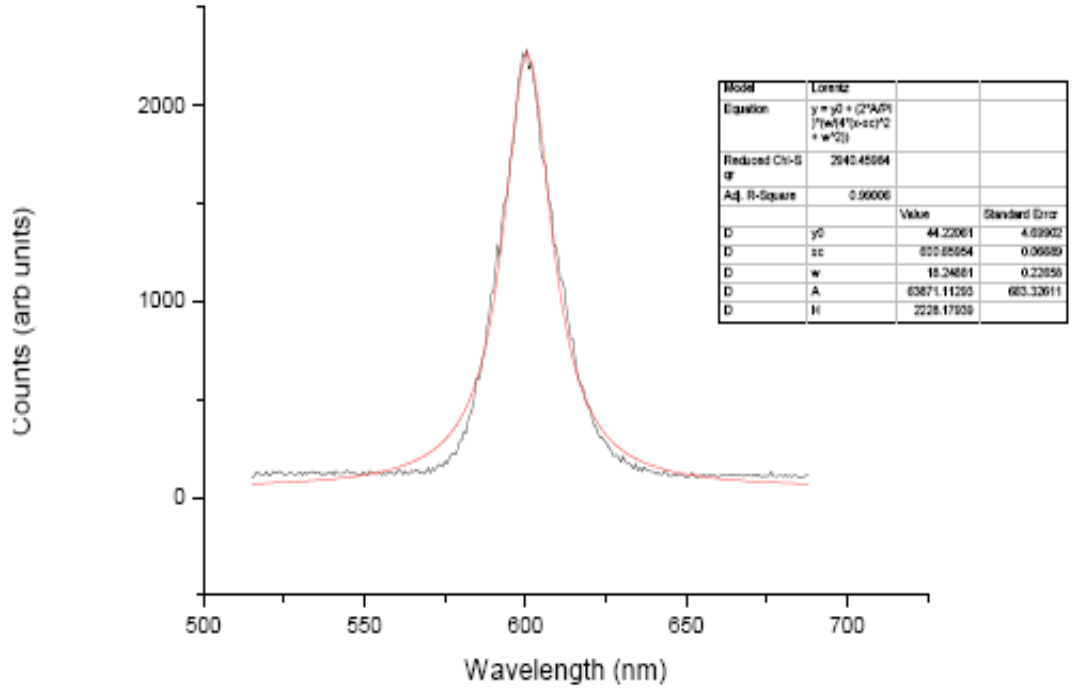

Figure 3.15 Spectral data for an alloyed nanocrystal emitting at 605 nm (KP282) over 0.5 s integration time.

As the FWHM is measured to be between 16-18 nm it was necessary to confirm single nanocrystal status, as the FWHM value is large, by Hanbury Brown Twist (HBT) antibunching measurements. A dip below 50% was observed showing that it is single nanocrystal.[129] The horns are an artefact of the detectors and can be seen in Figure 3.16.

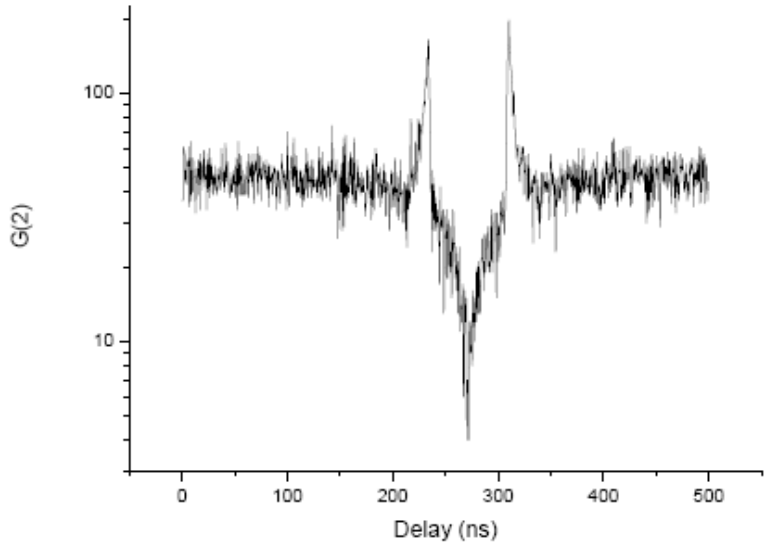

Figure 3.16 A typical HBT measurement showing a single emitter due to a dip below 50% being observed.

Blinking investigations show almost no long scale blinking with no spectral drift, only a few nms which is exceptional. These particles are very good emitters when they are in the "on" state. The spectral data for two single alloyed nanocrystals emitting at 605 nm with a 0.5 s integration time can be seen in Figure 3.17. The lack of blue shift in the spectral time graphs shows a well passivated nanocrystal as no oxygen can permeate the system therefore not enhancing confinement potential (blue shift) through oxidation.[119]

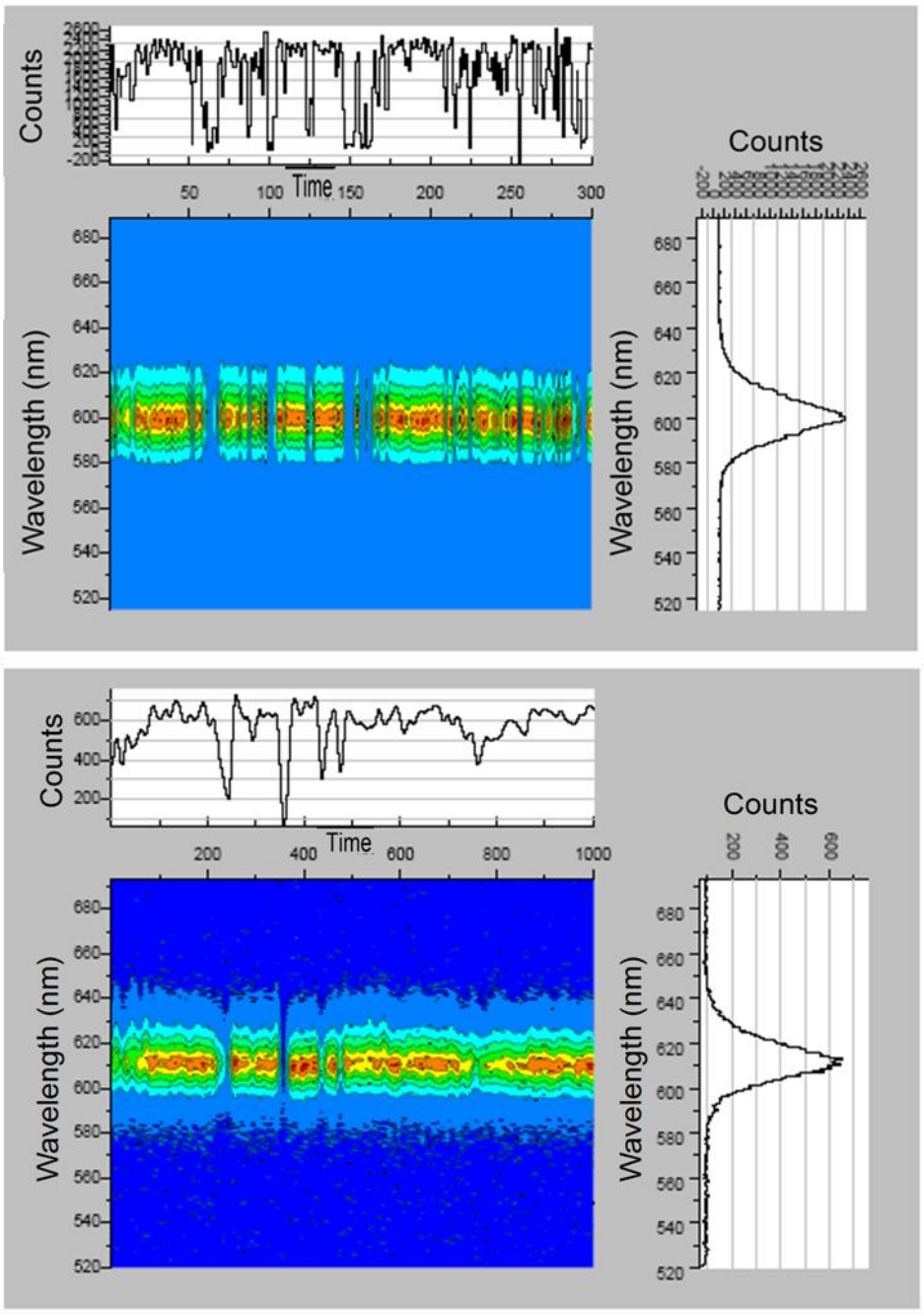

Figure 3.17 Spectral data for two single alloyed nanocrystals emitting at 605 nm (KP282) over 200 spectra with a 0.5 s integration time.

Blinking investigations show that the nanocrystal blinks typically on short time scales. Initial investigation showed that a 10 minute time trace was insufficient to get an accurate "on" time exponent, on this sample, however going to a long time intensity scan we notice that there is an "off" period which can be seen in Figure 3.18. Again the "on" and "off" states follow the power law distribution confirmed by the log graphs in Figure 3.18.

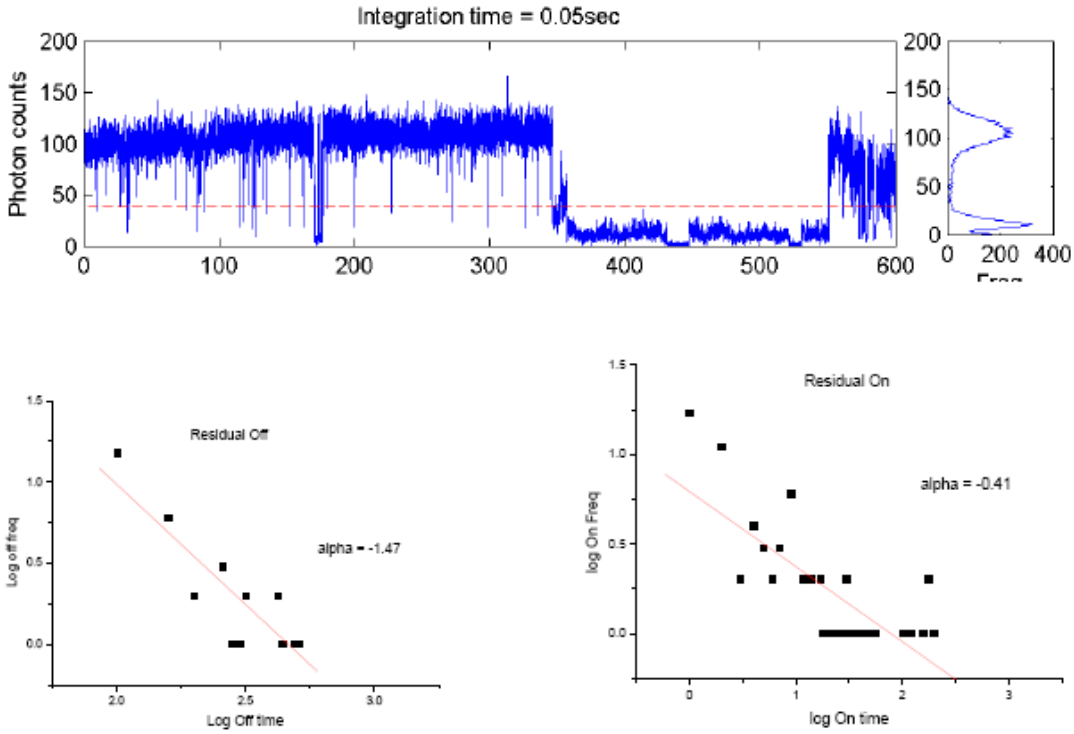

Figure 3.18 Intensity time graph showing the "on" and "off" periods of KP282 whilst under continuous wave excitation rate showing the off power law exponent of -1.47 (left) and on power law of -0.41 (right).

The lifetime measurements of the QDs were then measured. Ideally a single exponential is desired however for this sample a bi exponential is observed only with an initial fast component of 3 ns and a longer tail of 31 ns, which can be seen in Figure 3.19. This could be due to surface defeats caused by aging.

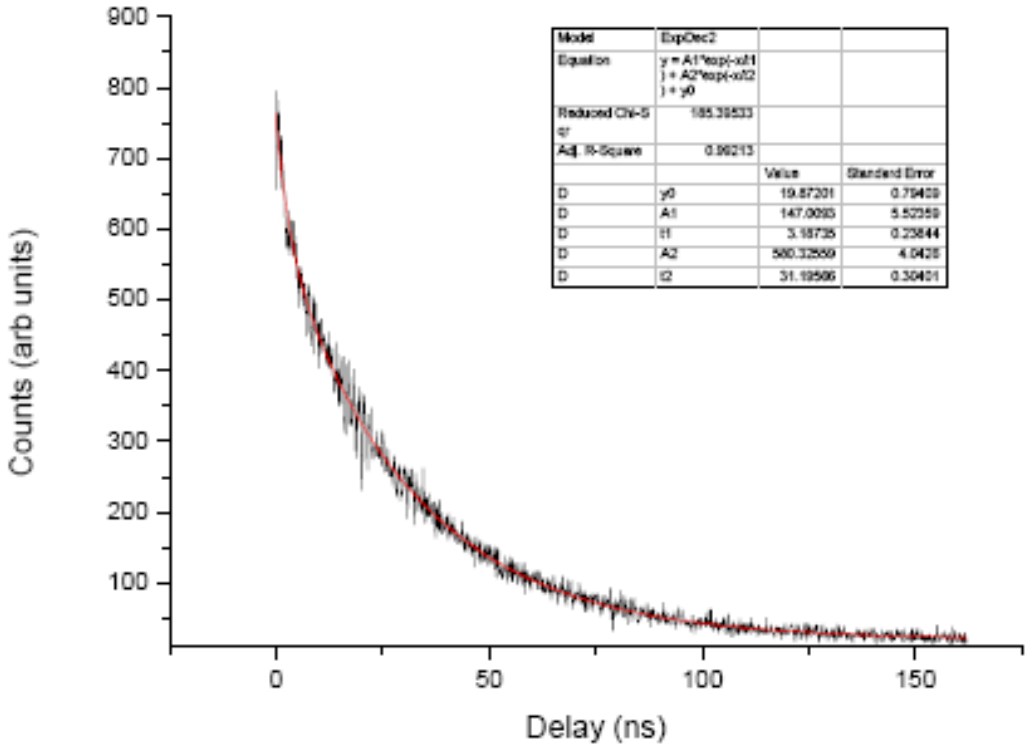

Figure 3.19 Lifetime measurement showing a bi exponential with an initial fast component of 3 ns and longer tail of 31 ns of KP282.

Surface defects are a major reason for a diminished quantum yield and they are also a small subsection of trap sites and it is trap sites that are the cause of blinking. The previous single nanocrystal investigation of a sample of alloyed quantum dots had surface defects caused by aging therefore a shell of ZnS was added to another sample of alloyed QDs. This was to reduce the surface defects and increase the "on" states by reducing the possibility of recombination via trap states. The shell was added using zinc ethylxanthate using the same process of shelling CdSe cores as described in Chapter 2. The spectral data can be seen in Figure 3.20. The sample emits at 612 nm with a FWHM of 12.5 nm.

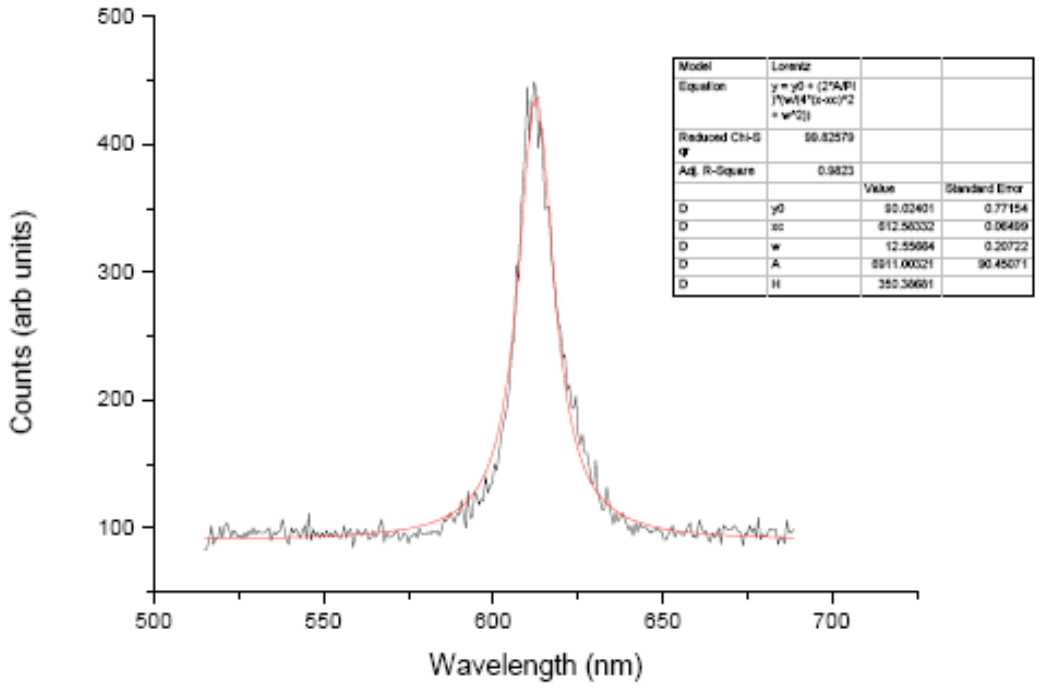

Figure 3.20 Spectral data for alloyed nanocrystals emitting at 612 nm over 0.5 s integration time.

Spectral time traces were taken of four individual nanocrystals from this sample of alloyed QDs and can be seen in Figure 3.21. A spectral drift of 5-8 nm was observed in some cases caused by fluctuations in the local electric field.

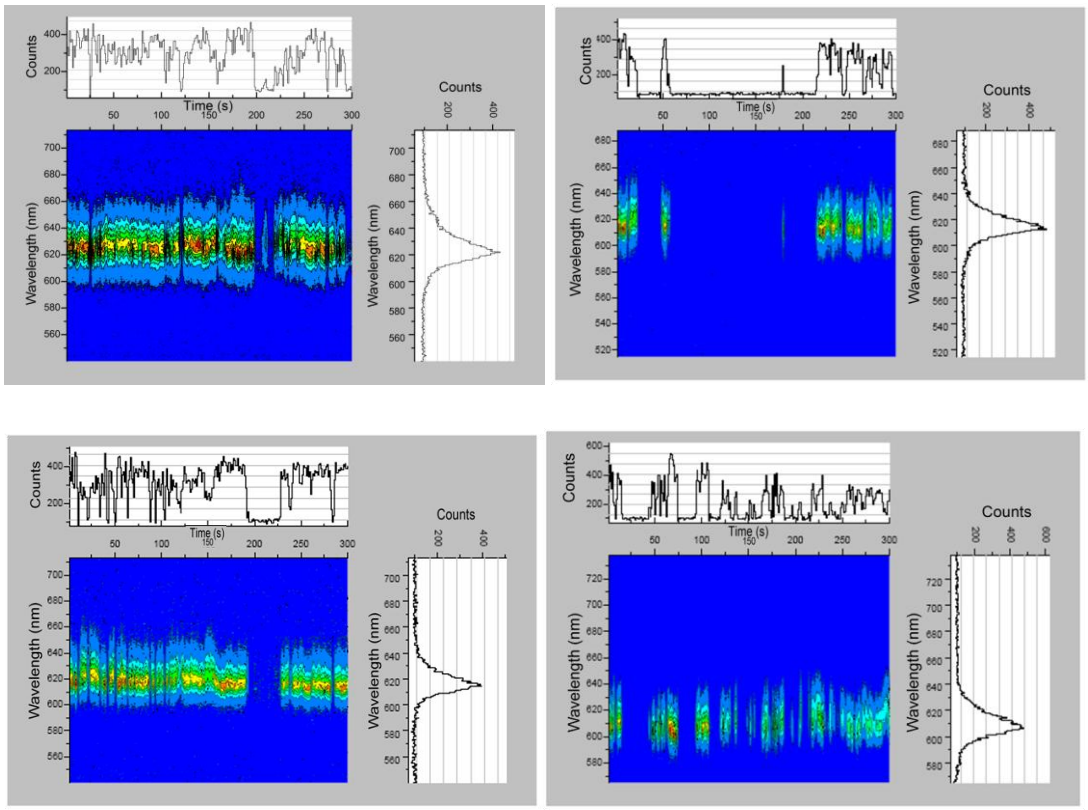

Figure 3.21 Spectral time traces of four individual nanocrystals emitting at 612 nm over 300 spectra with an integration time of 0.5 s.

The blinking investigation showed that the QDs do blink typically on a short time scale. Some nanocrystals behave differently when under pulsed excitation however these QDs behaved in the same manner. Again the QDs follow the power law distribution as seen in Figure 3.22.

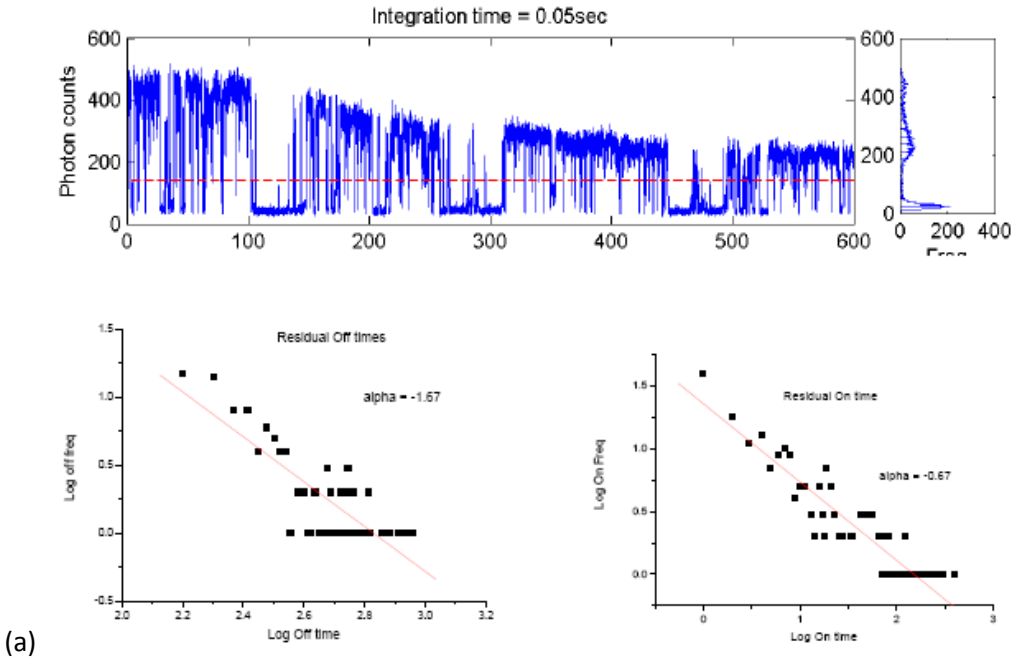

(a)

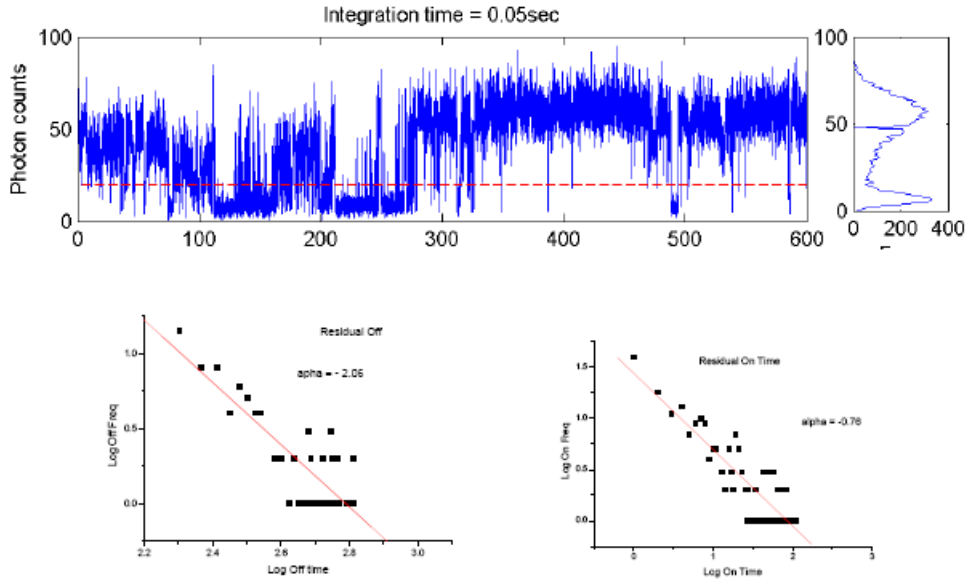

(b)

Figure 3.22 (a) An intensity time graph of alloyed QDs emitting at 612 nm under continuous wave excitation showing the off power law exponential of -2.08 (left) and on power law exponential of -0.79; (b) An intensity time graph of the same QDs emitting at 612 nm under pulsed excitation rate of 5 MHz repetition rate with off power law exponential of -2.08 (left) and on power law exponential of -0.79.

The lifetime measurements for these quantum dots (see Figure 3.23) appears to be an example of single exponential decay. The ZnS shell had a positive effect on the lifetimes of these QDs. A single exponential can model the lifetime at short times but, a tri exponential lifetime is needed to fit all the data. We can therefore ascribe the slight

variations from a single expontential to defects. However the non radiative routes ascribed to defects only have a minor influence on the overall optical behaviour of the nanocrystals. This in comparison to the purely alloyed sample indicates that the main sources of trap sites were at the surface of the alloyed NC. The addition of ZnS passivates most traps sites.

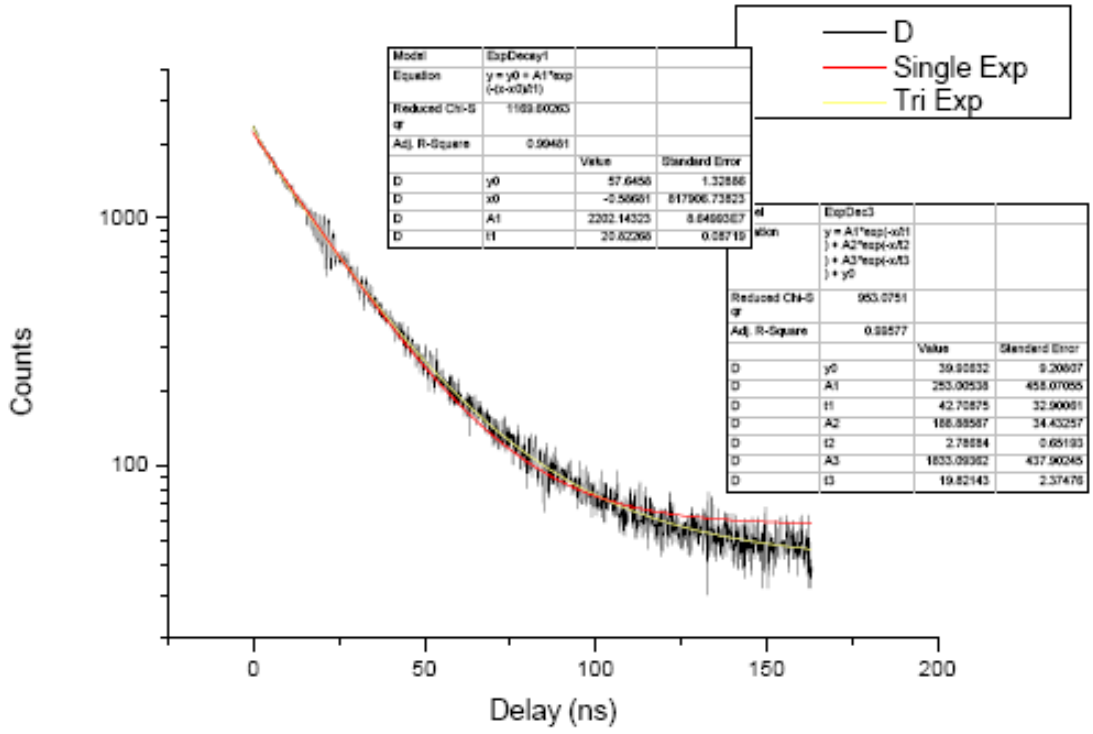

Figure 3.23 Photoluminescence lifetime measurement. The fitting shows a single and tri exponential fittings. The exponential shows a lifetime of (a) single - 20.1 ns, (b) tri – 19.8, 2 and 43 ns.

It can be concluded from this study that the alloyed nanocrystals are very bright and stable emitters. It is known that lifetime and FWHM are related and this data supports this; the larger the FWHM, the shorter the lifetime. The shelled alloy NC had a smaller FWHM but the lifetime was greater than that of the unshelled alloy NC potentially caused by the enhanced confinement by the shell.

3.6 Conclusion

In conclusion, it has been shown that alloyed QDs can be synthesised to emit over the whole visible range with QYs ranging from 7% - 70% depending on the concentration of sulfur or selenium used. These QDs are very stable and can remain luminescent for over a year and a half in dry solvent. Omitting selenium $Zn_xCd_{x-1}S$ QDs emitted in the blue region of the visible spectrum at 400, 426 and 449 nm. By increasing the value of x the QDs decreased in size which was confirmed by TEM. Using cadmium, zinc, sulfur and selenium the QDs synthesised emitted from 390 – 622 nm with high QYs. By changing the concentration of selenium and then sulfur the size of the particles varied, noting that as the concentration of selenium increased the size of the particles increased and so corresponds to why when the concentration of sulfur increased the size of the particles decreased. These results were reproducible, each reaction was carried out at least three times, and each time resulted in QDs that emitted at very similar wavelength and with comparable QYs.

Successful encapsulation of the QDs in thiol-containing microspheres resulted in PL maxima remaining constant, with QYs measuring 23% and 25%; this was reduced to 14% when made aqueous compatible, which is a marked improvement on previous reports. These PVP-QDs could be possibly used for bioimaging and encoding applications.

Successful multiphoton excitation of QDs in toluene may allow these QDs to be suitable for 3D bioimaging as they can be excited at 700 nm, which is a tissue window in the body, as neither water nor haemoglobin absorb in this region. They can also be possibly useful for 3D data storage applications.

Single nanocrystal investigation showed that the larger the FWHM, the smaller the lifetime of NCs; supporting the relation between FWHM and lifetime. The alloys investigated were bright emitters and tended to be in the “on” state rather than the “off” state. These are promising results that can be taken further to synthesise NCs that are non blinking and can be used for biomedical imaging and opto-electronics specifically for biological tagging and single photon sources.

CHAPTER 4 TYPE II AND TYPE II/TYPE I NANOPARTICLES

4.1 Introduction

One of the most common targeting applications for nanoparticles is of chemotherapeutic agents against most cancerous cells and tumour sites. Oral delivery of chemotherapy is of high interest because chemotherapeutic agents are eliminated by the first-pass extraction of the cytochrome P450-dependant metabolic process.[130] Another reason it has attracted attention is due to the phenomenon known as the enhanced permeation and retention (EPR) effect. The vasculature around tumour sites is inherently leaky due to the rapid vascularization necessary to serve fast-growing tumours.[131] Much attention has been given to lymphatic targeting with nanoparticles. In addition, poor lymphatic drainage at the site prevents elimination of the particles from the tumour tissue. Another advantage of tumour targeting is the fact that many cancer cells over-express specific antigens. Coating or binding of ligands on nanoparticulate surfaces can exploit this property.[132] The use of colloidal semiconductor quantum dots (QDs) for biomedical assays and imaging experiments is therefore an area of significant interest as they have advantages over fluorescent dyes currently being used. The idea was introduced a decade ago[133-134] with the realization that QDs tend to be more photochemically efficient than organic dyes. This is due to the compounded effects of extinction coefficients, an order of magnitude larger in QDs (0.5-2 x 10^6 M^{-1} cm^{-1}), than those of most dyes (5-10 x 10^4 M^{-1} cm^{-1}) with comparable QYs and similar emission saturation levels.[135] The absorption rates of the QDs will be 10-50 times faster that those of the organic dyes at the same excitation photon flux. The larger extinction coefficients enable the QDs to appear brighter in photon limited *in vivo* conditions due to scattering and absorption. In theory, the lifetime limited emission rates for single QDs are 5-10 times lower than those of organic dyes, due to their longer excited state lifetimes (20-50 ns).[135] However, in reality the rate of absorption is the main limiting factor of fluorescence emission as fluorescence imaging takes place under absorption limited conditions. QDs therefore appear 10-20 times brighter than organic dyes as their rate of light emission is higher. This observation has been noticed and confirmed by several groups.[136-138]

The advantages of QDs over dyes include their potential resistance to bleaching over long periods of time. Dyes tend to have short lifetimes meaning that it is difficult to get sharp and well contrasted images. The increased photostability of QDs is very useful for three-dimensional optical sectioning. Near infrared (NIR) QDs are a new

generation of QDs which have far reaching potential for the study of intracellular processes at the single-molecule level, high-resolution cellular imaging, long-term *in vivo* observation of cell trafficking, tumour targeting, and diagnostics.[81] Another advantage of using tuneable NIR QDs is the limited choice of organic dyes (Cy7 (767 nm)[139], IRDye78 (796 nm)[140], indocyanine green (784 nm)[141]) that can be used in the biological NIR window. The fluorescence QYs of QDs are higher and have superior photostability when compared to the above dyes.[142]

Currently there are many QD systems which have high QYs in the visible region[143-147] however examples of QYs of NIR region emitting QDs (700 and 1000 nm) are fewer.[148] Type-II QD systems (see section 1.9) aim for a large red shift of emission wavelength with their shell. The band alignment is staggered, unlike type-I QDs where the band gap of the shell is larger than the core. This therefore, causes a smaller effective band gap than each one of the constituting core and shell materials with the natural valence-band offset (ΔE_v) calculated as 0.57 eV.[149] Bawendi's group started much of the work in this area in the NIR region. They have reported type-II QD photoluminescence (PL) QYs for CdTe/CdSe core/shell QDs less than 4%.[150] This was raised to 20% when a further shell of ZnTe was added. There is interest in NIR QDs as they can be applied to improve methods for early tumour detection. The window is good for *in vivo* imaging because of minimal light absorption by haemoglobin (<650 nm) and water (>900 nm) illustrated in Figure 4.1.[151] Other type-II systems which have been studied include CdTe/CdSe,[152-153] InAs/ZnSe,[154] Cd(Hg)Te/ZnS,[155] and ZnTe/CdSe.[156]

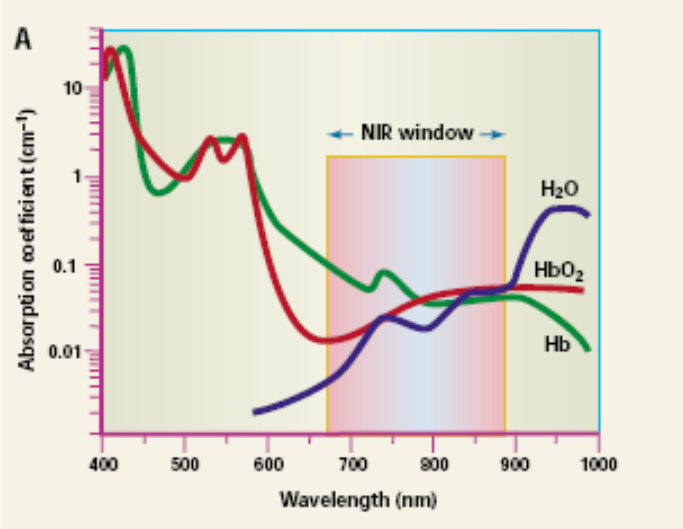

Figure 4.1 The NIR window is good for *in vivo* imaging because of minimal light absorption by haemoglobin (<650 nm) and water (>900 nm).[156]

4.2 Results and Discussion - CdSe/CdTe/CdS Nanoparticles

4.2.1 Synthesis of 3.5 nm CdSe Nanoparticles

The CdSe nanoparticles had a diameter of 3.5 nm and were grown by means of high temperature colloidal synthesis using cadmium oxide as a starting material, rather than pyrophoric organometallic compounds, in oleic acid and ODE. The luminescence spectrum is shown in Figure 4.2. The PL spectrum shows that the nanoparticles emit at 538 nm and the QY was measured to be 12%.

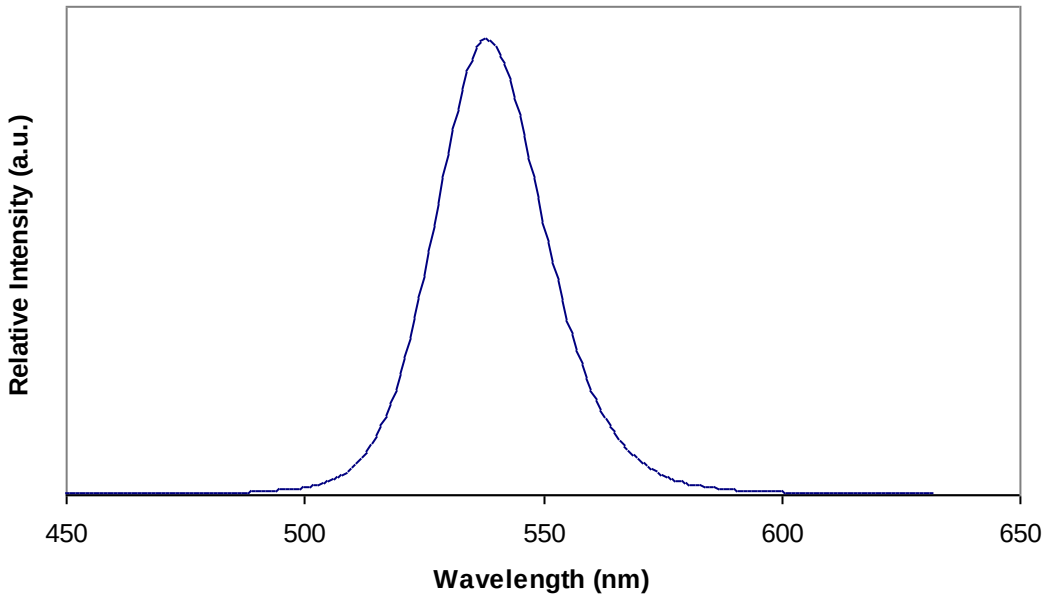

Figure 4.2 PL spectrum of CdSe nanoparticles emitting at 538 nm which was excited at 480 nm.

The pXRD pattern of the CdSe nanoparticles is shown in Figure 4.3. Strong reflections are shown to the (002), (110), (103) and (200) lattice planes of hexagonal bulk CdSe (JCPDS 08-0459).

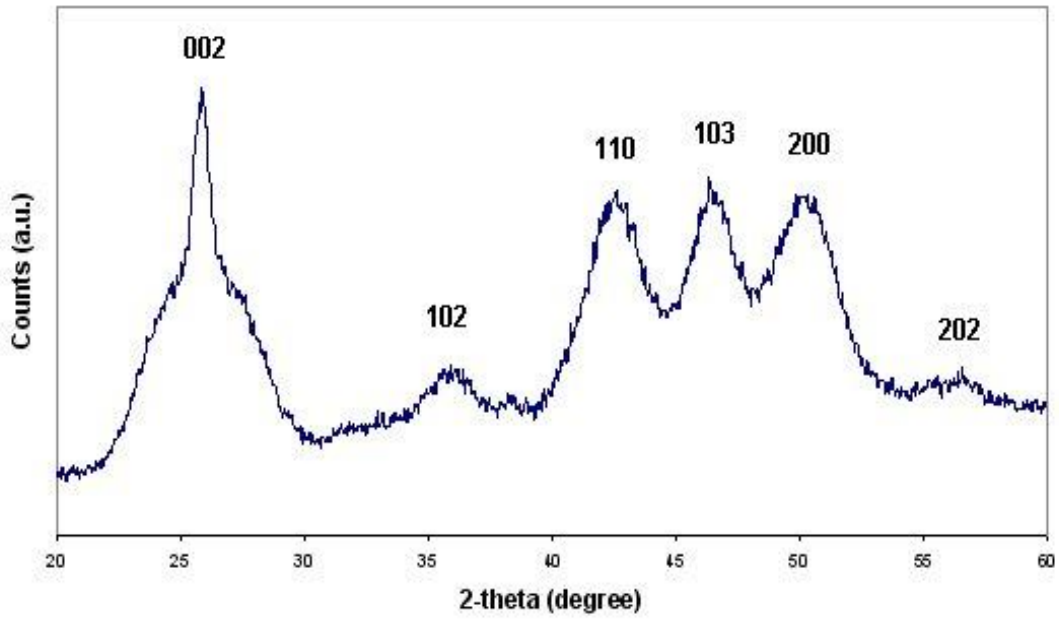

Figure 4.3 pXRD pattern of CdSe nanoparticles showing strong reflections for (002), (110), (103) and (200).

Figure 4.4 show the TEM image of CdSe nanoparticles. The size of the particles was measured to be 3.5 nm.

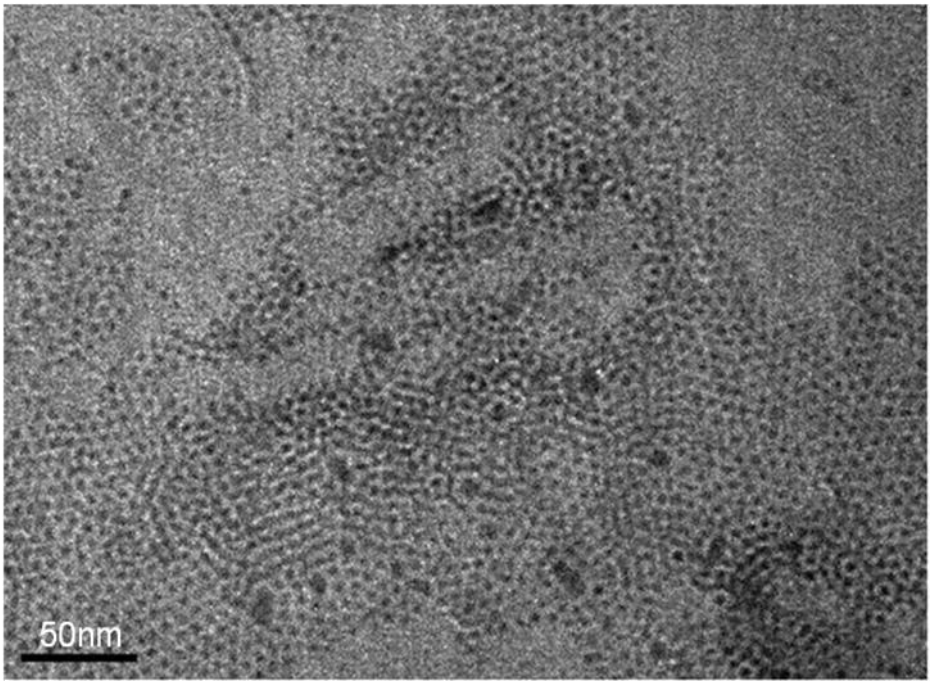

Figure 4.4 TEM image of 3.5 nm CdSe nanoparticles (scale bar = 50 nm).

4.2.2 Synthesis of CdSe/CdTe/CdS Nanoparticles

The synthesis of CdSe/CdTe/CdS type-II/type-I QDs emitting in the NIR included the previously synthesised CdSe as the core, which is then shelled with CdTe followed by a high band gap CdS shell. These QDs were synthesised in a two step high temperature colloidal process. The lattice mismatch between each stage is relatively small ~7% and 10% respectively, causing lattice strain to be minimal.

In a typical synthesis using CdSe as a core, the CdTe shell was grown using both the cadmium and tellurium precursor which were added separately. Cadmium oxide in oleic acid and ODE was added slowly dropwise at a high temperature, followed by the addition of tellurium in TBP and ODE dropwise after a 5 min interval. It was important to add the precursors slowly and at an even pace to ensure even shelling and to prevent the growth of isolated CdTe nanoparticles which could occur if the solution was added too quickly. A growth time of 30 min was given before the addition of the final shell. The final shell was added by the slow addition of a CdS precursor $[Cd\{S_2CNMe(Hex)\}_2]$ in TBP and ODE. The TGA (under N_2, 10 ^{o}C/min) of $[Cd\{S_2CNMe(Hex)\}_2]$, Figure 4.5, showed that it decomposes at 357 ^{o}C in a single-step leaving ~29% residue which corresponds well with bulk CdS (cal. 29%) therefore making it an ideal precursor for CdS.[157]

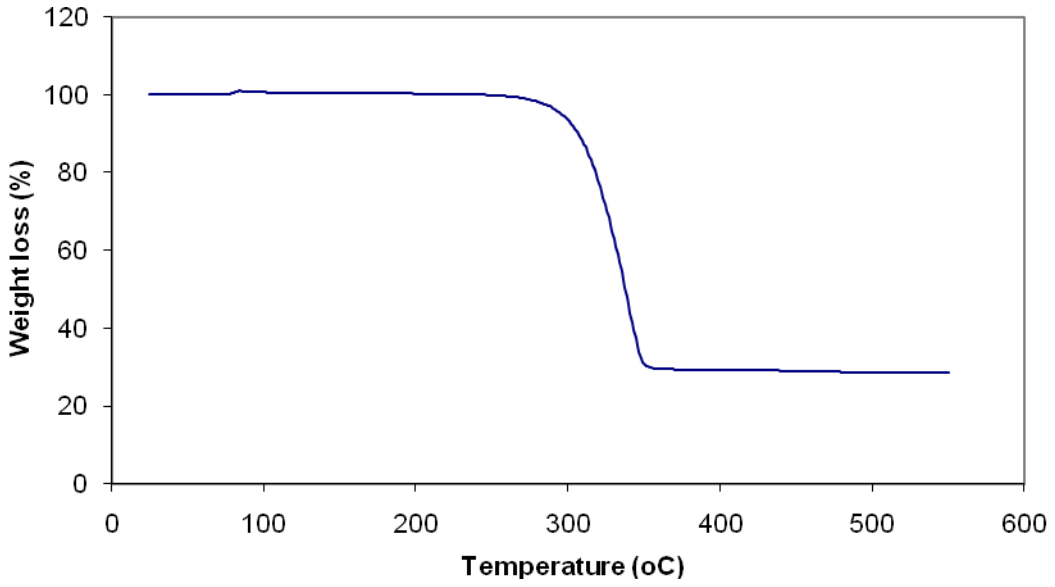

Figure 4.5 TGA (under N_2, 10 ^{o}C/min) of $[Cd\{S_2CNMe(Hex)\}_2]$ which decomposes at 357 ^{o}C leaving 29% residue corresponding with bulk CdS (cal. 29%).

Figure 4.6 shows the emission spectra for CdSe/CdTe and CdSe/CdTe/CdS. A red shift was observed as the QDs increase in size. The CdSe core emits at 538 nm which sees a red shift of ~140 nm with the addition of CdTe shell as the emission wavelength increased to 674 nm. Due to tellurium's instability in air, the additional shell of the CdS shell was then added *in situ* to retain photoluminescence. A red shift of ~80 nm was observed with the addition of the final shell pushing it into the NIR region emitting at 754 nm. The QY of the original core was 12% which increased to 29% with the addition of the CdTe shell. This then rose further to 48% upon the addition of the CdS shell.

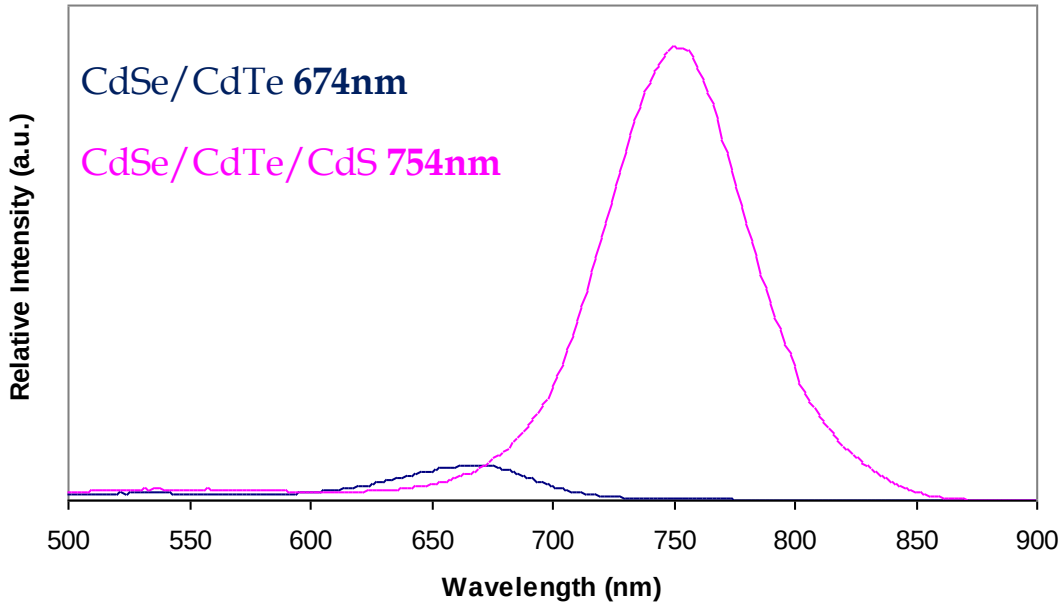

Figure 4.6 PL spectra of CdSe/CdTe and CdSe/CdTe/CdS which were both excited at 480 nm.

The addition of only one CdTe shell was determined to be optimum, as previous experiments had shown how the monodispersity of the dots was affected upon the addition of the second shell. Figure 4.7 shows how, with the addition of one shell the peak remains uniform, but after the addition of the second shell the peak develops a shoulder. Although it is seen that the emission peak of the final product is uniform once again, this intermediate stage will undoubtedly have detrimental effects on the overall photoluminescence. The peaks in this spectrum are not all comparable, however the two peaks at 742 nm are and they show the drop in intensity of the final product after being left in toluene overnight, therefore showing the importance of storing the QDs under nitrogen.

By having a thin CdTe shell it was initially unknown if the final product would emit in the NIR region but as we can see in Figure 4.6 the final product does also emit in this region.

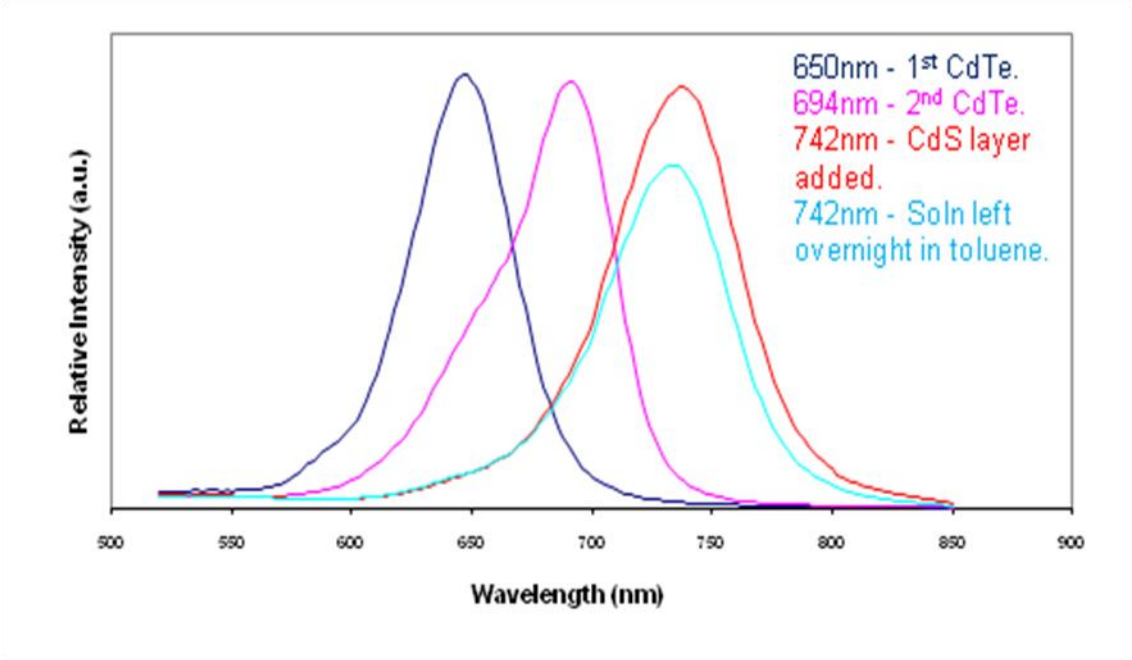

Figure 4.7 PL spectra of CdSe/CdTe with a single CdTe layer, CdSe/CdTe with a double CdTe layer, CdSe/CdTe/CdS and CdSe/CdTe/CdS when left overnight in toluene which were all excited at 480 nm.

The QY increases on shelling with CdTe and again on shelling with CdS with the overall stability increasing also. This is shown by measuring the QY after initial synthesis and again after a period of 8 weeks stored in dry chloroform under nitrogen. The QY over this period decreased from 48% to 22% which showed that the QDs are relatively stable.

To characterize the material it was analyzed by powder XRD. The CdSe core with CdTe and CdS shell was compared with the diffraction pattern of bulk cubic CdTe shown in Figure 4.8. The main peaks for bulk CdTe are at 29.42°, 37.14° and 63.50°, however the pXRD pattern shows only the pattern expected for glass. This is because the product must have decomposed before analysis was achieved.

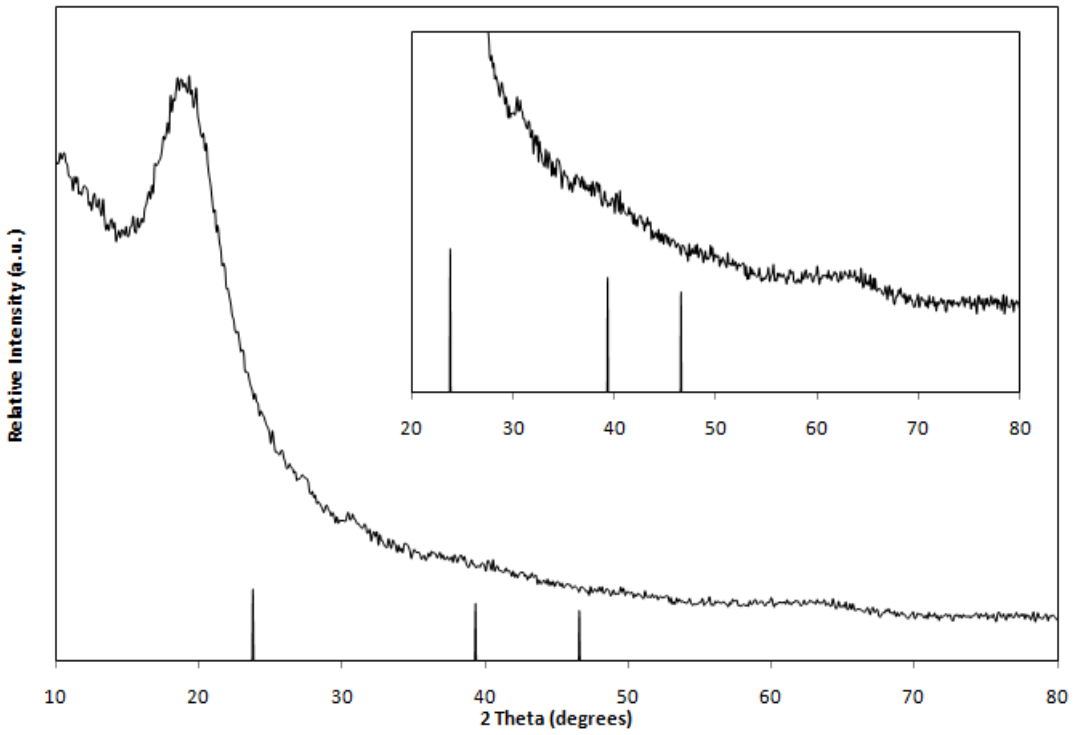

Figure 4.8 pXRD pattern from CdSe/CdTe/CdS with standard diffraction lines of bulk cubic CdTe.

By utilizing both type I and type II interfaces, the possibility of synthesising QDs in the NIR region which are also stable is increased. The type II interface as the CdSe core is shelled with CdTe causes a large red shift towards the NIR region. Generally type I interfaces result in only a small red shift but in general increase overall stability. This is utilized by shelling CdTe with CdS to serve as a type I heterojunction, with the CdTe layer ensuring the confinement of both photogenerated electrons and holes within the CdSe/CdTe structure, thus substantially enhancing the spatial indirect radiative recombination at the CdSe core and inner CdTe shell interface. This is because CdS has a wide bulk bandgap, 2.42 eV, in comparison with CdSe (1.70 eV) and CdTe (1.56 eV).[158]

The TEM images shown in Figure 4.9 show the CdSe/CdTe/CdS QDs which are approx. 7 nm in size.

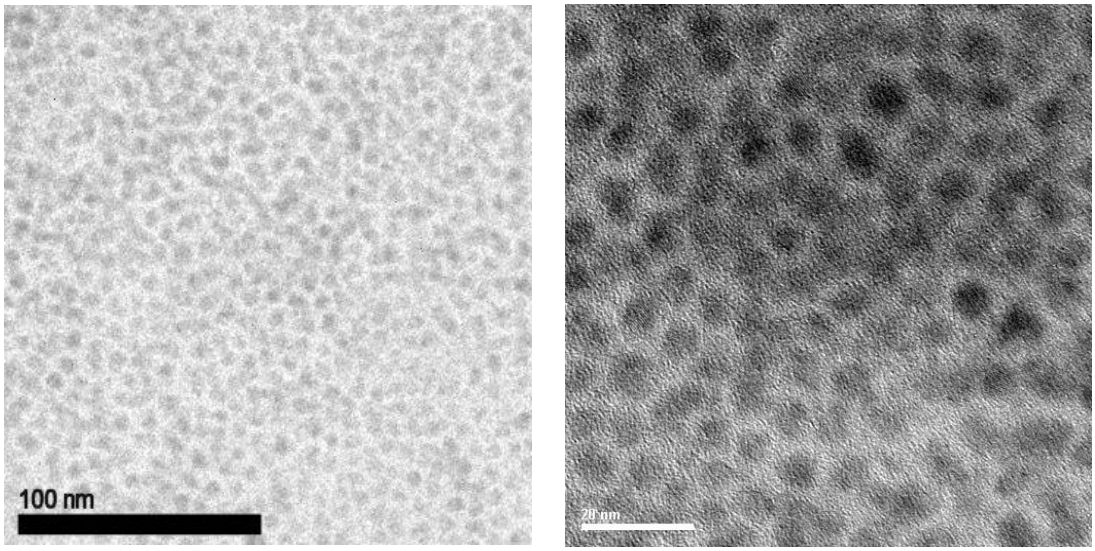

(a) **(b)**

Figure 4.9 (a) TEM image of CdSe/CdTe/CdS QDs (scale bar = 100 nm) ~7 nm in size. (b) TEM image of CdSe/CdTe/CdS QDs (scale bar = 20 nm).

4.2.3 Synthesis of 4.5 nm CdSe Nanoparticles

The CdSe nanoparticles synthesised were larger than the previous ones described in this chapter as their diameter was 4.5 nm. They were also synthesised by high temperature colloidal synthesis using cadmium oxide in oleic acid and ODE. Generally, in these experiments TOPSe solutions were injected quickly in the cadmium solution; however the reverse happened here where the cadmium solution was injected into a TOPSe/oleylamine mixture. Figure 4.10 shows the PL and UV-Vis spectrum of the CdSe nanoparticles synthesised which emit at 644 nm and the QY measured was 11%.

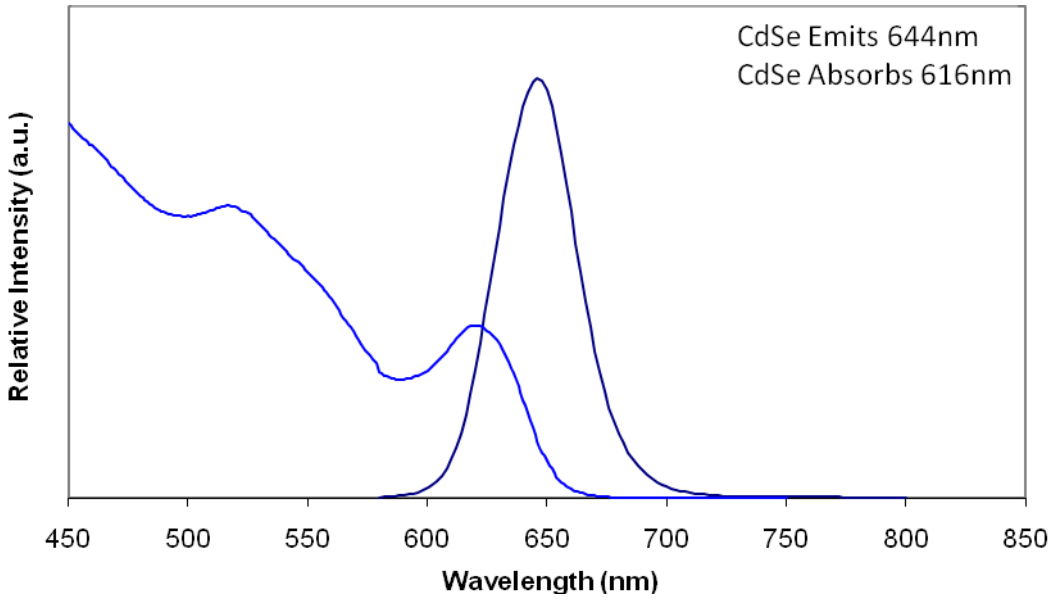

Figure 4.10 PL and absorption spectra of CdSe nanoparticles emitting at 644 nm (which was excited at 480 nm) and absorbing at 616 nm.

The TEM image of CdSe nanoparticles is shown in Figure 4.11 and it was using the image that the diameter was measured to be 4.5 nm.

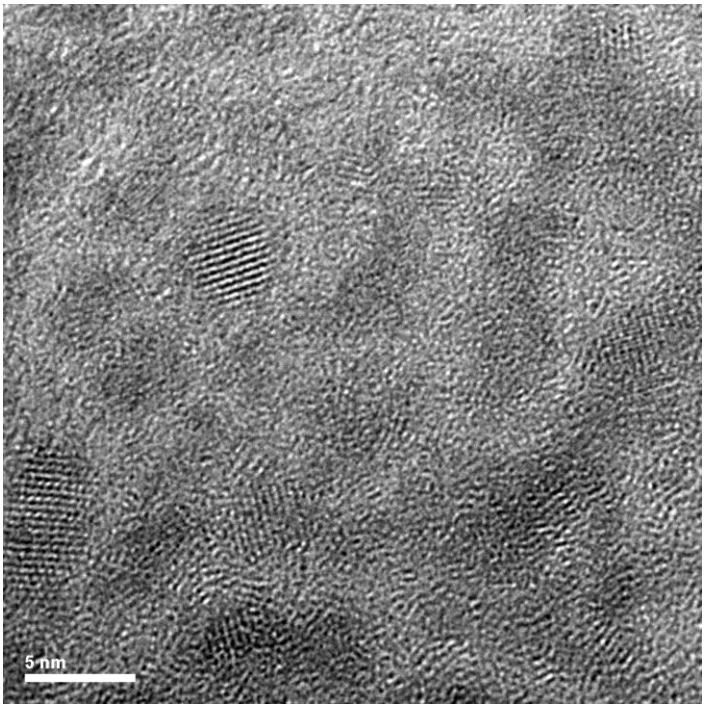

Figure 4.11 TEM image of 4.5 nm CdSe nanoparticles (scale bar = 5 nm).

4.2.4 Synthesis of CdSe/CdS Nanoparticles

To synthesise CdSe/CdS nanoparticles the same CdS precursor was used, $[Cd\{S_2CNMe(Hex)\}_2]$. Using the 4.5 nm CdSe previously synthesised they were added to oleic acid and ODE and heated to 250 ^{o}C where the CdS precursor was slowly added and allowed to anneal for 30 min. Figure 4.12 shows the PL and absorption spectra for both the CdSe core and CdSe/CdS nanoparticles. The shelled nanoparticles emit at 654 nm, meaning that a 10 nm red shift has occurred. The QY was in this case unaffected by the addition of the CdS shell as it remained at 11%.

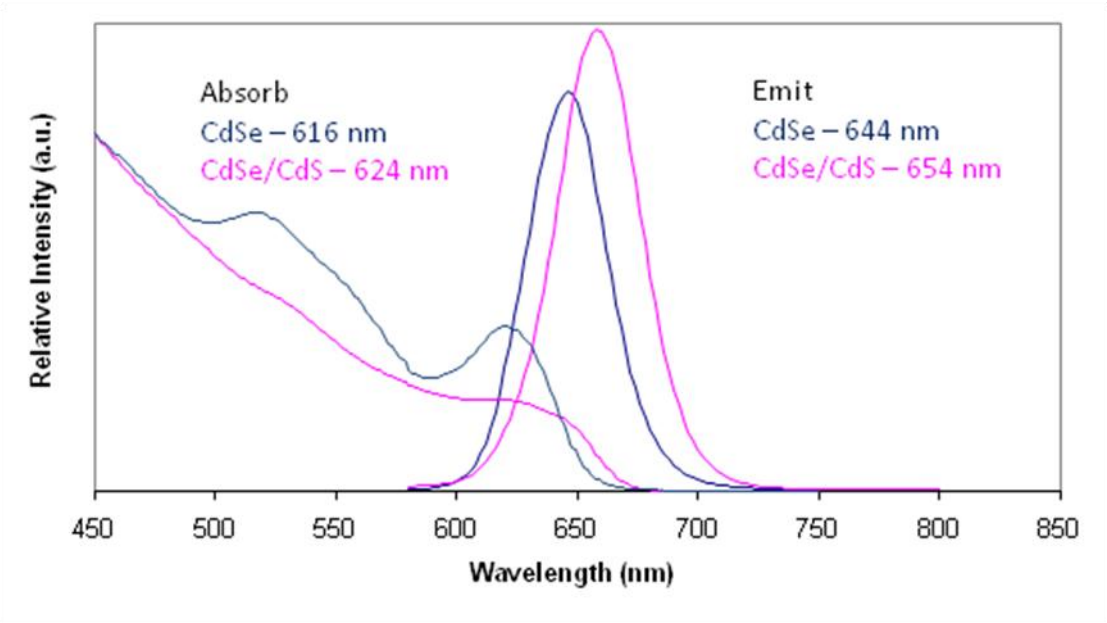

Figure 4.12 PL and absorption spectra of CdSe QDs which absorbed at 616 nm and emitted at 644 nm. The CdSe/CdS QDs absorbed at 624 nm and emitted at 654 nm. The PL samples were all excited at 480 nm.

The TEM image of CdSe/CdS nanoparticles is shown in Figure 4.13 and the particles were determined to be 5.5 nm.

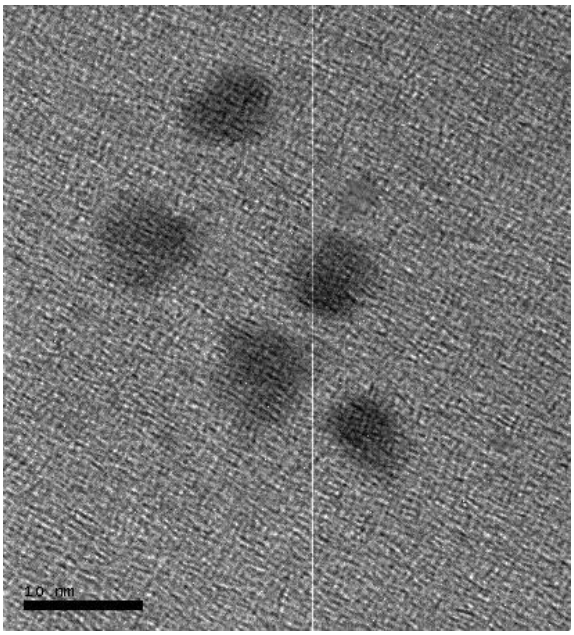

Figure 4.13 TEM image of CdSe/CdS nanoparticles measuring 5.5 nm in diameter (scale bar = 10 nm).

4.2.5 Comparison of Type I and Type II/Type I PL transient decays

The PL transients of CdSe/CdS and CdSe/CdTe/CdS were measured by Stuart Stubbs from D. Binks' group. The purpose of this was to see the difference a type II interface makes to lifetime of these nanoparticles. It was essential that the nanoparticles synthesised emitted over 624 nm. The is because for multi exciton generation the lowest pump wavelength the laser can go to is 240 nm so as to exceed the MEG threshold the band gap needs to be 2.6 times larger. It was for this reason the CdSe nanoparticles synthesised for CdSe/CdS were prepared via a different method (see section 4.2.3) in order to ensure that they would emit over this threshold.

The PL peak for the type I dots was at 660 nm therefore the fluorescence lifetimes were monitored to 660 nm. The laser pulse period was set to 2 μs as this was more than x 5 the time it took for the decay to relax to the background level. A good fit was found when 2 exponentials are used to describe the decay with the following results:

	Relative fluorescence intensity
τ_1 = 32 ns	84.79%
τ_2 = 6 ns	15.21%

This serves to show that processes other than radiative recombination occur within the dot such as recombination at trap sites. Figure 4.14 shows the graph of TCSPC on type I CdSe/CdS quantum dots.

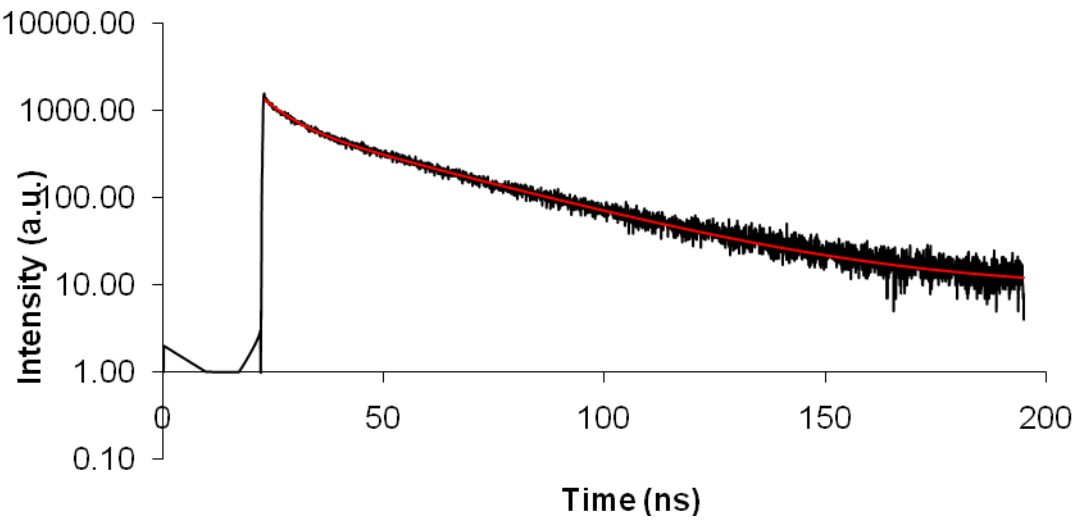

Figure 4.14 TCSPC on Type I CdSe/CdS nanoparticles with the red line showing the lifetime which was the best fit to the data.

The PL peak for CdSe/CdTe/CdS was found to be at ~730 nm, therefore the fluorescence lifetimes was monitored at 730 nm. The laser pulse period was set to 2 μs as this was more than x 5 the time it took for the decay to relax to the background level. A reasonable fit was found when 2 exponentials are used to describe the decay with the following results:

	Relative fluorescence intensity
τ_1 = 41.3 ns	87.2%
τ_2 = 4.3 ns	12.8%

In this dot there are clearly other processes occurring and as the PL was so weak in this dot it was quite hard to get a decay. For dots with high quantum yields where radiative recombination dominates we often obtain single exponential lifetimes and when viewed on a log plot appear as straight lines. Figure 4.15 shows the graph of TCSPC on type II/type I CdSe/CdTe/CdS quantum dots. In both dots here we do not see this, revealing other competing processes.

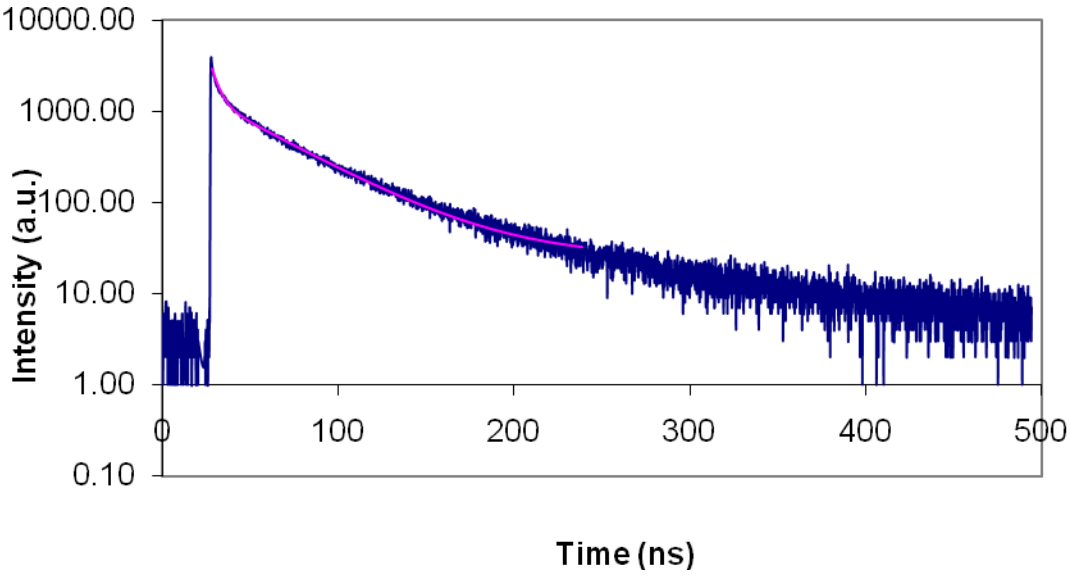

Figure 4.15 TCSPC on Type II/Type I CdSe/CdTe/CdS nanoparticles where the red line is showing the lifetime which was the best fit to the data.

It is possible that in the type II/type I quantum dots we are creating tri-exictons at laser powers that usually only create bi-exitons in other quantum dots. Along with the lifetime data and the relatively unexplored area of the behaviour of multi-exitons type II quantum dots could have important implications for the use of dots in solar cells.

4.3 CdTe/CdSe/CdS NIR Nanoparticles

4.3.1 Synthesis of CdTe Nanoparticles

The synthesis of CdTe was carried out using cadmium oxide with ODPA in ODE. Tellurium powder was separately dissolved in TBP and ODE which was rapidly injected into the cadmium solution. The reaction time was 1.5 h with aliquots taken regularly. To see if this was the extent of growth possible, the reaction time was extended to 17.5 h. Figure 4.16 shows the normalised PL spectra over 45 min. After 45 min there has been a red shift of 46 nm but the peak has begun to broaden.

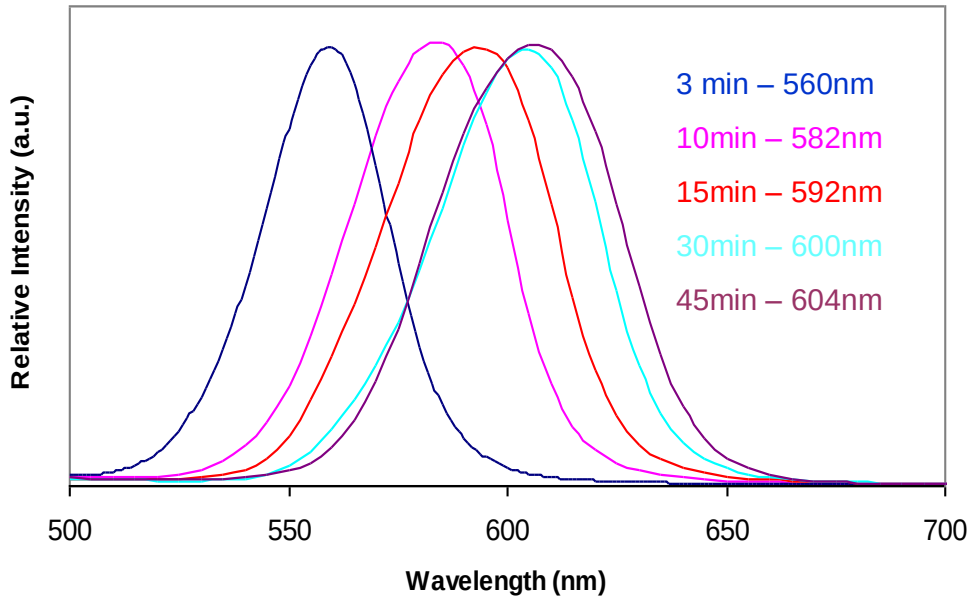

Figure 4.16 Normalised PL spectra of CdTe nanoparticles after 3 min, 10 min, 15 min, 30 min and 45 min reaction time which were all excited at 480 nm.

After 1.5 h the peak continue to red shift but it becomes broader still and develops a shoulder. Regardless the reaction was then left overnight and stopped after 17.5 h to see the result. Figure 4.17 shows the normalised PL spectra of the reaction after 1 h and 1.5 h and a 10 nm red shift is observed between the two aliquots. When the reaction was stopped the PL was measured and the sample emitted at 668 nm, however the peak was very broad meaning that the luminescence had dramatically decreased.

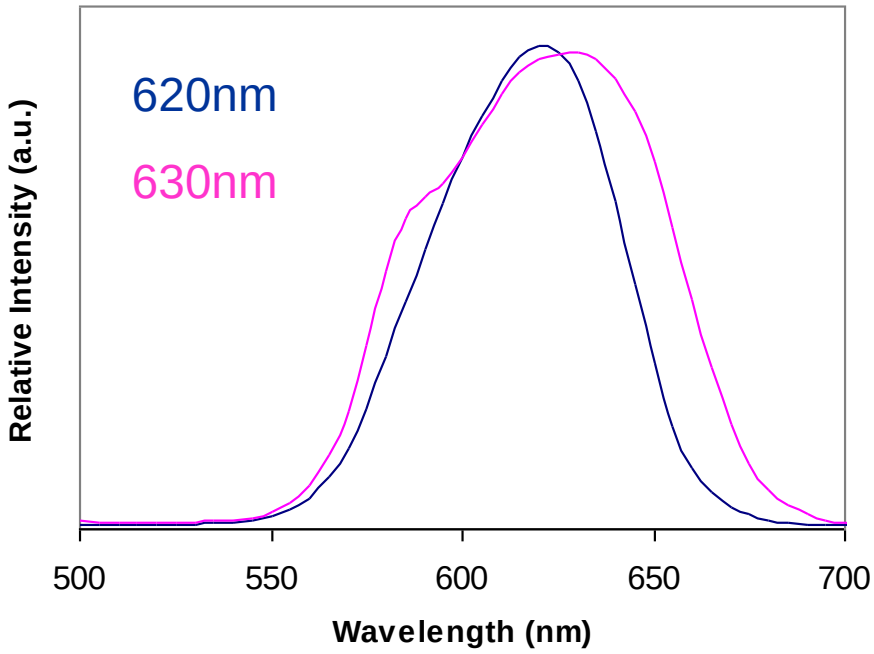

Figure 4.18 Normalised PL of CdTe nanoparticles after 1 h and 1.5 h reaction time and was excited at 480 nm.

The reaction was repeated and stopped immediately after injection to produce CdTe nanoparticles which emitted at 565 nm. These were then taken on to be shelled with CdSe. However, despite numerous attempts a successful method was not found to maintain luminescence. This is due to the CdTe QDs being prone to oxidation which leads to low QY and fast photobleaching.[159] The growth of a protective inorganic shell around CdTe QDs is therefore of importance. However if the CdTe QDs oxidise during the isolation process then there are bound to be large surface traps which the addition of the CdSe shell would be unable to remove. Therefore, we moved onto synthesising CdTe/CdSe *in situ*.

4.3.2 Synthesis of CdTe/CdSe Nanoparticles *in situ*

The synthesis of type II quantum dots CdTe/CdSe emitting in the far red to NIR required the CdTe core being synthesised and then shelled immediately with CdSe before isolation. The *in situ* growth of these core/shell, CdTe/CdSe, QDs is necessary to produce high QYs due to CdTe's air sensitive nature. The CdSe shell helps shield it from the atmosphere, therefore stabilizing the final product. The lattice mismatch is ~6% meaning that the strain should not be too great. 8 mg of selenium was initially used for the

synthesis of CdTe/CdSe and this resulted in QDs that emitted at 716 nm after a reaction time of 15 min which after 2 h had red shifted 5 nm to 721 nm. Although, we had successfully synthesised QDs emitting in the NIR region the QY was measured to be only 13%. The normalised PL spectra of the CdTe/CdSe QDs are seen in Figure 4.18.

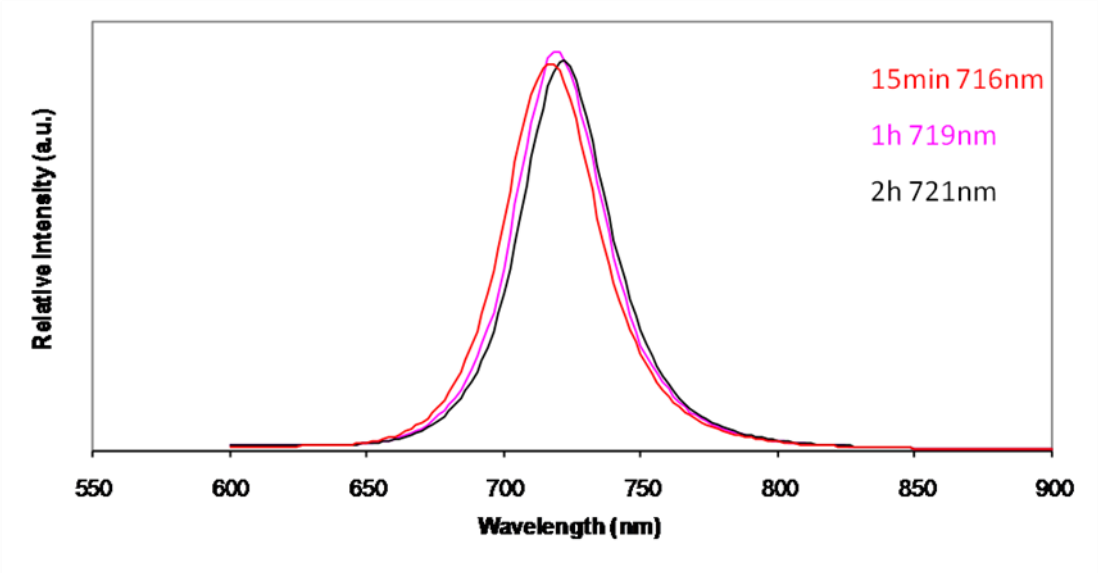

Figure 4.18 Normalised PL spectra of CdTe/CdSe nanoparticles corresponding to 15 min, 1 h and 2 h reaction time using 8 mg of selenium. Each sample was excited at 480 nm.

The TEM image is shown in Figure 4.19. It shows monodispersed CdTe/CdSe QDs which are 5.5 nm in diameter.

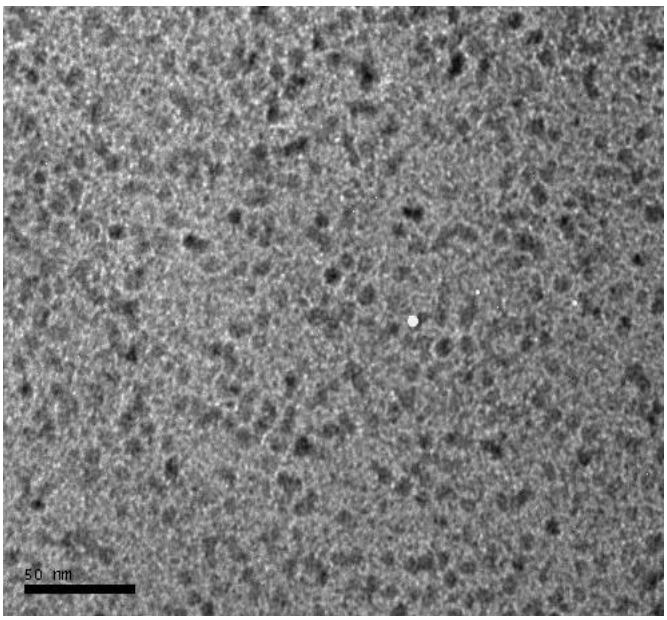

Figure 4.19 TEM image of CdTe/CdSe nanoparticles using 8 mg of selenium (scale bar = 50 nm) 5.5 nm in size.

As selenium concentrations have had dramatic effects in previous experiments (see previous chapter) it was decided to try halving the amount and also increasing the concentration of selenium used. The normalised PL spectrum shown in Figure 4.20(a) shows how the CdTe/CdSe QDs synthesised using 4 mg of selenium red shifting 10 nm as the growth time is increased from 15 min to 2 h. When 4 mg of selenium was used the QDs synthesised were smaller than those made when using 8 mg of selenium as they emitted over a range of 684 to 694 nm. However, when we look at Figure 4.20(b), which is the normalised PL spectra of CdTe/CdSe when 14 mg of selenium was used, it is clear that the selenium concentration does not have any effect in this case on the size of the QDs grown as they emit at approximately the wavelength of 720 nm. Therefore increasing the amount of selenium above 8 mg has no effect on the size and quality of the QDs synthesised.

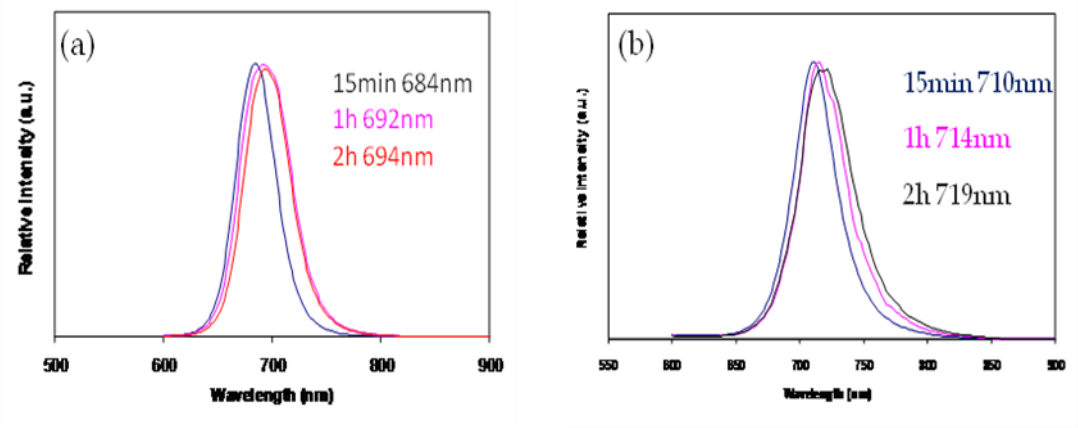

Figure 4.20 (a) Normalised PL spectra of CdTe/CdSe corresponding to 15 min, 1 h and 2 h reaction time using 4 mg of selenium. (b) Normalised PL spectra of CdTe/CdSe corresponding to 15 min, 1 h and 2 h reaction time using 14 mg of selenium. All samples were excited at 480 nm.

The QY of CdTe/CdSe using 4 mg of selenium emitting at 684 nm and growth time of 15 min was measured to be 44%. However, the QY of CdTe/CdSe using 14 mg of selenium emitting at 719 nm and growth time of 2 h was measured to be 12%. It was concluded from these results that the QY decreases as the growth time is increased. Figure 4.21 shows the TEM images of the two different monodispersed CdTe/CdSe samples. CdTe/CdSe using 4 mg of selenium emitting at 684 nm were measured to be 5 nm in diameter and CdTe/CdSe using 14 mg of selenium emitting 719 nm were measured to be 6 nm in diameter.

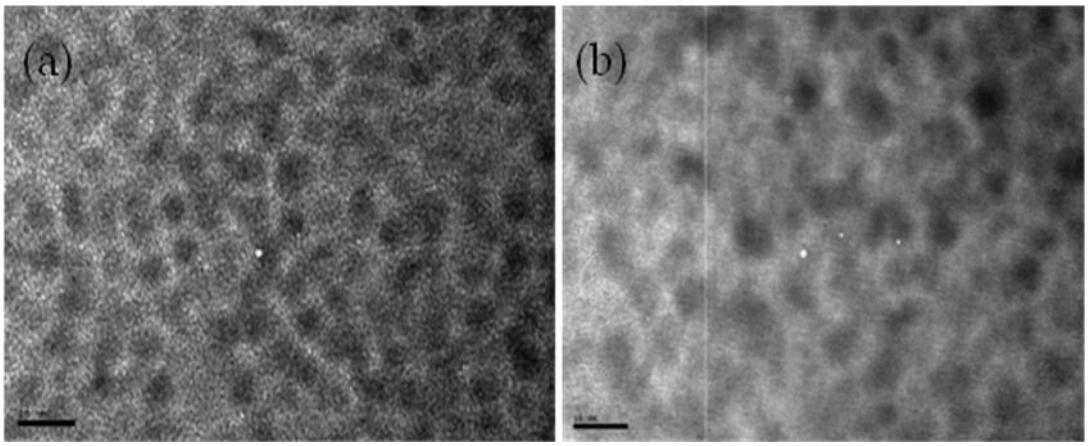

Figure 4.21 (a) TEM image of CdTe/CdSe using 4 mg of selenium (scale bar = 10 nm) 5 nm in size. (b) TEM image of CdTe/CdSe using 14 mg of selenium (scale bar = 10 nm) 6 nm.

It was decided to return to using 8 mg of selenium but replace TOP with TOPO to see the effects. It was expected that the reaction would not work well if at all due to the original synthetic procedure requiring the oxygen present to be removed and replaced with an inert gas. However, we successfully synthesised CdTe/CdSe QDs. The normalised PL spectra, shown in Figure 4.22, shows that QDs emitting at 738 nm were synthesised but monodispersity was not achieved. As the peak is not uniform it is assumed that the QY was low. The QDs synthesised were larger than previous CdTe/CdSe QDs synthesised but with a lower QY they are not viable.

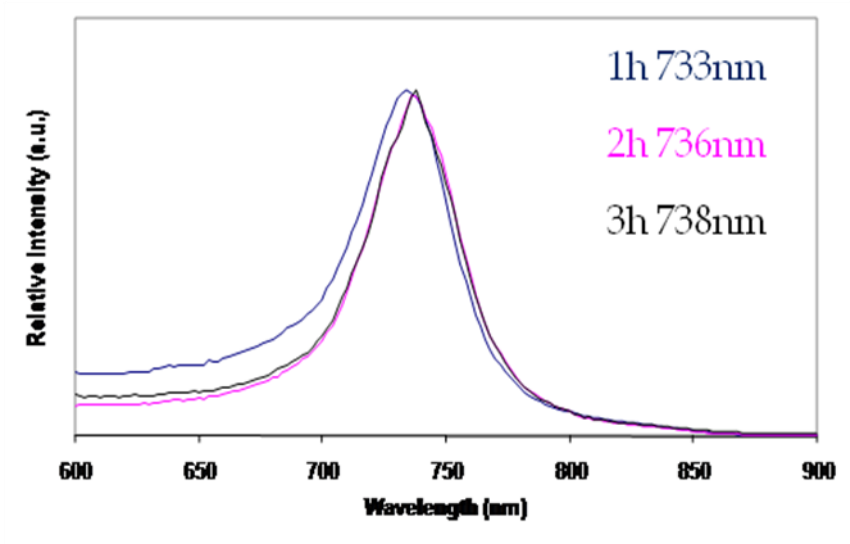

Figure 4.22 Normalised PL spectra of CdTe/CdSe when TOP was replaced with TOPO which was excited at 480 nm and with reaction times of 1 h, 2 h and 3 h.

4.3.3 Synthesis of CdTe/CdSe/CdS Nanoparticles

The synthesis of CdTe/CdSe/CdS type-II/type-I quantum dots emitting in the NIR included a CdTe core which was shelled with CdSe followed by a high band gap CdS shell. These heterostructures were grown by means of single-pot, high-temperature colloidal synthesis and also does not involve highly toxic and pyrophoric organometallic compounds such as dimethyl cadmium. The lattice mismatch between each stage is relatively small, ~6% and ~4% respectively, meaning strain between the layers is less than that observed for CdSe/CdTe/CdS QDs previously synthesised.

CdTe QDs were synthesized using trioctylphosphine (TOP)-Cd and TOP-Te precursors. In a typical synthesis TOP-Te was injected very quickly into a TOP-Cd solution at high temperature. The CdTe QDs were not isolated before being shelled with CdSe due to its air sensitive nature. Earlier experiments indicated that the optimum injection period for CdSe is 1 h followed by growth for 15 min. The QY of the CdTe/CdSe QDs decreased from 44% (15 min) to 13% after 2 h. The red shift observed was small (~5 nm) as the growth time was increased from 15 min to 2 h (Figure 4.19). Earlier experiments carried out determined that successful shelling occurred when the stock solution of TOP-Se was injected slowly over 1 h as the temperature was slowly increased to the growth temperature. A syringe pump was used to ensure the solution was added at a steady rate. This procedure is important because if TOP-Se was added too fast or at an uneven pace then shelling would not occur and potentially isolated CdSe nanoparticles could form in the solution. When CdTe is shelled with CdSe the red shift is minimal, increasing from 688 nm to 694 nm, as the peak remains symmetrical and sharp meaning that monodispersity has been retained and shelling has been successful. If shelling had been unsuccessful this peak would emit in the same place and a second peak might also be visible in the blue or green region, a result of CdSe QDs being also present. A higher PL efficiency is noted with a thinner CdSe shell as it ensured a better overlap of the hole and electron wave function. Thermal decomposition by the slow addition of a CdS precursor [Cd{S_2CNMe(Hex)}$_2$] in TBP and degassed ODE at 250 ^{o}C enables the growth of the final shell.

Figure 4.23 shows absorption and emission spectra for CdTe, CdTe/CdSe and CdTe/CdSe/CdS. A red shift is observed as the QDs increase in size. The shift is small between CdTe and CdTe/CdSe but the addition of the final shell induces a significant red shift of ~60 nm as the emission wavelength is increased from 694 nm to 757 nm, effectively pushing it into the NIR region. As mentioned earlier, the QY increases

during the first stage however it decreases to 35% once shelled with CdS.

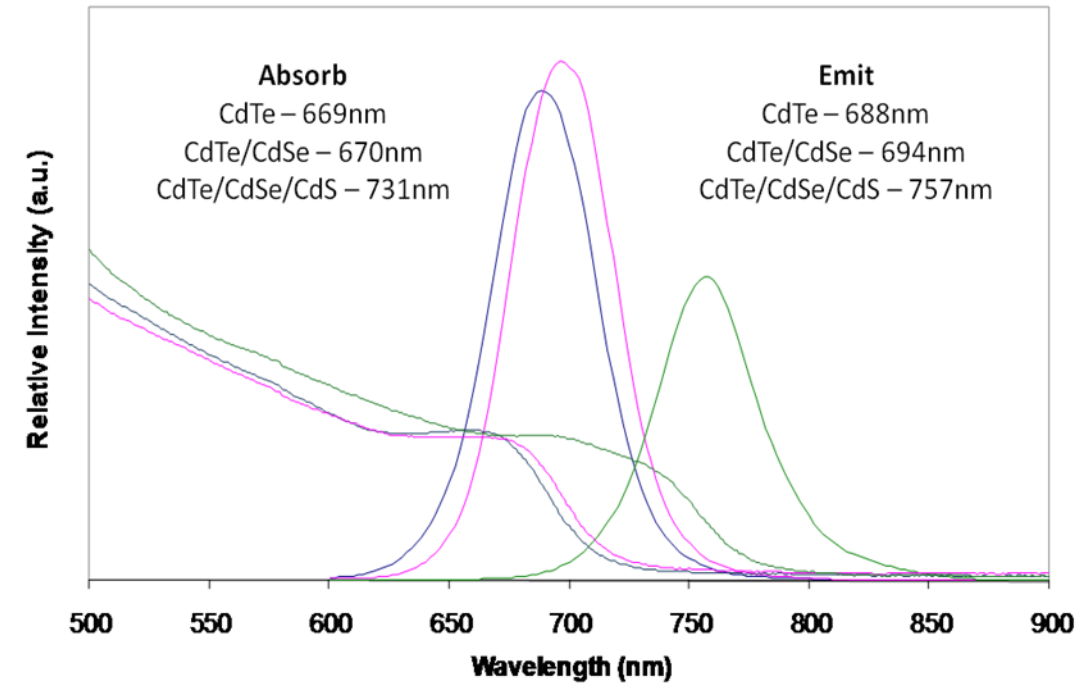

Figure 4.23 PL and UV-Vis spectra after the addition of each shell, corresponding to CdTe, CdTe/CdSe and CdTe/CdSe/CdS QDs. Each sample was excited at 480 nm for each PL spectrum.

The PL peak shifted greatly once the CdS shell had been added to the CdSe/CdTe QDs as expected due to the QDs increasing in size. Figure 4.24 shows the TEM image of monodispersed CdTe/CdSe/CdS QDs which are ~7 nm in diameter.

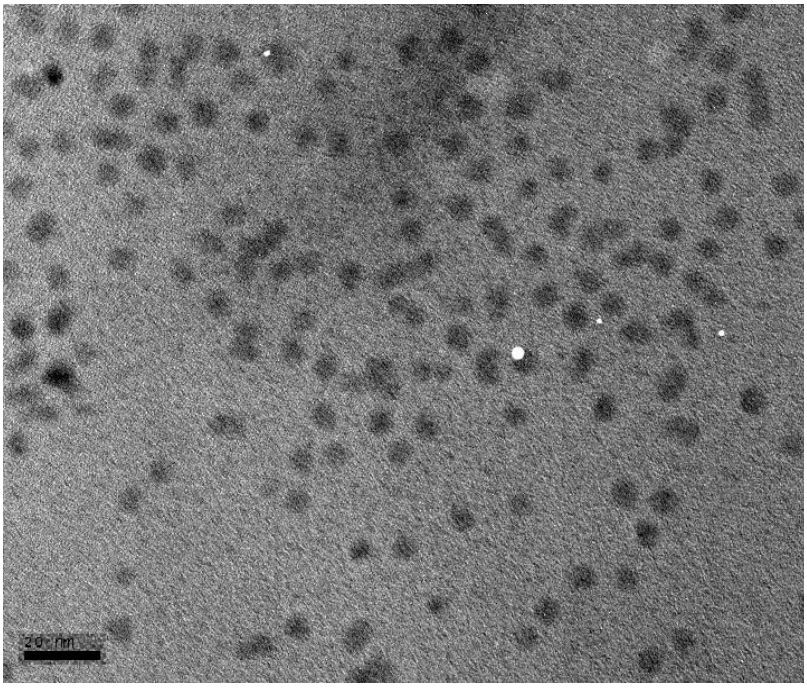

Figure 4.25 TEM image of CdTe/CdSe/CdS (scale bar = 20 nm) ~7 nm in size.

The QY decreases on shelling with CdS, but the overall stability of the QD is significantly improved. This effect is shown in a QY time study (Figure 4.25). An initial drop of 35% to 28% is noted between days 2 and 6 as the QDs were aged in air. The sample was then flushed with N_2 and then kept in an air tight vial and we can note that the QY remained almost constant, allowing for instrument error, at 27% for the initial 3 weeks after synthesis. The sample was then left under nitrogen and measured a month later to have a QY of 12%.

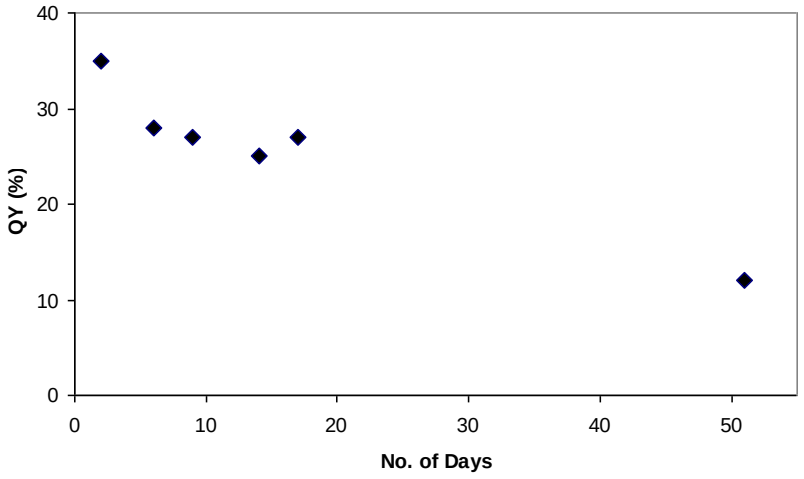

Figure 4.25 The QY study over 51 days.

To characterise the material it was analysed by powder XRD. Once the CdTe core was shelled with CdSe and CdS it was compared with the diffraction pattern of bulk cubic CdTe (ICDD (10-0207)), shown in Figure 4.26, and it was noted that the resulting pattern shifted slightly to larger scattering angles supporting the successful shelling of CdSe and CdS. Strong reflections can be seen at angles of 23.6°, 39.2° and 46.2° which are indexed to the scattering from (111), (220) and (311) lattice planes of cubic CdTe core. The reason why the diffraction peaks have shifted to higher angles is because they are moving towards the positions of bulk CdSe and CdS peaks.

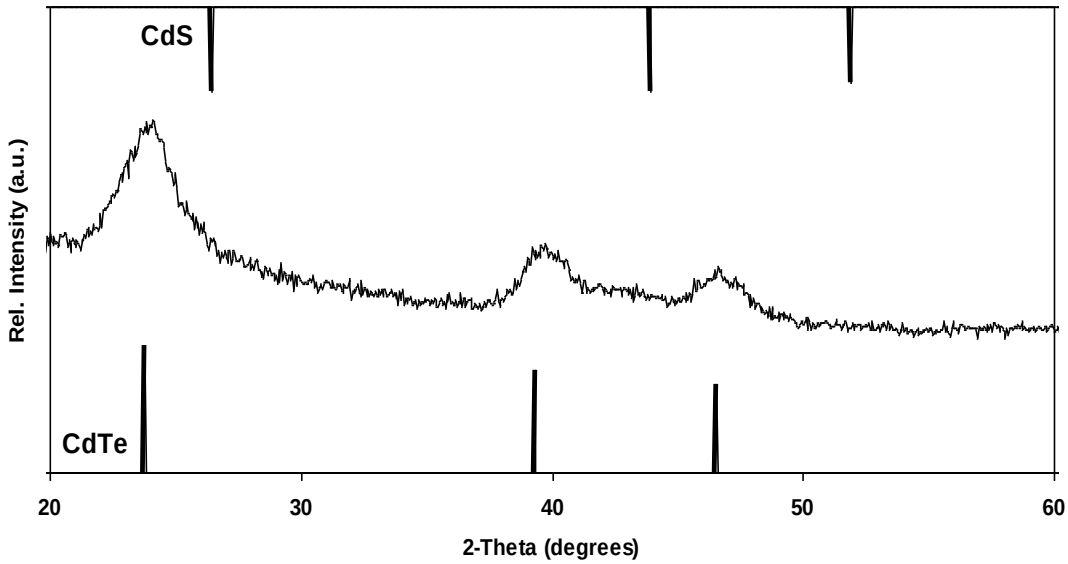

Figure 4.26 X-ray diffraction pattern from CdTe/CdSe/CdS with standard diffraction lines of cubic CdTe and cubic CdS. Strong reflections can be seen at angles of 23.6°, 39.2° and 46.2° which are indexed to the scattering from (111), (220) and (311) lattice planes of cubic CdTe core. The diffraction peaks have shifted to a higher angle as they are moving towards the positions of bulk CdSe and CdS peaks.

The PL decay transient is shown in Figure 4.27; a good fit was achieved with a tri–exponential function with time-constants and relative amplitudes of 42.9 ± 0.2 ns (57%), 4.4 ± 0.1 ns (36%), and 160 ±1 ns (7%). A similar multi-exponential decay has been previously reported[160] where, as in this study, the associated time-constants were found to be 3-5 times greater than those found for CdTe core. A reduced rate of radiative decay indicates that the wave-function overlap between the electron and hole has been reduced and is therefore consistent with their expected increased spatial separation in a Type II QDs.

By utilizing both type-II and type-I systems we are able to ensure that the dots are emitting in the NIR region and are also stable. The addition of the CdS shell serves

as a type-I heterojunction with the CdSe layer ensuring the confinement of both photogenerated electrons and holes within the CdTe/CdSe structure and substantially enhancing the spatial indirect radiative recombination at the CdTe core and inner CdSe shell interface. This is because CdS has a wide bulk bandgap, 2.42 eV, in comparison with CdTe (1.56 eV) and CdSe (1.70 eV).

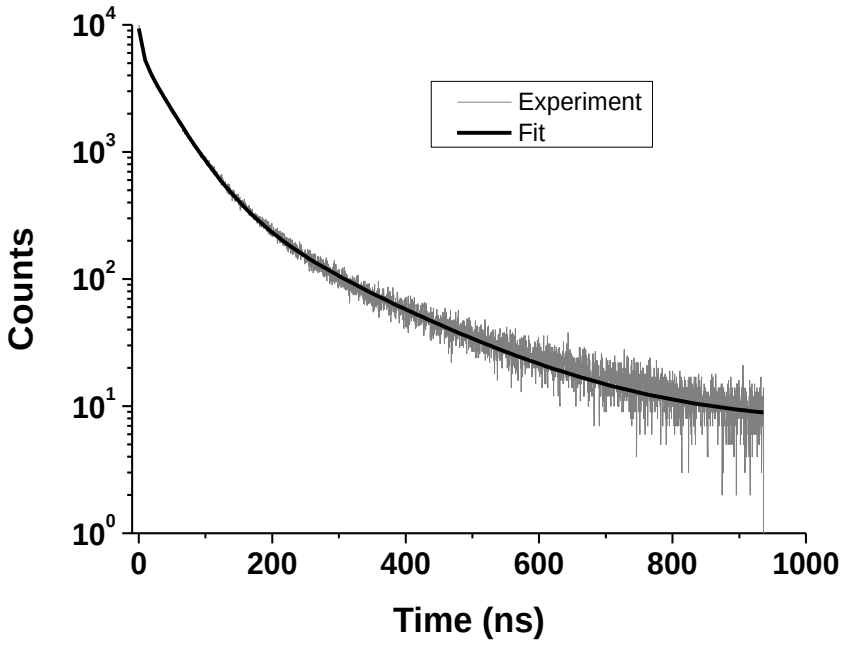

Figure 4.27 PL decay transient for the CdTe/CdSe/CdS quantum dots.

4.4 Conclusion

In conclusion, we have reported a facile two stage and one-pot synthetic approach to the formation of highly luminescent NIR core/shell/shell, CdSe/CdTe/CdS and CdTe/CdSe/CdS respectively, type-II/type-I QDs with high stability. The CdSe/CdTe/CdS QDs had a QY that was initally 48% and emitted at 742 nm, which decreased to 22% after 8 weeks under a nitrogen atmosphere. The CdSe/CdTe/CdS QDs had a QY of initally 35% and emitted at 757 nm which decreased to 12% after 51 days under a nitrogen atmosphere. TEM images showed that both samples were monodispersed, spherical in shape and ~7 nm in size.

Time resolved PL measurements for CdTe/CdSe/CdS revealed the radiative recombination rates to be significantly smaller than for CdTe core only QDs, consistent

with the increased electron-hole separation expected in a Type II QD.

NIR emitting QDs have recently attracted considerable interest as they are promising materials in comparison to current dyes being used for bioimaging probes in both biological and medical fields. Therefore, their ability for emitting in the NIR region with a high PL QY makes them especially interesting for *in-vivo* applications.

CHAPTER 5 CONCLUSIONS AND FURTHER WORK

5.1 Conclusion and Further Work

The overall aim of this project was to synthesise QDs that could be used to deliver a technology platform for high-throughput (HT) manipulation of embryonic stem cells through encoded bead-based delivery of RNAi and protein libraries ("beadfection"). A range of different chalcogenides were used to synthesise cadmium based QDs that emitted over the entire visible region and into the NIR region.

Using core/shell, core/shell/shell and alloyed QDs a range from 390 – 757 nm was achieved with varying QY values. It was found that the alloyed QDs provided the most stable QDs with the highest QYs of 70% in the visible region. These bright emitting QDs were successfully encapsulated in thiol-containing microspheres and resulted in PL maxima remaining constant, with QYs measuring 23% and 25%; this was reduced to 14% when made aqueous compatible, which is a marked improvement on previous reports. These PVP-QDs could be possibly used for bioimaging and encoding applications.

A theoretical study[121] showed that a graduated potential reduces the effect of auger recombination, which is largely attributed to the recombination route for the off state in blinking. This was confirmed when blinking studies were carried out on core/shell, CdSe/ZnS, QDs and alloyed, $Cd_{1-x}Zn_xSe_{1-y}S_y$ QDs. The CdSe/ZnS QDs were predominantly in the "off" state, but the alloyed QDs were in an "on" state for a large period of time.

CdSe/CdTe/CdS and CdTe/CdSe/CdS QDs were successfully synthesised and they both emitted in the NIR region at 757 nm and 742 nm with QYs of 35% and 48% respectively. This is especially exciting as QDs emitting in this region can be applied to improve methods for early tumour detection. The window is good for *in vivo* imaging because of minimal light absorption by haemoglobin (<650 nm) and water (>900 nm). The QDs were stable when under a nitrogen atmosphere but when encapsulation was attempted the QDs were no longer luminescent and agglomeration occurred. Work needs to be continued in this area to stablise these QDs so that the QY is retained and can be made aqueous compatible.

CHAPTER 6 EXPERIMENTAL

6.1 Chemicals

Cadmium oxide (99.5%, CdO), tellurium powder (99.8%, 200 mesh), octadecene (tech. 90%, ODE), trioctylphosphine (tech. 90%, TOP), tributylphosphine (97%, TBP), trioctylphosphine oxide (90%, TOPO), octadecylamine (90%), zinc stearate (tech.), triethylamine (99.5%), sulfur powder, oleylamine (70%), potassium ethyl xanthogenate (96%), tetramethylammonium chloride (97%), benzenethiol (>98%), cadmium acetate (98%), sodium hydroxide pellets(>98%), carbon disulfide (>99.99%), cadmium nitrate tetrahydrate (98%) and cadmium chloride (99.99%) were purchased from Aldrich and used as received. Sellenium powder(99.7%, <325 mesh) was purchased from Acros and used as received. Tetradecylphosphonic acid (98%, TDPA), n-octadecylphosphonic acid, zinc chloride (99.98%) and hexadecylamine (90%) were purchased from Alfa Aesar and used as received.

6.2 Solvents

Toluene, THF and methanol were dried by refluxing for 1 h under nitrogen and then distilling. Dry chloroform, acetonitrile (99.8%) and acetone (99%) were purchased from Aldrich and used as received.

6.3 Manipulation of air sensitive compounds

A standard Schlenk line consisting of four vacuum and four nitrogen arms was used for all QD syntheses. The nitrogen was supplied from BOC gas cylinders. The vacuum was provided by a rotary oil pump and waste products were collected in a cold trap cooled with liquid nitrogen. Air sensitive products were isolated under nitrogen using centrifuge tubes with large suba seals secured by metal wire. The products were injected into the centrifuge tubes and once isolated dissolved with minimal dry chloroform and transferred to air tight vials under a nitrogen atmosphere.

6.4 Syntheses

6.4.1 Chapter 2 Experimental CdSe/ZnS Nanoparticles

6.4.1.1 Synthesis of CdSe Nanoparticles

CdO (0.25 g, 1.95 mmol) in oleic acid (2.25 ml, 7.09 mmol) and ODE (6 ml, 18.75 mmol) were degassed and heated until colourless. Separately, Se (0.20 g, 2.53 mmol) was dissolved in TOP (3 ml, 6.73 mmol). Once dissolved ODA (3 g, 11.13 mmol) and TDPA (2 g, 7.18 mmol) were added and the solution was heated until colourless. The Se solution was injected into the Cd solution at 240 ^{o}C and then cooled to the growth temperature of 210 ^{o}C. The solution after a period of time was then cooled and isolated using 1:1 mixture of dry methanol (20 ml) and dry chloroform (20 ml) and excess acetone (~60 ml) was added to promote precipitation. The particles were collected using centrifugation. A summary of the quantity of selenium used and growth times are given in Table 6.1.

Sample ID	Amount of TOPSe (0.2M) Solution (ml)	Time left to anneal (m)	Resulting Wavelength (nm)
KP68a	3	0.33	No emission
KP68b	3	18	No emission
KP69a	6	1	539
KP69b	6	18	545
KP70a	8	0.33	578
KP55	8	18	588
KP70b	8	18	617

Table 6.1 Table showing sample ID, quantity of selenium solution injected, reaction time and resulting emission wavelength.

6.4.1.2 Synthesis of Zinc Ethylxanthate

Zinc chloride (0.684 g, 5.0 mmol) was added to distilled water (20 ml). Separately, potassium ethyl xanthogenate (1.603 g, 10 mmol) was added to distilled water (20 ml). The zinc chloride solution was added dropwise with a Pasteur pipette to the potassium ethyl xanthodenate solution whilst stirring. A white precipitate formed immediately. The precipitate was collected by filtration, washed with water and dried.

6.4.1.3 Synthesis of CdSe/ZnS Nanoparticles

In a typical synthesis, CdSe (0.5 g, 2.61 mmol) was added to oleylamine (10 ml, 30.39 mmol) and ODE (10 ml, 31.25 mmol) which was degassed and then heated to 200 ^{o}C under a nitrogen atmosphere. Zinc ethylxanthate (0.0185 g, 0.1 mmol) was dissolved in TOP (1 ml, 2.24 mmol) and zinc stearate (0.19 g, 0.3 mmol) were separately dissolved in TOP (1 ml, 2.24 mmol). The two zinc solutions were combined and injected slowly, a rate of ~1 drop every 5 s, into the cadmium solution at 200 ^{o}C. Once the zinc solution was added the reaction mixture was cooled and the particles were isolated with a 1:1 mixture of methanol (20 ml) and chloroform (20 ml), precipitated using excess acetone (~50 ml) and collected using centrifugation.

Table 6.2 shows a summary of some of the reactions, and amount of zinc precursor required to grow both thin and thick ZnS shells.

Sample ID	Sample ID of core	Quantity of zinc ethylxanthate (g)	Quantity of zinc stearate (g)	Temperature of cadmium solution (^{o}C)	Resulting Wavelength (nm)
KP71	KP69a	0.0185	0.19	200	557
KP72	KP69b	0.0185	0.19	200	569
KP73	KP55	0.006	0.065	200	594
KP62	KP55	0.0185	0.19	210	599
KP63	KP55	0.0185	0.19	200	608

Table 6.2 Table showing sample ID, quantity of zinc precursors, reaction temperature and the resulting emission wavelength

6.4.1.4 Synthesis of $[NMe_4]_4[Cd_{10}Se_4(SPh)_{16}]$

$Cd(NO_3)_2.4H_2O$ (21 g, 68 mmol) in methanol (60 ml) was added to a well stirred solution of benzenethiol (20 g, 182 mmol) and triethylamine (18.5g, 182 mmol) in methanol (60 ml) at room temperature. Tetramethylammonium chloride (8.4 g, 77 mmol) in methanol (40 ml) was added and the mixture was left to stir until all the precipitate had dissolved. The solution was then left undisturbed at 0 ^{o}C overnight. The precipitate $[Me_4N]_2[Cd_4(SPh)_{10}]$ that formed was collected by filtration and dried.

Black selenium powder (0.701 g, 8.9 mmol) was added in one portion to a solution of $[Me_4N]_2[Cd_4(SPh)_{10}]$ (15 g, 8.9 mmol) in acetonitrile (20 ml) at room temperature. The mixture was stirred for 3 h until the selenium became a white precipitate. The mixture was heated to 75 ^{o}C and acetonitrile (100 ml) was added until all the precipitate had dissolved. The pale yellow solution was cooled to room temperature causing a white precipitate to form which was collected and dried.

6.4.1.5 Synthesis of Red CdSe Nanoparticles

Two separate methods were used to synthesis CdSe nanoparticles which emitted in the red region of the spectrum.

1. In a typical synthesis, HDA (62.5 g, 258.84 mmol) and octylamine (6.39 ml, 38.69 mmol) were degassed at 120 ^{o}C before cooling to 70 ^{o}C. The previously synthesised cadmium cluster precursor $[Me_4N]_4[Cd_{10}Se_4(SPh)_{16}]$ (0.25 g) was added to TOPSe (1.0 M, 1 ml) and cadmium acetate (0.53 g, 1.99 mmol) in TOP (4 ml). The cadmium solution was added to the HDA and the temperature was slowly increased to 150 ^{o}C. From 150-200 ^{o}C more TOPSe (1.0 M, 4.25 ml) and cadmium acetate (2.66g, 9.98 mmol) in TOP (6.75 ml, 15.13 mmol) were added dropwise. After 60 h the solution was cooled to 80 ^{o}C and the particles were isolated by adding excess dry methanol. The particles had a wavelength of 610 nm.

2. In a typical synthesis, CdO (1.156 g, 9.00 mmol) and oleic acid (15 ml, 47.26 mmol) were degassed in ODE (15 ml, 46.88 mmol) and then heated to 250 ^{o}C under N_2 atmosphere. Separately, a TOPSe (2.1 M, 5 ml) stock solution was prepared. TOPSe (0.15 ml) was added to oleylamine (5 ml, 15.20 mmol) and degassed. The cadmium solution was injected into the selenium solution at 280 ^{o}C. Once the particles had reached the required size the reaction was cooled to 60 ^{o}C. The particles were isolated by adding 1:1 dry methanol and dry chloroform and then excess acetone to promote precipitation of the particles were collected by centrifugation. The particles had a wavelength of 641 nm.

6.4.1.6 Synthesis of CdSe/ZnS Nanoparticles

Red cores formed by both methods were shelled with ZnS, the second method core was also shelled with a thin shell. In a typical synthesis, CdSe (0.5 g, 2.61 mmol) was added to oleylamine (10 ml, 30.39 mmol) and ODE (10 ml, 31.25 mmol) which was degassed and then heated to 200 ^{o}C under a nitrogen atmosphere. Zinc ethylxanthate (0.0185 g, 0.1 mmol) was dissolved in TOP (1 ml, 2.24 mmol) and zinc stearate (0.19 g, 0.3 mmol) was separately dissolved in TOP (1 ml, 2.24 mmol). The two zinc solutions were combined and injected slowly, a rate of ~1 drop every 5 s, into the cadmium solution at 200 ^{o}C. Once the zinc solution was added the reaction mixture was cooled and the particles were isolated

with a 1:1 mixture of methanol (20 ml) and chloroform (20 ml), precipitated using excess acetone (~50 ml) and collected using centrifugation.

Table 6.3 shows a summary of the amounts of zinc ethylxanthate and zinc stearate used, and the temperatures the nanoparticles were grown at.

Sample ID	CdSe Core (nm)	Quantity of zinc ethylxanthate (g)	Quantity of zinc stearate (g)	Temperature of cadmium solution (^{o}C)	Resulting Wavelength (nm)
KP145	608	0.0185	0.19	200	607
KP146	641	0.006	0.065	200	650
KP150	641	0.0185	0.19	200	651

Table 6.3 Table showing sample ID, quantity of zinc precursors, reaction temperature and resulting wavelength.

6.4.2 Chapter 3 Experimental– Alloyed Nanoparticles

6.4.2.1 $Zn_xCd_{x-1}S$ Nanoparticles

CdO (0.064 g, 0.5 mmol), ZnO, and oleic acid (5 ml, 15.75 mmol) were added to ODE (40 ml, 125 mmol) and degassed for 2 h and then heated to 310 ^{o}C under N_2 atmosphere until a colourless solution was achieved. Sulfur powder was dissolved in ODE (10 ml, 31.25 mmol) separately. The cadmium/zinc solution was cooled to 300 ^{o}C at which point the sulfur solution was injected in under 1 s. Different concentrations of zinc and sulfur were used to form different sized particles, a summary of which can be seen in Table 6.4. The particles were isolated using dry methanol (30 ml), excess dry chloroform (100 ml) and excess acetone (100 ml) to promote precipitation and the particles were collected by centrifugation. x in Table 6.4 is equal to the number of mmols of zinc oxide and sulfur required.

x	CdO (g)	ZnO (g)	S (g)	Wavelength (nm)
0.15	0.064	0.122	0.048	449
0.2	0.064	0.163	0.064	426
0.3	0.064	0.245	0.096	400

Table 6.4 Table showing the value of x, cadmium, zinc and sulfur quantities and the resultant wavelengths.

6.4.2.2 $Cd_{1-x}Zn_xSe_{1-y}S_y$ Nanoparticles

In a typical synthesis, cadmium oxide (0.051 g, 0.4 mmol) and zinc acetate (0.733 g, 4 mmol) were dissolved in OA (5.6 ml, 15.75 mmol) and ODE (20 ml, 62.50 mmol). The solution was degassed and heated up to 310 ^{o}C. Separately, sulfur and selenium were dissolved in TOP (3 ml, 6.72 mmol). See Table 6.5 for values. The sulfur/selenium solution was injected into the cadmium solution, which was at 310 ^{o}C, in under 1 s. The solution was cooled to 300 ^{o}C for the growth period of 5 mins. The solution was cooled to room temperature and isolated using a 1:1 mixture of dry methanol (20 ml)/dry chloroform (20 ml) and then excess acetone (50 ml) was added to promote precipitation of the particles which were then collected by centrifugation.

ID	CdO	Zn $(OAc)_2$	Se	S	Wavelength (nm)	QY (%)
KP197	0.4 mmol, 0.051 g	4 mmol, 0.733 g	0.1mmol, 0.007896 g	4 mmol, 0.128 g	622	50
KP260	0.4 mmol, 0.051 g	4 mmol, 0.733 g	0.1mmol, 0.007896 g	4 mmol, 0.128 g	580*	70
KP189	0.4 mmol, 0.051 g	4 mmol, 0.733 g	0.4 mmol, 0.03158 g	4 mmol, 0.128 g	597	60
KP190	0.4 mmol, 0.051 g	4 mmol, 0.733 g	0.025 mmol, 0.001974 g	4 mmol, 0.128 g	604#	7
KP278	0.4 mmol, 0.051 g	4 mmol, 0.733 g	0.3 mmol, 0.02369 g	4 mmol, 0.128 g	618	25
KP283	0.4 mmol, 0.051 g	4 mmol, 0.733 g	0.1 mmol, 0.007896 g	10 mmol, 0.3207 g	390	3
KP284	0.4 mmol, 0.051 g	4 mmol, 0.733 g	0.1 mmol, 0.007896 g	8 mmol, 0.2566 g	400	7
KP281	0.4 mmol, 0.051 g	4 mmol, 0.733 g	0.1 mmol, 0.007896 g	6 mmol, 0.19242 g	586	67
KP280	0.4 mmol, 0.051 g	4 mmol, 0.733 g	0.1 mmol, 0.007896 g	3 mmol, 0.09621 g	596	65
KP282	0.4 mmol, 0.051 g	4 mmol, 0.733 g	0.1 mmol, 0.007896 g	1 mmol, 0.03207 g	605	59
KP182	0.4 mmol, 0.051 g	4 mmol, 0.733 g	1 mmol, 0.07896 g	2.3 mmol, 0.07376 g	622	30
KP184	0.4 mmol, 0.051 g	4 mmol, 0.733 g	1.3 mmol, 0.103 g	2 mmol, 0.064 g	602	27

Table 6.5 Table showing the value of cadmium, zinc, selenium and sulfur quantities and the resultant wavelengths and QY. *reaction time was only 3 min. #reaction time was 10 min

6.4.3 Chapter 4 Experimental - NIR

6.4.3.1 Synthesis of 3.5 nm CdSe Nanoparticles

CdO (0.25 g, 1.95 mmol) in oleic acid (2.25 ml, 7.09 mmol) and ODE (6 ml, 18.75 mmol) were degassed and heated until colourless. Separately, Se (0.20 g, 2.53 mmol) was dissolved in TOP (3 ml, 6.73 mmol). Once dissolved ODA (3 g, 11.13 mmol) and TDPA (2 g, 7.18 mmol) were added and the solution was heated until colourless. The Se solution was injected into the Cd solution at 240 ^{o}C and then cooled to the growth temperature of 210 ^{o}C for 10 min. The solution was then cooled and isolated using 1:1 mixture of dry methanol (20 ml) and dry chloroform (20 ml). Excess acetone (~60 ml) was added to promote precipitation and the particles were collected using centrifugation.

6.4.3.2 [Cd{S_2CNMe(Hex)}$_2$] Synthesis

Sodium hydroxide (3 g, 75 mmol) was dissolved in methanol (150 ml) in a beaker. Separately, HexMeNH (11.38 ml, 75 mmol) was dissolved in methanol and then added to the sodium hydroxide solution. The beaker was placed in an ice bath and stirred for 30 min. CS_2 (4.5 ml, 75 mmol) was dissolved in methanol and added dropwise to the reaction mixture. The solution was allowed to stir for a further 30 min during which it turned pale yellow and was removed from the ice bath. A cadmium chloride soluntion was prepared by dissolving cadmium chloride (6.88 g, 37.5 mmol) in distilled water (50 ml). The $CdCl_2$ solution was added very slowly, dropwise, to the reaction mixture to form a white suspension. The suspension was allowed to stir for a further 20 min before filtering and washing with methanol. The solid was allowed to dry and then was recrystallised from chloroform to form a pale yellow solid.

6.4.3.3 Synthesis of CdSe/CdTe/CdS Nanoparticles

Precursors were all made up to 0.04M solutions and stored at room temperature in a vial under a N_2 atmosphere:

Cd – CdO (0.05 g, 0.39 mmol) in oleic acid (1 ml, 3.15 mmol) and ODE (9 ml, 28.13 mmol) were heated to 240^{o}C to form a clear solution.

Te – Te powder (0.06 g, 0.47 mmol) in TBP (1.91 ml, 7.65 mmol) was added to degassed ODE (10 ml, 31.25 mmol). The solution was heated until the tellurium had dissolved.

Se – Se powder (0.38 g, 4.81 mmol) in TBP (1.91 ml, 7.65 mmol) was added to degassed ODE (10 ml, 31.25 mmol). The solution was heated until the selenium had dissolved.

CdS – $[Cd(S_2CNMe(Hex))_2]$[150] (0.23 g) in TBP (1.91 ml, 7.65 mmol) was added to degassed ODE (10 ml, 31.25 mmol). The solution was heated until $[Cd(S_2CNMe(Hex))_2]$ dissolved.

CdSe (9.58 mg, 0.05 mmol) in oleic acid (6.7 ml, 21.11 mmol) and ODE (7.6 ml, 23.75 mmol) were degassed and heated to 190 ^oC.

The Cd precursor (0.28 ml) was injected dropwise and after a 5 min interval the Te precursor (0.28 ml) was injected dropwise. The temperature was increased to 250 ^oC and left for 30 min. After 30 min the CdS precursor (1 ml) was injected slowly and the reaction was left for a further 30 min. The solution was then cooled and the particles were precipitated using excess acetone and collected using centrifugation. The particles were then dissolved in dry toluene and stored in a vial under N_2 atmosphere.

6.4.3.4 Synthesis of 4.5 nm CdSe Nanoparticles

For this synthesis two stock solutions were prepared. The cadmium stock solution (0.3 M) was prepared by adding CdO (0.518 g, 4.03 mmol) in oleic acid (5 ml, 15.75 mmol) and ODE (5 ml, 15.63 mmol). The solution was degassed then heated until colourless and then cooled to ~60 ^oC. The selenium stock solution was prepared by dissolving selenium (0.33 g, 4.18 mmol) in TOP (2 ml, 4.48 mmol).

Oleylamine (25 ml, 75.98 mmol) and the selenium solution (0.6 ml) were degassed ~90 ^oC and then heated to 300 ^oC under nitrogen. The cadmium solution (4 ml) was injected quickly into the selenium mixture and the temperature was reduced to the growth temperature of 280 ^oC and left for 5 min. The solution was then cooled and the particles were isolated using 1:1 dry methanol (40 ml) and dry chloroform (40 ml) and then precipitated using excess acetone. The particles were collected using centrifugation.

6.4.3.5 Synthesis of CdSe/CdS Nanoparticles

In a typical synthesis, the 4.5 nm cores were synthesised by the method described in 6.4.3.4. CdSe (9.56 mg, 0.05 mmol) was added to oleic acid (7.7 ml, 24.26 mmol) and ODE (7.6 ml, 23.75 mmol). The solution was degassed and then heated to 250 ^oC under nitrogen. The CdS precursor (0.04M, 1 ml) (for preparation see 5.4.3.3) was then slowly injected into the reaction mixture at 250 ^oC for 30 min. The solution was then cooled and

the particles were isolated using 1:1 dry methanol (40 ml) and dry chloroform (40 ml) and then precipitated using excess acetone. The particles were collected using centrifugation.

6.4.3.6 Synthesis of CdTe Nanoparticles

CdO (0.128 g, 0.1 mmol) and ODPA (0.068 g, 0.205 mmol) were added to ODE (5 ml, 3.93 mmol) and degassed then heated to 300 ^{o}C. Separately, tellurium (0.025 g, 0.2 mmol) was dissolved in TBP (0.58 ml, 2.34 mmol) and ODE (1.9 ml, 5.04 mmol). The Te solution was injected rapidly into the cadmium solution at 300 ^{o}C and then cooled to the growth temperature 250^{o}C. Aliquots were taken at regular intervals. After 17.5 h the sample was cooled and isolated using a 1:1 dry methanol/dry chloroform and excess acetone mixture. The particles were then collected using centrifugation.

6.4.3.7 Synthesis of CdTe/CdSe Nanoparticles

CdO (51.36 mg, 0.40 mmol) in TOP (2.66 ml, 5.96 mmol) was degassed and heated to 310 ^{o}C to form a clear solution under nitrogen. To this, a solution of Te (25.52 mg, 0.20 mmol) in TOP (1.90 ml, 4.26 mmol) was injected quickly at 300 ^{o}C. The solution was cooled to 250 ^{o}C and left for 15 min after which it was cooled to 150 ^{o}C. Se (8 mg, 0.10 mmol) dissolved in TOP (0.4 ml, 0.90 mmol) was added to a stock solution of CdO (25.72 mg, 0.20 mmol) dissolved in TOP (3.6 ml, 8.07 mmol) and then added over 1 h, using a syringe pump, to the reaction mixture as the temperature was increased slowly to 200 ^{o}C. The reaction mixture was then kept at 200 ^{o}C for 15 min. The reaction mixture was cooled and was precipitated with the addition of 1:1 dry methanol:THF, excess acetone and then collected using centrifugation under N_2 atmosphere and resuspended in 7 ml dry chloroform.

6.4.3.8 Synthesis of CdTe/CdSe/CdS Nanoparticles

CdO (51.36 mg, 0.40 mmol) in TOP (2.66 ml, 5.96 mmol) was degassed and heated to 310 ^{o}C to form a clear solution under nitrogen. To this, a solution of Te (25.52 mg, 0.20 mmol) in TOP (1.90 ml, 4.26 mmol) was injected quickly at 300 ^{o}C. The solution was cooled to 250 ^{o}C and left for 15 min after which it was cooled to 150 ^{o}C. Se (8 mg, 0.10 mmol) dissolved in TOP (0.4 ml, 0.90 mmol) was added to a stock solution of CdO (25.72 mg, 0.20 mmol) dissolved in TOP (3.6 ml, 8.07 mmol) and then added over 1 h, using a syringe pump, to the reaction mixture as the temperature was

increased slowly to 200 °C. The reaction mixture was then kept at 200 °C for 15 min. [Cd{S_2CNMe(Hex)}$_2$] (0.04 M, 0.23 g, 0.79 mmol) in TBP (1 ml, 4 mmol) and ODE (10 ml, 31.25 mmol) was prepared and injected (2 ml) slowly to the reaction mixture. Once all of the CdS solution was injected the temperature was increased to 250 °C for 30 min. The mixture was then cooled and the particles were precipitated with the addition of 1:1 dry methanol:THF, excess acetone and then collected using centrifugation under N_2 atmosphere and resuspended in 7 ml dry chloroform.

6.5 Instrumentation and physical measurements

6.5.1 UV/Vis spectroscopy

A ThermoSpectronic Heλios UVB v4.55 spectrophotometer was used to record the absorption spectra of the QDs samples which were measured as either toluene or chloroform solutions in Helma quartz cuvettes with a 1 cm path length. The optical measurements were carried out using either toluene or chloroform as a reference (depending on the QD sample prepared).

6.5.2 Photoluminescence spectroscopy

Photoluminescence (PL) spectra of the QD samples were measured using either a Horiba Jobin Yvon Fluorolog-3 instrument or a Gilden photonics fluoroSENS fluorimeter with a xenon lamp (450 W) and a 152 P photomultiplier tube as the detector. The samples were prepared and transferred to Helma quartz cuvettes with a 1 cm path length and had an optical density of less than 0.1. Spectra were obtained with the slits set to 2 nm and an integration time of 1 s. Accuracy of +/- 0.5 nm for the Horiba and +/- 0.2 nm for the Gilden. Excitation wavelength generally used was 480 nm, however when wavelengths were lower than this a different excitation value was used (see individual PL spectrum for specific excitation used).

6.5.3 Quantum Yield measurements

The quantum yields (QYs) for QD samples with an optical density less than 0.1 were measured by comparing the PL to an organic dye (rhodamine) whose spectrum overlaps significantly with the QD sample ensuring that they were both run using the same settings.

The QY was determined by comparing the integrated PL intensities of the QDs and the corresponding dye.

A fluoromax-4 spectrofluorometer with integrating sphere attachment (instrument standardised with a tungsten lamp) was used for solid or more concentrated samples. A background reference measurement was acquired for each sample. Toluene or chloroform was the reference for QD samples prepared in toluene or chloroform respectively. Solid samples that were measured were QDs in microspheres so the reference was empty microspheres. For samples, for example, excited at 480 nm in the integrating sphere a reference had an excitation spectrum measured between 470 and 490 nm and a fluorescence emission spectrum measured between 500 and 700 nm. Once the reference data were collected the QD samples were then measured by again exciting at 480 nm and taking the excitation spectra between 470 and 490 nm and the fluorescence emission spectrum between 500 and 700 nm. Inbuilt software was used to calculate the QY.

6.5.4 Powder X-ray diffraction

A Bruker AXS D8 Advance X-Ray Diffractometer was used to obtain the X-ray diffraction patterns. Secondary graphite monochromated Cu Kα radiation (λ = 1.54178 Å, 40 kV) was used to perform the X-ray diffraction (XRD). Measurements were taken using a glancing angle incidence dectector at an angle of 3^{o} for 2θ values over 20^{o} – 60^{o} in steps of 0.04^{o} with a count time of 1 s. To get a clean spectrum the sample needs to be thoroughly washed with chloroform and methanol to ensure all capping agent has been removed and only a small amount of sample is required. The samples were finely ground and placed in a single crystal silicon holder.

6.5.5 Transmission electron microscopy (TEM)

A Philips CM200 electron microscope operated at 200 kV with an Oxford Instruments AN 10000 EDS analyzer was used to obtain TEM images. The samples were prepared by placing a drop of dilute solution on copper grids (300 mesh, Agar Scientific). The excess solvent was allowed to evaporate off at room temperature. A Joel 2200 aberration corrected transmission electron microscope was used in bright field configuration was used for single crystal imaging.

6.5.6 PL decay transient

The PL decay transient was measured by a commercial time-correlated single photon counting instrument (MiniTau, Edinburgh Instruments). The sample was excited by a pulsed diode laser (EPL-405, Edinburgh Instruments), which emitted at a wavelength of 405 nm with a pulse duration of 90 ps; scattered excitation light was suppressed using a long-pass filter (cut-off wavelength = 620 nm). A Hammatsu H4722 photomultiplier tube was used as the detector and the instrument response function of the system had a full width half maximum of better than 300 ps.

The samples were prepared as dilute solutions in toluene in Helma quartz cuvettes with 1 cm path length.

6.5.7 Inductively coupled plasma atomic emission spectroscopy (ICP-AES)

The ICP-AES was measured on a Perkin-Elmer Optima 5300 dual view ICP-AES. The sample was prepared by thoroughly washing the sample with chloroform and methanol to ensure all capping agent has been removed. A 2% nitric acid solution was prepared and 5 ml was added to a QD sample (0.005 g). Then concentrated nitric acid (2-3 ml) was added and the solution was sonicated until the sample had fully dissolved.

6.5.8 Thermogravimetric Analysis (TGA)

TGA measurements to determine decomposition temperatures were carried out on a TGA Sieko SSC/S200 in air.

6.5.9 Multiphoton Excitation

An ultrafast pulsed Ti:sapphire laser was used. The laser wavelength was 800 nm with FWHM of ca. 12 ns. 100 fs pulses at 80 MHz repetition rate, low pulse energy (10 nJ) with high peak power of 0.1 MW. The sample was dissolved in toluene and placed in Helma quartz cuvettes with a 1 cm path length.

6.5.10 Single Nanocrystal Investigation

The equipment used is shown in Figure 6.1. The photon avalanche detector used to collect lifetime and blinking data was fibre optically coupled to the system isn't shown in the set up. Excitation was at 425 nm with a picoquant laser. Continuous wave or picoseconds pulse laser at a rate of up to 5 MHz was used. Typically excitation was at 20 W cm^{-2} CW and 20 W cm^{-2} pulsed. A series of laser clean up filters, dichromic mirrors and long pass filters were used to clean up the signal. Images of the nanocrystals were taken using Acton spectrometer and Princeton Instruments CCD with mirror grating. The spectral measurements were also taken using the Acton spectrometer and Princeton Instruments CCD with 500 blazed grating. Time tagged investigations were coupled to a Perkin Elmer avalanche single photon detector and used a Picoquant time correlated single photon card to obtain time resolve photoluminescence (TRPL) data. The single nanocrystal image was taken using a Joel 2200 aberration corrected TEM microscope used in bright field configuration.

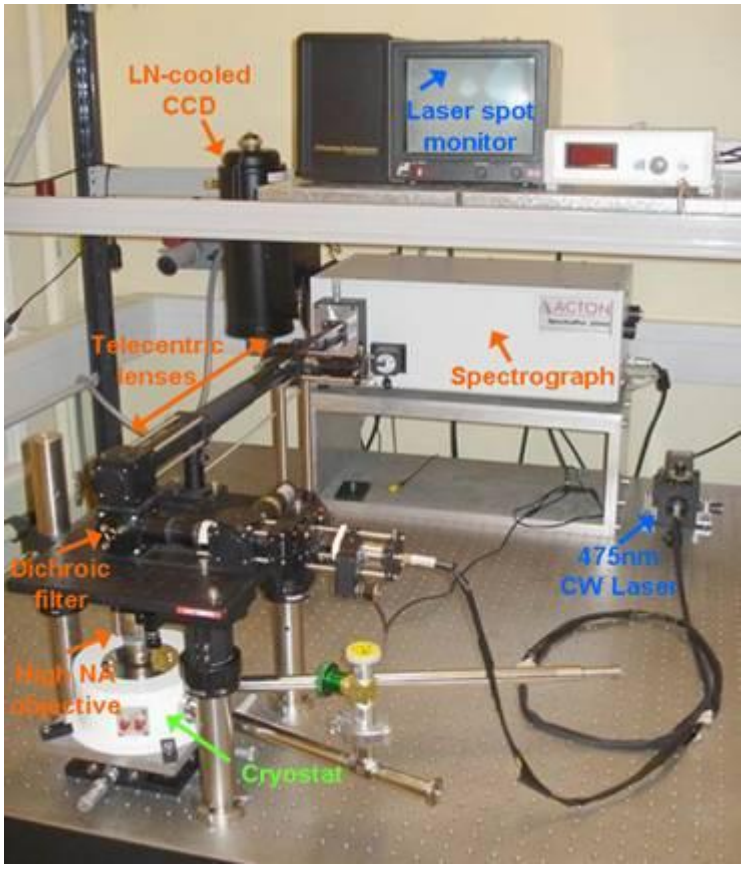

Figure 6.1 The set up for single nanocrystal investigations.[124]

The sample was dissolved in chloroform, polymethylmethacrylate (pmma) and hexadecylamine. The nanocrystals were dissolved down to nano mole concentrations and a few drops were spin cast on to a glass cover slip. These were then placed under an oil immersion lens. To do the investigations one nanocrystal was isolate.

6.5.11 Centrifuges

The centrifuges used in this research were a Jouan B4i (max. 4000 rpm) and a Centurion 882 (max. 6000 rpm). The centrifuge tubes were purchased from VWR in two sizes: 15 ml, 17x120 mm and 50 ml, 30 x 115 mm with screw caps.

APPENDIX

A.1 Experimental Procedures

This section explains the experimental procedure, methods and equipment required for the synthesis of the nanomaterials synthesised in chapters 2, 3 and 4.

A1.1 Procedure used for the synthesis of cadmium based nanoparticles.

The precursors used in the synthesis of the cadmium nanoparticles were all stable in ambient conditions. All the glassware was cleaned and oven dried before it was assembled as seen in Figure A1.1. The solvent, capping agent and cadmium source was added and degassed by putting the system under reduced pressure at ~ 100 ^{o}C for 30 min. After this time the apparatus was placed under a nitrogen free atmosphere. The temperature was raised to the desired reaction temperature. The chalcogenide source was dissolved in a small amount of solvent/capping agent and injected into the reaction vessel. The reaction mixture was heated to the desired temperature and once the reaction time had passed the mixture was cooled. The product was isolated by precipitation by the addition of a polar solvent and collected by centrifugation. The liquid was discarded and the remaining solid was washed before being dried in a desiccator.

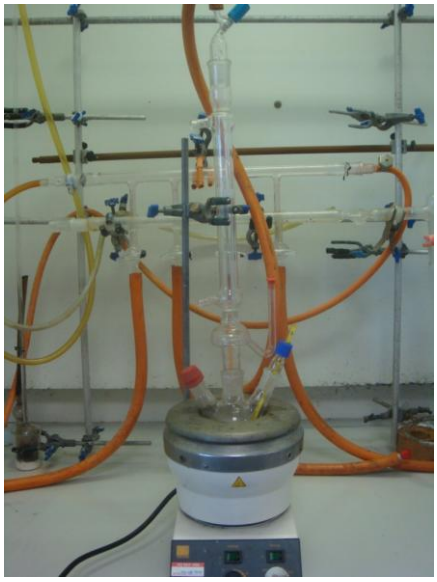

Figure A1.1 Image of standard equipment set up for all experiments described in chapters 2, 3 and 4.

REFERENCES

1. J. Pérez-Arantegui, J. Morela, A. Larrea, T. Pradell, M. Vendrell-Saz, I Borgia, B. G. Brunetti, F. Cariati, P. Fermo, M. Mellini, A. Sgamellotti, C. Viti, *J. Am. Ceram. Soc.* **2001**, *84*, 442-446.

2. M. Faraday, *Phil. Trans. R. Soc. Lond.*, **1857**, *147*, 145-181.

3. R. Feynman, Eng. and Sci., **1960**, *23*, 22-36.

4. P. Alivisatos, P. F. Barbara, A. W. Castleman, J. Chang, D. A. Dixon, M. L. Kline, G. L. McLendon, J. S. Miller, M. A. Ratner, P. J. Rossky, S. I. Stupp and M. I. Thompson, *Adv. Mater.*, **1998**, *10*, 1297-1336.

5. Y. Xia, P. Yang, Y. Sun, Y. Wu, B. Mayers, B. Gates, Y. Yin, F. Kim, H. Yan, *Adv. Mater.*, **2003**, *15*, 535-589.

6. M. Fox, *Optical Properties of Solids*, Oxford University Press, **2010**.

7. V. A. Fonoberov, E. P. Pokatilov, V. M. Fomin, J. T. Devreese, *Phys. Rev. Lett.*, **2004**, *92*, 127402-1–127402-4.

8. http://arxiv.org/ftp/cond-mat/papers/0602/0602053.pdf, accessed 24/06/07.

9. R. B. Little, M. A. El-Sayed, G. W. Bryant, S. Burke, *J. Chem. Phys.*, **2001**, *114*, 1813-1822.

10. A. Eychmuller, A. Mews, H. Weller, *Chem. Phys. Lett.*, **1993**, *208*, 59-62.

11. W. Ostwald, “Die Welt der Vernachlassigten”, Steinkopf, Dresden, **1915**.

12. P. O’Brien, N. L. Pickett, *Chem. Mater.*, **2001**, *13*, 3843-3858.

13. A. Mews, A. Eychmueller, M. Giersig, D. Schooss, H. Weller, *J. Phys. Chem.*, **1994, *98*,** 934-941.

14. E. Schrödinger, *Phys. Rev.*, **1928**, *28*, 1049-1070.

15. A. P. Alivisatos, *Science*, **1996**, *271*, 933-937.

16. L. I. Berger, *Semiconductor Materials,* CRC Press, New York, **1997**.

17. P. Reiss, M. Protiere, L. Li, *Small*, **2009**, *5*, 154-168.

18. C. A. Pickover, *The Math Book: From Pythagoras to the 57th Dimension, 250 Milestones in the History of Mathematics*, Sterling Publishing Company Inc., New York, **2009**, pg. 126.

19. http://en.wikipedia.org, accessed 20/06/07.

20. http://departments.kings.edu/chemlab/animation/clospack.html, accessed 20/06/07.

21. M. Berger, *Nano-Society; Pushing the Boundaries of Technology*, Royal Society of Chemistry, Cambridge - UK, **2009**, pg 28.

22. G. Cao, *Nanostructures and Nanomaterials*, Imperial College Press, UK, **2004**, pg.30.

23. C. R. Bullen and P. Mulvaney, *Nano Lett.*, **2004**, *4*, 2303-2307.

24. R. Rossetti, J. L. Ellison, J. M. Gibson, L. E. Brus, *J. Chem. Phys. Chem.,* **1984**, *80*, 4464-4469.

25. V. K. LaMer, R. H. Dinegar, *J. Am. Chem. Soc.,* **1950**, *72*, 4847-4854.

26. R. Rossetti, R. Hull, J. M. Gibson, L. E. Brus, *J. Chem. Phys.,* **1985**, *82*, 552-559.

27. Y. Tian, T. Newton, N. A. Kotov, D. M. Guldi, J. H. Fendler, *J. Phys. Chem.*, **1996**, *100*, 8927-8939.

28. J. G. Brennan, T. Siegrist, P. J. Carroll, S. M. Stuczynski, L. E. Brus, M. L. Steigerwald, *J. Am. Chem. Soc.*, **1989**, *111*, 4141-4143.

29. N. L. Pickett, P. O'Brien, *Chemical Record*, **2001**, *1*, 467-469.

30. W. Maneeprakorn, C. Q. Nguyen, M. A. Malik, P. O'Brien, J. Raftery, *Dalton Transactions,* **2009**, 2103-2108.

31. M. Green, P. O'Brien, *Adv. Mater.*, **1998**, *10*, 527-528.

32. N. Ravaprasadu, M. A. Malik, P. O'Brien, *J. Mater. Chem.*, **1998**, *8*, 1885-1888.

33. T. Trindade, O. C. Monteiro, P. O'Brien, M. Motevalli, *Polyhedron,* **1999**, *18*, 1171-1175.

34. M. A. Malik, P. O'Brien, N. Revaprasada, *Adv. Mater*., **1999**, *11*, 1441-1444.

35. N. Revaprasadu, M. A. Malik, J. Carstens, P. O'Brien, *J. Mater. Chem*., **1999**, *9*, 2885-2888.

36. T. Trindade, N. L. Pickett, P. O'Brien, *Chem. Mater.*, **2001**, *13*, 3843-3858.

37. C. B. Murray, D. J. Norris, M. G. Bawendi, *J. Am. Chem. Soc.*, **1993**, *115*, 8706-8715.

38. S. Sun, C.B. Murray, D. Weller, L. Folks, A. Moser, *Science*, **2000**, *287*, 1989-1992.

39. P. K. Santra, R. Viswanatha, S. M. Daniels, N. L. Pickett, J. M. Smith, P. O'Brien, D. D. Sarma, *J. Am. Chem. Soc.*, **2009**, *131*, 470-477.

40. S. M. Stuczynski, J. G. Brennan, M. L. Steigerwald, *Inorg. Chem.*, **1989**, *28*, 4431-4432.

41. M. Protière, P. Reiss, *Nanoscale Res. Lett.*, **2006**, *1*, 62-67.

42. M. Protière, P. Reiss, *Small*, **2007**, *3*, 399-403.

43. L. Li, M. Protière, P. Reiss, *Chem. Mater.*, **2008**, *20*, 2621-2623.

44. S. Deka, A. Quarta, M. G. Lupo, A. Falqui, S. Boninelli, C. Giannini, G. Morello, M. De Giorgi, G. Lanzani, C. Spinella, R. Cingolani, T. Pellegrino, L. Manna, *J. Am. Chem. Soc.*, **2009**, *131*, 2948-2958.

45. Z. A. Peng, X. Peng, *J. Am. Chem. Soc.*, **2001**, *123*, 183-184.

46. L. H. Qu, Z. A. Peng, X. Peng, *Nano Lett.*, **2001**, *1*, 333-337.

47. J. H. Lui, J. B. Fan, Z. Gu, J. Cui, X. B. Xu, Z. W. Liang, S. L. Luo, M. Q. Zhu, *Langmuir*, **2008**, *24*, 5241-5244.

48. J. R. Dean, A. M. Jones, D. Holmes, R. Reed, J. Weyers, A. Jones, *Practical Skills in Chemistry*, Pearson Education Limited, UK, **2002**, pg 165.

49. C. E. Housecroft, E. C. Constable, *Chemistry: an introduction to organic, inorganic and physical chemistry,* Pearson Education Limited, UK, **2006**, pg. 348.

50. L. Cao, S. Huang, E. Shulin, *J. Colloid and Interface Science*, **2004**, *273*, 478-482.

51. A. L. Efros, M. Rosen, M. Kuno, M. Nirmal, D. J. Norris, M. G. Bawendi, *Phys. Rev. B.*, **1996**, *54*, 4843-4856.

52. M. Pelton, G. Smith, N. F. Scherer, R. A. Marcus, *Proc. Nacl. Acad. Sci*., **2007**, *104*, 14249-14254.

53. K. T. Shimizu, R. G. Neuhauser, C. A. Leatherdale, S. A. Empedocles, W. K. Woo, M. G. Bawendi, *Phys. Rev. B.*, **2001**, *63*, 205311-205316.

54. M. Kuno, D. P. Fromm, A. Gallagher, D. J. Nesbitt, O. I. Micic, A. J. Nozik, *Nano Lett*, **2001**, *1*, 557–564.

55. S. Wang, C. Querner, T. Emmons, M. Drndic, C. H. Crouch, *J. Phys. Chem. B.,* **2006**, *110*, 23221–23227.

56. M. Kuno, D. P. Fromm, H. F. Hamann, A. Gallagher, D. J. Nesbitt, *J. Chem. Phys.*, **2001**, *115*, 1028–1040.

57. R. J. Cook, H. Kimble, *Phys. Rev. Lett.*, **1985**, *54*, 1023-1026.

58. A. L. Efros, M. Rosen, *Phys. Rev. Lett.*, **1997**, *78*, 1110-1113.

59. R. G. Neuhauser, K. T. Shimizu, W. K. Woo, S. A. Empedocles, M. G. Bawendi, *Phys. Rev. B.*, **2000**, *85*, 3301-3304.

60. B. Mahler, P. Spinicelli, S. Buil, X. Quelin, J. P. Hermier, B. Dubertret, *Nature Mater.*, **2008**, *7*, 659-664.

61. A. L. Efros, V.A. Kharchenko, M. Rosen, *Solid State Comm.*, **1995**, *93*, 301-305.

62. V.I. Klimov, *Semiconductor and Metal Nanocrystals: Synthesis and Electronic and Optical Properties*, Marcel Dekker, Inc., New York, **2004**.

63. R.D. Schaller, M.A. Petruska, and V.I. Klimov, Applied Physics Letters, **2005**, *87*, 253102-253103.

64. V.I. Klimov, *J.Phys. Chem. B*, **2000**, *104*, 6112-6123.

65. S. Stubbs, D. Binks, *Ultrafast Laser Spectroscopy of CdSe Nanocrystal Quantum Dots,* **2007**, *University of Manchester.*

66. R. Ellingson, M. C. Beard, J. C. Johnson, P. Yu, O. I. Micic, A. J. Nozic, A. Shabaev, A. L. Efros, *Nano. Letts.*, **2005**, *5*, 865-871.

67. D. Binks, PSI, The University of Manchester, Manchester.

68. M. G. Mayer, *Ann. Physiks*, **1931**, *9*, 273-294.

69. S. Mannegis, *Multiphoton Excitiation*, **2010**, *University of Manchester.*

70. A. Bullen, *Nat. Rev. Drug Discov.,* **2008**, *7*, 54-67.

71. B. Fultz, J. M. Howe, *Transmission Electron Microscopy and Diffractometry of materials*, Springer 3rd Edition, New York, **2008**.

72. Z. L. Wang, *J. Phys. Chem. B.*, **2000**, *104*, 1153-1175.

73. www.britannica.com, accessed 08/07/09.

74. V. K. Percharsky, P. Y. Zavalij, *Fundamentals of Powder Diffraction and Structural Characterization of Materials,* Springer, New York, **2003**.

75. C. Suryanarayana, M. G. Norton, *X-Ray Diffraction: a practical approach*, Springer, New York, **1998**.

76. A. Guinier, *X-ray diffraction in crystals, imperfect crystals, and amorphous bodies,* Courier Dover Publications, San Francisco, **1994**.

77. *Principles and Applications of Thermal Analysis*, Paul Gabbot, John Wiley and Sons, Oxford – UK, **2007**.

78. T. Ryänen, M. A. Uusitalo, O. Ikkala, A. Kärkkäinen, *Nanotechnologies for Future Devices*, Cambridge University Press, **2010**.

79. European Commission *Nanotechnology Innovation for tomorrow's world*, European Commission, Research DG, May 2004.

80. X. Michalet, F. F. Pinaud, L. A. Bentolila, J. M. Tsay, S. Doose, J. J. Li, G. Sundaresan, A. N. Wu, S. S. Gambhir, S. Weiss, *Science*, **2005**, *307*, 538-544.

81. F. Tokumasu, J Dvorak, *J. Microsc.*, **2003**, *211*, 256-261.

82. S. Kim, Y. T. Lim, E. G. Soltesz, A. M. De Grand, J. Lee, A. Nakayama, J. A. Parker, T. Mihaljevic, R. G. Laurence, D. M. Dor, L. H. Cohn, M. G. Bawendi, J. V. Frangioni, *Nat. Biotechnol.*, **2004**, 93-97.

83. W. Barthlott, C. Neinhuis, *Planta* **1997**, *202*, 1-8.

84. B. Bhushan, Y. C. Jung, K. Koch, *Langmuir,* **2009**, *25*, 3240-3248.

85. http://gsfctechnology.gsfc.nasa.gov/TechSheets/Lotus_Goddard_final.pdf, accessed 02/04/10

86. S. E. Cross, B. Innes, M. S. Roberts, T. Tsuzuki, T. A. Robertson, P. McCormick, *Skin Pharmacol. Physiol.*, **2007**, *20*, 148-154.

87. http://www.investmentandbusinessnews.co.uk/headline/the-two-words-economists-forget/, accessed 20/07/10.

88. F. Fayazpour, B. Lucas, N. Huyghebaert, K. Braeckmans. S. Derveaux, B. G. Stubbe, J.-P. Remon, J. Demeester, C. Vervaet, S. C. De Smedt, *Adv. Mater.*, **2007**, *19*, 3854-3858.

89. M. A. Green, K. Emery, K. Bucher, D. L. King, S. Igari, *Prog. Photovolt.: Res. Appl.*, **1996**, *4*, 321-325.

90. N. H. Karam, J. H. Ermer, R. R. King, M. Hadda, L. Cai, D. E. Joslin, D. D. Krut, M. Takahashi, J. W. Eldredge, W. Nishikawa, B. T. Cavicchi, D. R. Lillington, *Proceedings in the 2nd World Conference on Photovoltaic Solar Energy Conversion, Vienna*, **July 6th-10th 1998**, 3534-3539.

91. M. A. Green, *Prog. Photovolt.: Res. Appl.*, **2001**, *9,* 123-135.

92. S. Sapara, S, Mayilo, A. A. Klar, A. L. Rogach, J. Feldmann, *Adv. Mater.*, **2007**, *19*, 569-572.

93. D. Battaglia, B. Blackman, X. G. Peng, *J. Am. Chem. Soc.* **2005,** *127*, 10889-1897.

94. I.L. Medintz, H. T. Uyeda, E. R. Goldman, H. Mattoussi, Nature Mater., 2005, 4, 435-446

95. P. O'Brien, N. L. Pickett, T. Trindade, *Chem. Mater.*, **2001**, *13*, 3843-3858.

96. E.L. Bentzen, F. House, T.J. Utley, J.E. Crowe, D.W. Wright, Nano Lett., **2005**, *5,* 591–595.

97. V. L. Colvin, M. C. Schlamp, A. P. Alivisatos, *Nature*, **1994**, *370*, 354-357.

98. J. G. Brennan, T. Siegrist, P. J. Carroll, S. M. Stucznski, L. E. Brus, M. L. Steigerwald, *J. Am. Chem. Soc.*, **1989**, *111*, 4141-4143.

99. B. Ludolf, M. A. Malik, P. O'Brien, N. Revaprasadu, *Chem. Commun.*, **1998**, *17*, 1849-1850.

100. T. Trindade, O. C. Monteiro, P. O'Brien, M. Montevalli, *Polyhedron*, **1992**, *18*, 1171-1175.

101. S. L. Cumberland, K. M. Hanif, A. Javier, G. A. Khitrov, G. F. Strouse, S. M. Woessner, C. S. Yun, *Chem. Mater.*, **2002**, *14*, 1576-1584.

102. M. Green, P. O'Brien, *Chem. Comm.*, **1999**, 2235-2241.

103. B. O. Dabbousi, J. Rodriquez-Viejo, F. V Mikulec, J. R. Heine, H. Mattoussi, R. Ober, K. F. Jensen, M. G. Bawendi, *J. Phys. Chem. B.*, **1997**, *101*, 9463-9475.

104. H. Wang, H. Nakamura, M. Uehara, Y. Yamaguchi, M. Miyazaki, H. Maeda, *Adv. Funct. Mater.*, **2005**, *15*, 603-608.

105. X. Zhong, Y. Feng, Y. Zhang, *J. Phys. Chem. C.*, **2007**, *111*, 526-531.

106. M. B. Mohamed, D. Tonti, A. Al-Salman, A. Chemseddine, M. Chergui, *J. Phys. Chem. B.*, **2005**, *109*, 10533-10537.

107. M. A. Hines, P. Guyot-Sionnest, *J. Phys. Chem.*, **1996**, *100*, 468-471.

108. L. Qu, X. Peng, *J. Am. Chem. Soc.*, **2002**, *124*, 2049-2055.

109. M. Kuno, D. P. Fromm, H. F. Hamann, A. Gallagher, D. J. Nesbitt, *J. Chem. Phys.*, **2000**, *112*, 3117-3120.

110. K. T. Shimizu, R. G. Neuhauser, C. A. Leatherdale, S. A. Empedocles, W. K. Woo, M. G. Bawendi, *Phys. Rev. B.*, **2001**, *63*, 205316-205321.

111. S. A. Crooker, T. Barrick, J. A. Hollingsworth. V. I Klimov, *App. Phys. Lett.*, **2003**, *82*, 2793-2795.

112. I. G. Dance, A. Choy, M. L. Scudder, *J. Am. Chem. Soc.* **1984**, *106*, 6285-6295.

113. J. M. Behrendt, M. Afzaal, L. M. Alexander, M. Bradley, A. V. Hine, D. Nagel, P. O'Brien, K. Presland, A. J. Sutherland, *J. Mater. Chem.*, **2009**, *19*, 215-221.

114. W. K. Bae, K. Char, H. Hur and S. Lee, *Chem. Mater.* **2008**, *20*, 531-539.

115. M. Han, X. Gao, J. Z. Su, S. Nie, Nat. Biotechnol., 2001, 19, 631-635.

116. H.-Q. Wang, Z.-L. Huang, T.-C. Liu, J.-H. Wang, Y.-C. Cao, X.-F. Hua, X.-Q. Li, Y.-D., Zhao, *J. Fluoresc.*, **2007**, *17*, 133-138.

117. P. O'Brien, S. S. Cummins, D. Darcy Dearden, A. Dearden, O. Masala, N. L. Pickett, S. Ryley, A. J. Sutherland, *Chem. Commun.*, **2003**, 2532-2533.

118. Y. Li, E. C. Y. Lui, N. Pickett, P. J. Skabara, S. S. Cummins, S. Ryley, A. J. Sutherland, P. O'Brien, *J. Mater. Chem.*, **2005**, *15*, 1238-1243.

119. W. G. J. H. M. van Sark, P. L. T. M. Frederix, A. A. Bol, H. C. Gerritsen. A. Meijerink, *ChemPhysChem*, **2002**, *3*, 871-879.

120. X. Wang, X. Ren, K. Kahan, M. A. Hahn, M. Rajeswaran, S. Maccagnano- Zacher, J. Silcox, G. E. Cragg, A. L. Efros, T. D. Krauss, *Nature*, **2009**, *459*, 686-689.

121. A. L. Efros, *Nature. Mater.*. **2008**, *7*, 612-613.

122. A. Kiejna, K. F. Wojciechowski, *Metal Surface Electron Physics*, Elsevier, Oxford - UK, **1996**, pg 187.

123. X. Chen,′J. L. Hutchison, P. J. Dobson, G. Wakefield, *Mater. Sci. Eng., B*, **2010**, *166*, 14-18.

124**.** J. Smith, S. Fairclough, University of Oxford, Oxford, *Personal reference*.

125. Y. Chan, J. P. Zimmer, M. Stroh, J. S. Steckel, R. K. Jain, M. G. Bawendi, *Adv. Mater,.* **2004**, *16*, 2092-2097.

126. V. Stsaipura, A. Sukhanova, M. Artemyev, M. Pluot, J. H. M. Cohen, A. V. Baranov, V. Oleinikov, I. Nabiev, *Anal. Biochem.,* **2004**, *334*, 257-265.

127. R. M. Sanchez-Martin, M. Muzerelle, N. Chitkul, S. E. How, S. Mittoo, M. Bradley, *Chem. Bio. Chem.* **2005**, *6*, 1341-1345.

128. M. J. Levene, J. Korlach, S. W. Turner, M. Foguet, H. G. Craighead, W. W. Webb, *Science*, **2003**, *299*, 682-686.

129. A. Tribu, G. Sallen, T. Aichelle, R. André, J.-P. Poizat, C. Bougerol, S. Tatarenko, K. Kheng, *Nano. Lett.*, **2008**, *8*, 4326-4329.

130. Y. Dong, S-S. Feng, *Biomaterials*, **2005**, *26*, 6068-6076.

131. L. Brannon-Peppas, J. O. Blanchette, *Adv. Drug Deliv. Rev.*, **2004**, *56*, 1649-1659.

132. Y. Gogotsi, Nanomaterials Handbook, CRC Press Taylor and Francis group, Boca Raton Florida - USA, **2006**, pg 654

133. M. Bruchez Jr., M. Moronne, P. Gin, S. Weiss, A. P. Alivisatos, *Science*, **1998**, *281*, 2013-2016.

134. W. C. W. Chan, S. Nie, *Science*, **1998**, *281*, 2016-2018.

135. T. Vo-Dihn, 'Nanotechnology in Biology and Medicine: Methods, Devices and Applications' CRC Press Taylor and Francis group, Boca Raton Florida - USA, **2007**.

136. X. Gao, Y. Cui, R. M. Levenson, L. W. K. Chung, S. Nie, *Nat. Biotechnol.*, **2004**, *22*, 969-976.

137. J. K. Jaiswal, H. Mattoussi, J. M. Mauro, S. M. Simon, *Nat. Biotechnol.*, **2003**, *21*, 47-51.

138. D. Ishii, K. Kinbara, Y. Ishida, N. Ishii, M. Okochi, M. Yohda, T. Aida, *Nature*, **2003**, *423*, 628-632.

139. T. Hiromichi, N. Hiroyuki, H. Susumu, H. Sachiko, O. Ko, S. Toshikazu, *J. Histochem. Cytochem.*, **2000**, *43*, 653-662**.**

140**.** A. Zaheer, A. Lenkinski, A. Mahmood, A. G. Jones, L. C. Cantley, J. V. Frangioni, *Nat. Biotechnol.*, **2001**, *19*, 1148-1155.

141. M. Gui, S. Nagaraj, S. V. Rahavendran, H. T. Karnes, *Analytica Chimica Acta*, **1997**, *342*, 145-149.

142. A. L. Rogach, A. Eychmuller, S. G. Hickey, S. V. Kershaw, *Small*, **2007**, *3*, 536-557.

143. W. Bae, N. Ki, K. Min Ki, K. Char, S. Lee, *Chem. Mater.*, **2008**, *20*, 5307-5313.

144. L. Li, P. Reiss, *J. Am. Chem. Soc.*, **2008**, *130*, 11588-11589.

145. Z. A. Peng, X. Peng, *J. Am. Chem. Soc.*, **2001**, *123*, 183-184.

146. Z. A. Peng, X. G. Peng, *J. Am. Chem. Soc.*, **2002**, *124*, 3343–3353.

147. L. H. Qu, X. G. Peng, *J. Am. Chem. Soc.*, **2002**, *124*, 2049–2055.

148. Y. Zhang, Y. Li, X.-P. Yan, *Small*, **2009**, *5*, 185-189.

149. S. H. Wei, A. Zunger, *Appl. Phys. Lett.*, **1998**, *72*, 2011-2013.

150. S. Kim, B. Fisher, H.-J. Eisler, M. Bawendi, *J. Am. Chem. Soc.*, **2003**, *125*, 11466-11467.

151. R. Weissleder, *Nat. Biotechnol.*, **2001**, *19*, 316-317.

152. H. Seo, S. W. Kim, *Chem. Mater.*, **2007**, *19*, 2715-2717.

153. R. E. Bailey, S. M. Nie, *J. Am. Chem. Soc.*, **2003**, *125*, 7100-7106.

154. J. P. Zimmer, S. W. Kim, S. Ohnishi, E. Tanaka, J. V. Fragioni, M. G. Bawendi, *J. Am. Chem. Soc.*, **2006**, *128*, 2526-2527.

155. J. M. Tsay, M. Pflughoefft, L. A. Bentolila, S. Weiss, *J. Am. Chem. Soc.*, **2004**, *126*, 1926-1927.

156. R. Xie, X. Zhong, T. Basché, *Adv. Mater.*, **2005**, *17,* 2741-2745.

157. M. A. Malik, P. O'Brien, N. Revaprasadu, *Chem. Mater.*, **2002**, *14*, 2004-2010.

158. L. I. Berger, 'Semiconductor Materials' CRC Press, **1996**.

159. A. L. Rogach, D. V. Talapin, H. Weller, *Colloids and Colloid Assembly*, F. Caruso Ed., Wiley-VCH: Weinheim, Germany, **2004**.

160. J. J. Li, J. M. Tsay, X. Michalet , S. Weiss, *Chem. Phys.*, **2005**, *318*, 82–90.